Doctoral Dissertation

Image Reconstruction with Limited-view-angle Projection Data for BNCT-SPECT

Lu Fan

January 2025

Graduate School of Engineering,
Osaka University

Abstract

Boron Neutron Capture Therapy (BNCT) is an advanced, targeted radiation therapy that offers a highly selective approach to cancer treatment by leveraging the unique properties of boron-10 and neutron beams. BNCT has significant advantages over conventional radiotherapy: it selectively targets cancer cells while minimizing damage to surrounding healthy tissue, making it particularly valuable for treating invasive and recurrent tumors that are difficult to treat with surgery or traditional radiation. In BNCT, boron-10, which accumulates preferentially in tumor cells, is irradiated with neutrons, triggering a reaction that releases alpha particles and lithium nuclei. These particles have a very short range, destroying cancer cells with minimal effect on adjacent tissues.

Despite its potential, several technical challenges remain for BNCT to reach its full clinical effectiveness. A major unresolved issue is the development of a real-time monitoring system to assess treatment effects as they occur. There is particular interest in a method to detect gamma rays promptly emitted from the neutron-^{10}B reaction, enabling image reconstruction similar to Single Photon Emission Computed Tomography (SPECT), known as BNCT-SPECT.

Developing BNCT-SPECT is challenging due to two main factors. First, there is a limitation in projection angles: unlike conventional SPECT systems, which rely on projections across 360 degrees, BNCT-SPECT is restricted to under 90 degrees. This limitation renders Fourier-based reconstruction methods impractical. Second, measurement time is constrained, as BNCT-SPECT must operate simultaneously with treatment, raising concerns about acquiring sufficient counts for accurate imaging.

To overcome these challenges, this study explores a novel approach using Bayesian estimation in a successive approximation framework, which is specifically designed to operate effectively under BNCT-SPECTs limited-view-angle conditions. The proposed method not only addresses angle and time constraints but also enhances the potential for real-time, accurate monitoring of BNCT treatment effects. Detailed methodology and results are presented in this paper.

The structure of this paper is as follows. **Chapter 1** provides an introduction to BNCT and the principles of BNCT-SPECT. **Chapter 2** discusses Bayesian estimation, explaining its fundamental concepts and the rationale for selecting this method in our study. **Chapter 3** details the construction of the experimental system, including the setup process and descriptions of the equipment used. **Chapter 4** introduces the MCNP5 simulation code, explaining its principles and its role in this research. **Chapter 5** focuses on the design of the mock-up system, describing the design of each component and the sequence of experiments. **Chapter 6** presents image reconstruction, using the theoretical foundations and experimental results obtained from previous chapters. Finally, **Chapter 7** provides a summary of the study's findings.

CATALOG

Chapter 1 Introduction

1.1 Research background

In Japan, the number of deaths by cause of malignant neoplasms (tumors) in 2022 was 385,787 accounting for 24.6% of all deaths in the first place as shown in Figure 1.1. Looking at the annual trends in death rates in Figure 1.2, malignant neoplasms (tumors) have consistently risen and have been the leading cause of death since 1947 [1].

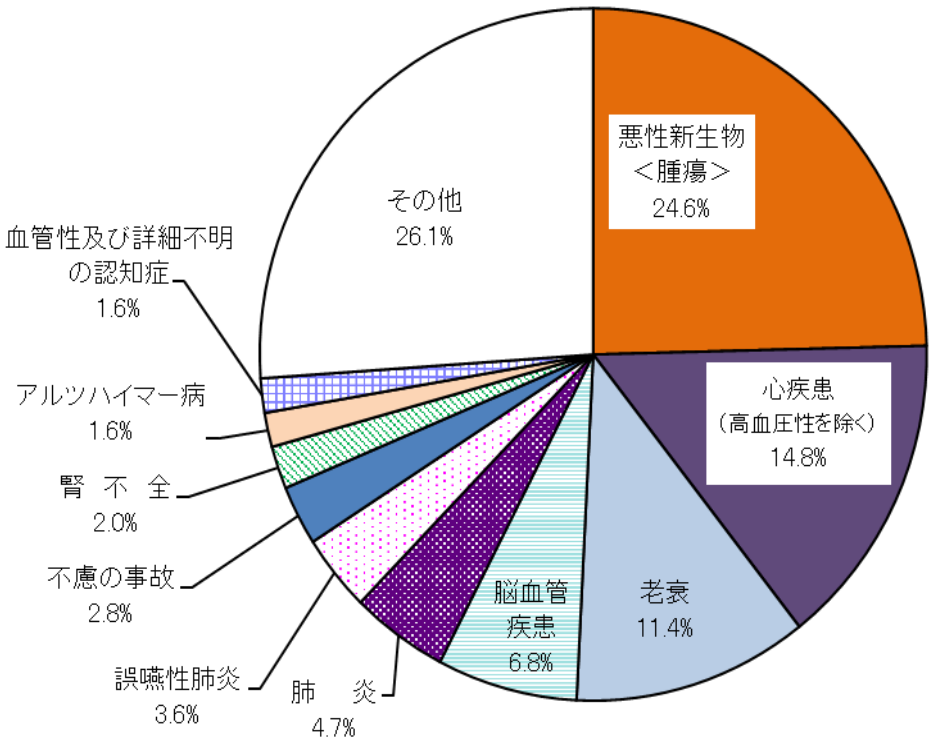

Figure 1.1 Composition of major causes of death (2022).

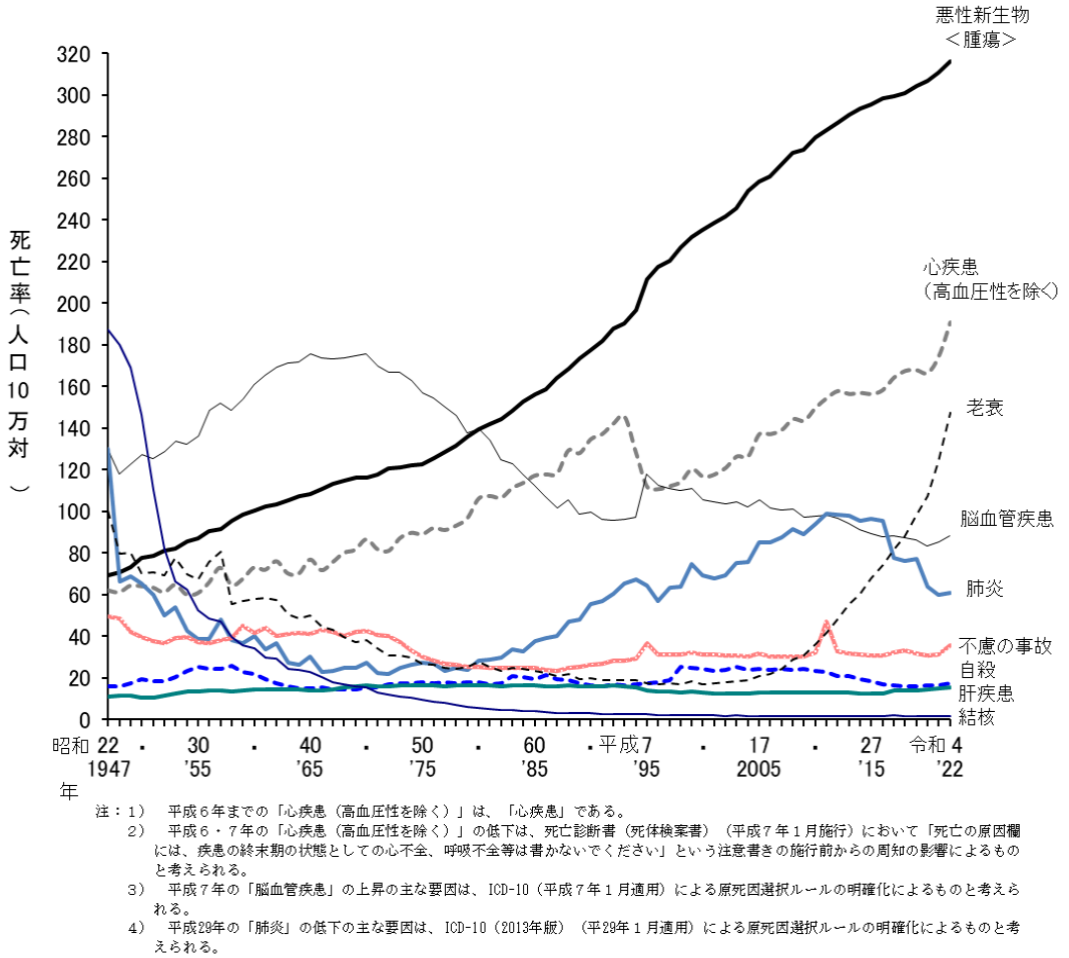

Figure 1.2 Annual mortality rates by leading causes of death (per 100,000 population).

The trend of increasing mortality and morbidity of cancer is expected to be kept. Therefore, research on effective cancer treatment methods is essential for Japan. The three primary treatment methods for cancer are "surgery," "chemotherapy," and "radiation therapy"[2].

Surgical treatment of cancer involves the direct excision of the tumor through operative intervention. To reduce the risk of recurrence, it is standard practice to remove surrounding tissues and regional lymph nodes simultaneously. While this approach can be highly effective, the removal of nearby tissue and lymph nodes may compromise the function of specific organs, potentially affecting the patient's quality of life and ability to perform daily activities post-surgery. Additionally, surgical procedures are generally performed under general anesthesia, which necessitates a certain level of physical

health. As a result, surgical intervention may not be appropriate for elderly patients or those with significant comorbidities.

Chemotherapy, another cornerstone of cancer treatment, primarily utilizes anti-cancer drugs which include recently developed molecularly targeted agents, to inhibit the proliferation of cancer cells, leading to tumor shrinkage and cellular destruction. Administered orally or by injection, these drugs circulate through the bloodstream, enabling them to target not only primary tumors but also microscopic lesions and metastatic cells. However, because chemotherapy affects both malignant and normal dividing cells, patients often experience significant side effects that can detrimentally impact their daily lives. These side effects can include nausea, immunosuppression, and fatigue, reflecting the non-selective nature of many anti-cancer drugs.

Radiation therapy, a fundamental modality in cancer treatment, employs high-energy radiation to target and shrink tumors. By delivering ionizing radiation directly to cancerous tissues, radiation therapy induces intracellular damage, disrupts cellular DNA repair mechanisms, impedes cell division, and ultimately leads to cancer cell death, resulting in tumor reduction. Despite its effectiveness, conventional radiation therapy is not tumor-specific, posing a risk of collateral damage to surrounding healthy tissues. To address these limitations, advances in physical and biological sciences have led to the development of more targeted radiation therapies, including Boron Neutron Capture Therapy (BNCT).

BNCT represents a novel approach to radiation therapy, leveraging the unique properties of boron-10 to achieve high selectivity in targeting cancer cells. Through neutron irradiation, boron-10 undergoes a nuclear reaction that releases highly localized energy within the cancer cells, sparing nearby healthy tissue and offering new potential for the treatment of invasive and recurrent tumors that are challenging to manage with conventional methods.

1.2 The principal of BNCT

BNCT is a new cancer therapy using boron-10 and neutron. The boron-neutron capture

reaction induced by low-energy neutrons generates alpha-ray and lithium nuclei that can kill cancer cells effectively.

$$\begin{aligned} {}^{10}\mathrm{B} + \mathrm{n} \quad &\rightarrow {}^{7}\mathrm{Li} + \alpha + 2.79\ \mathrm{MeV}\ (6\%) \\ &\rightarrow {}^{7}\mathrm{Li}^{*} + \alpha + 2.31\ \mathrm{MeV}\ (94\%) \\ &\rightarrow {}^{7}\mathrm{Li}^{*} \rightarrow {}^{7}\mathrm{Li} + \gamma(478\ \mathrm{keV}) \end{aligned} \tag{1.1}$$

Figure 1.3 shows the principle of BNCT. A drug-containing ^{10}B is administered to the patient to accumulate in the cancer cells. Then, the patient is irradiated with thermal neutrons (around 0.025eV) or epi thermal neutrons (0.5eV to 10keV) from outside the body. The nuclear reaction is shown in Equation (1.1); alpha-ray and lithium particles (^{7}Li) are the primary neutron-induced charged particles. The distance between them is short, about 10 μm for α-particles and about 5 μm for ^{7}Li, and this length is close to the size of a cancer cell (about 10 μm), only the cancer cells in which ^{10}B is accumulated will be killed by DNA damage caused by alpha-ray and ^{7}Li. This is genuinely a radiation therapy method that can attack cancer cells with high pinpoint accuracy.

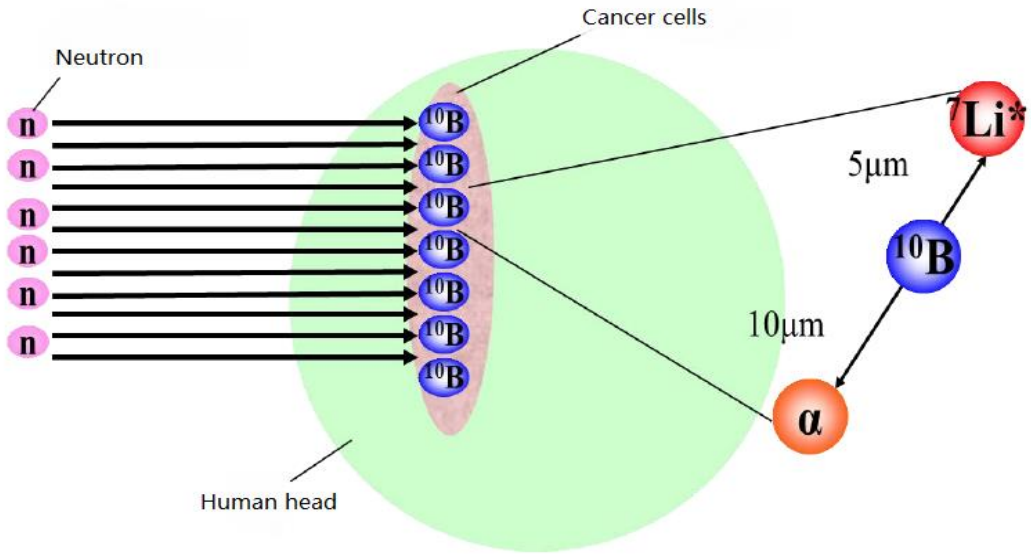

Figure 1.3 The principle of BNCT.

This indicates that BNCT exerts a substantially lesser impact on normal cells compared to conventional radiation therapies that use electromagnetic waves. Moreover,

unlike other treatments where repeated exposure to radiation limits the possibility of treating the same area multiple times, BNCT permits repeated treatments on the same region, offering a substantial therapeutic advantage.

As shown in Table 1.1, ^{10}B and low energy neutrons were chosen for three reasons: firstly, the reaction cross-section of ^{10}B with thermal neutrons is substantial compared to the elements present in the human body. Secondly, the secondary radiation produced after the nuclear reaction must be short because if the secondary radiation is long, the particles may reach normal cells and affect them. Thirdly, boron compounds are readily taken up by living organisms and do not have the high toxicity of heavy metals.

Table 1.1 Reaction cross sections of major nuclei and thermal neutrons [3].

Major nuclei in the human body		
Targeted nuclei	Nuclear reaction	Reaction cross-section /barn
^{1}H	$^{1}H(n,\gamma)^{2}H$	0.3320
^{12}C	$^{12}C(n,\gamma)^{13}C$	0.0035
^{14}N	$^{14}N(n,\gamma)^{15}N$	0.07500
^{16}O	$^{16}O(n,\gamma)^{17}N$	0.0001899
Major nuclei with large reaction cross-section		
Targeted nuclei	Nuclear reaction	Reaction cross-section /barn
^{3}He	$^{3}He(n,p)^{3}H$	5.332×10^{3}
^{6}Li	$^{6}Li(n,\alpha)^{3}H$	0.9412×10^{3}
^{10}B	$^{10}B(n,\alpha)^{7}Li$	3.840×10^{3}
^{157}Gd	$^{157}Gd(n,\gamma)^{158}Gd$	254.1×10^{3}

Low-energy neutrons are utilized for two primary reasons. Firstly, the reaction cross-section of ^{10}B is more significant at low energies than at high energies, as shown in Figure 1.4. Secondly, higher energy neutrons have a more significant effect on normal cells and are more likely to cause complications. In other words, low-energy neutrons

are more likely to cause nuclear reactions and have a more negligible effect on normal cells than high-energy neutrons.

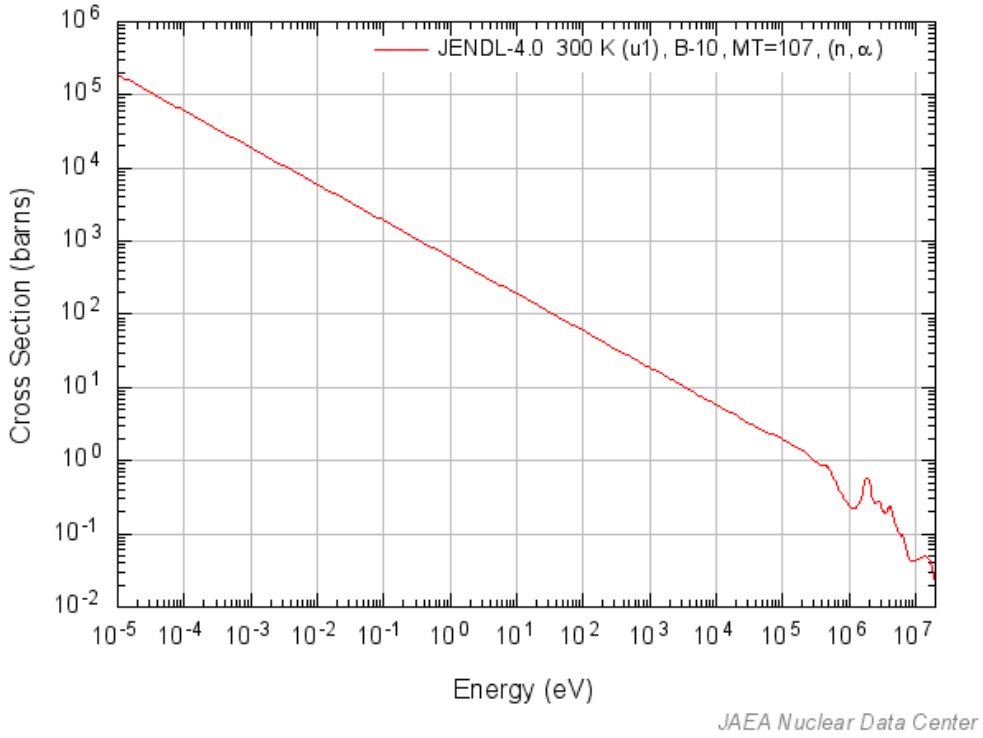

Figure 1.4 Reaction cross-section of ^{10}B (n,α)^{7}Li [4]

1.3 History of BNCT

Research on BNCT has been ongoing for over 70 years, and recent advancements have brought it to the cusp of widespread clinical implementation, with preparations nearly complete for its full-scale use in therapeutic settings.

The principle of BNCT was proposed in 1936 by American physicist Locher [5], merely four years after Chadwick's discovery of the neutron in 1932. By the 1940s, foundational research involving neutrons produced by accelerators was being conducted in the United States, using cell cultures and small animal models to explore the therapy's potential.[6][7] During this period, it was hypothesized that if ^{10}B could be selectively absorbed by cancer cells, it would enable the targeted destruction of these cells. From the 1950s to the 1960s, therapeutic irradiation for BNCT was conducted at the Brookhaven National Laboratory's research reactor (BGRR) and the Massachusetts

Institute of Technology's research reactor (MITR). A number of brain tumor cases were treated using a thermal neutron field and borax (which contains 96% ^{10}B). However, the anticipated therapeutic outcomes were not achieved, leading to the suspension of BNCT research in 1961.

From 1964 to 1968, Dr. Hatanaka—a neurosurgeon from Teikyo University who had studied BNCT at Harvard University—conducted collaborative research with chemist Soloway and colleagues. Together, they introduced the boron compound BSH (Borocaptate Sodium: $Na_2B_{12}H_{11}SH$), which demonstrated superior accumulation of ^{10}B in brain tumors, enhancing its potential for BNCT applications. [8] After returning to Japan in 1968, Dr. Hatanaka conducted the first BNCT treatment in the country, utilizing the thermal neutron field from Hitachi's research reactor. [9] To ensure that the thermal neutrons reached the deep regions of the brain tumor, Dr. Hatanaka combined the treatment with craniotomy. As a result, the therapeutic outcomes were significantly better than those achieved in the United States. Following this success, similar clinical studies were conducted at various research reactors, including the MITRR at Musashi Institute of Technology, the KUR at Kyoto University, and the JRR-2 and JRR-4 reactors at the Japan Atomic Energy Agency.

In 1987, a research group led by Mishima at Kobe University conducted clinical studies using BPA (p-Boronophenylalanine: $C_9H_{12}BNO_4$), a boron compound that can be efficiently accumulated in cancerous tissues via the amino acid transporter. This research led to the world's first successful application of BNCT for the treatment of malignant melanoma. [10] The introduction of BPA marked a pivotal moment for BNCT, as it became the first treatment method capable of selectively targeting and eradicating cancer cells.

Subsequently, research groups from Osaka University and Kawasaki Medical University began clinical trials for the treatment of head and neck cancers. In 2001, a team led by Kato at Osaka University successfully treated head and neck cancer for the first time in the world by combining both BSH and BPA in BNCT. Furthermore, research into the treatment of other types of cancer, including liver cancer and mesothelioma, has also begun in recent years.

Looking internationally, the United States, recognizing Japan's excellent BNCT treatment outcomes, resumed BNCT research in 1994. The BMRR reactor at Brookhaven National Laboratory (BNL) was modified to generate a thermal neutron field for BNCT and combined with BPA to treat brain tumors.

In 1997, an EU-based research group, led by Germany, began clinical studies using a thermal neutron field at the Petten Nuclear Research Center (HFR) in the Netherlands. The use of this thermal neutron field enabled the maintenance of a high dose deep within tissues, making it possible to treat brain tumors non-invasively, without the need for craniotomy. In Japan, modifications were made to the KUR and JRR-4 reactors, allowing for non-invasive treatment using thermal neutrons. While BNCT has advanced in this way, the therapy requires powerful thermal and fast neutron sources. As a result, clinical BNCT treatments are currently only conducted using reactors. Until 2010, the construction of small-scale reactors for BNCT was being considered. The development of small-scale accelerator-based fast neutron sources, which can be installed within hospitals, is actively underway as a new neutron source for BNCT.

Since 2000, advancements in accelerator technology have made it possible to develop BNCT accelerators that can be installed within hospitals. This progress has spurred active BNCT research in various countries [12-14], including the United Kingdom, Italy, and Argentina. Particularly in Japan, numerous universities, research institutes, and companies have initiated projects aimed at establishing BNCT treatment systems using accelerators. The first such project in Japan was launched by Kyoto University and Sumitomo Heavy Industries, which developed a treatment system utilizing a cyclotron accelerator. This system is now in the final stages of clinical trials. The successful development of such accelerators would not only contribute to the widespread adoption of BNCT but also enable treatment research at the university and hospital levels, potentially leading to improved therapeutic outcomes.

1.4 Challenges of BNCT

BNCT is an exceptionally effective treatment, and research aimed at its widespread adoption is being conducted globally. However, to establish BNCT as a standard

radiation therapy, several challenges remain. From a physical perspective, there are primarily three key issues to address.

Firstly, a high-intensity low-energy neutron beam generated by a BNCT accelerator is required. Currently, treatment can only be performed using reactors, which limits the accessibility and scalability of the therapy.

Secondly, the characterization of the neutron field remains challenging. In reactors, the neutron field is almost standardized, and thus, there are few issues related to its characterization. However, with accelerator-based neutron sources, the current neutron intensity and other characteristics are somewhat insufficient, and it is difficult to ensure an adequate thickness of the attenuation materials. As a result, the irradiation field cannot be considered fully standardized. Therefore, when using an accelerator-generated neutron field for treatment, it is crucial to accurately understand the energy spectrum, intensity, and any potential presence of unnecessary high-energy neutrons or gamma-rays. This issue is currently under investigation at the research stage. [15-17]

Thirdly, real-time measurement of treatment effectiveness is difficult. The evaluation of BNCT treatment efficacy is determined by multiplying the boron concentration distribution in the tumor and surrounding normal tissues with the intensity distribution of the neutron flux that reaches these areas.

In this study, to accurately measure the treatment efficacy in real-time, this study aims to develop a device called BNCT-SPECT, which combines the principles of Single Photon Emission Computed Tomography (SPECT), an imaging diagnostic technique, with BNCT. This device will enable the real-time three-dimensional measurement of treatment effectiveness.

1.5 BNCT-SPECT

1.5.1 The principal of SPECT

Single-photon emission computed tomography (SPECT) is a sophisticated nuclear medicine imaging technique that employs gamma-ray detection to produce tomographic images as shown in Figure 1.5, offering three-dimensional (3D)

visualization of the internal structures of the body. Unlike conventional imaging methods, which provide two-dimensional (2D) images, SPECT allows for the acquisition of 3D information, which can be presented as cross-sectional slices. These slices can be freely reformatted or manipulated to provide a comprehensive view of the patient's anatomy, facilitating enhanced diagnostic and therapeutic planning.

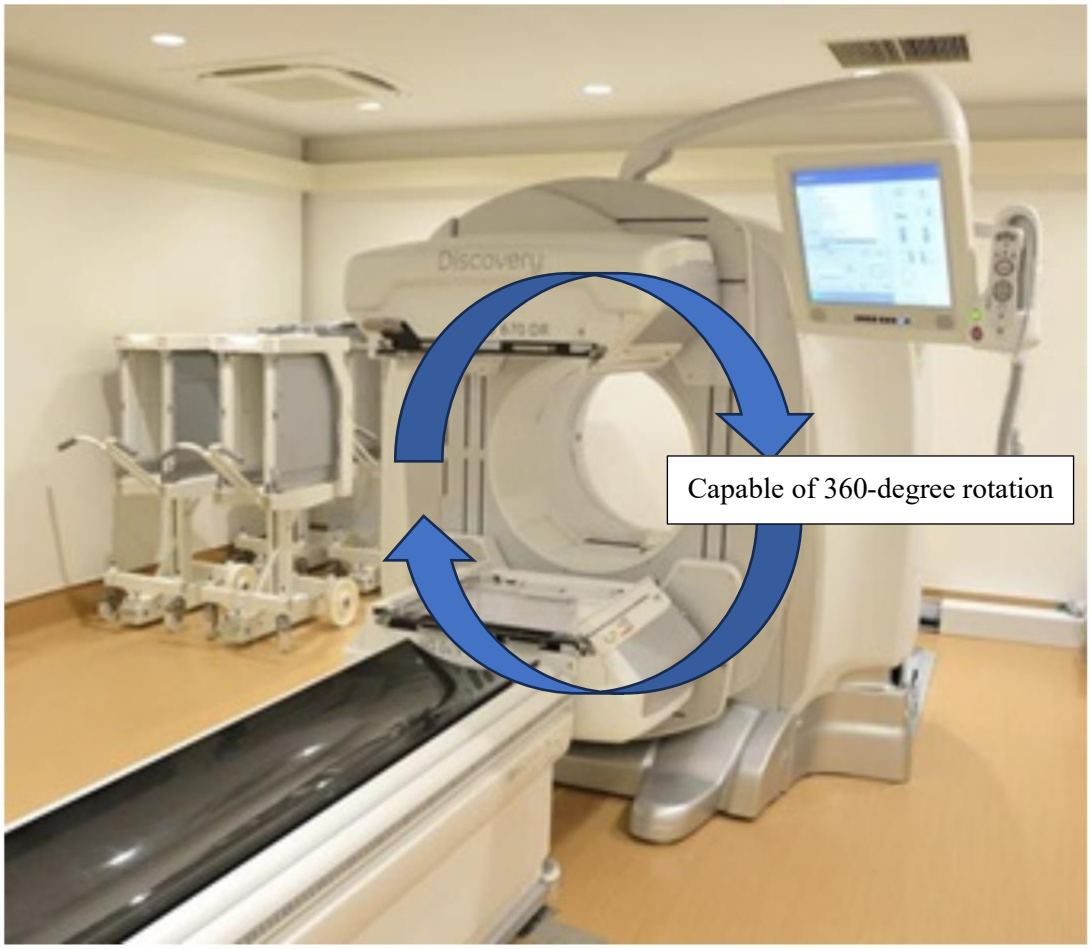

Figure 1.5 SPECT/CT of GE Healthcare Japan's Discovery 670DR. [18]

The SPECT process begins with the administration of a radiopharmaceutical that emits gamma radiation. A gamma-ray detector, typically a scintillation camera or solid-state detector, involves the rotation of a gamma-ray detector around the patient in a full 360-degree arc, capturing multiple 2D projections from various angles. This 360-degree rotation ensures that data from all perspectives are collected, allowing for a more complete and accurate reconstruction of the internal structures. These projections are then sent to a computer, which uses a tomographic reconstruction algorithm—such as

filtered back projection or iterative reconstruction—to combine the 2D projections into a 3D dataset.

The resulting 3D dataset can be further processed and visualized in various formats, such as axial, coronal, or sagittal slices, to allow detailed assessment of specific areas of interest within the body. This versatility in reformatting provides an in-depth understanding of anatomical and functional changes. SPECT imaging is commonly used in clinical settings to assess tissue function, such as blood flow in the heart, brain activity, and the distribution of certain types of cancer or infection, often complementing other imaging techniques like CT (computed tomography) or PET (positron emission tomography) for a more complete diagnosis

1.5.2 The principal of BNCT-SPECT

Figure 1.6 shows the principle of BNCT-SPECT. According to the nuclear reaction of equation (1.1), about 94 % of the ^{7}Li produced by the ^{10}B (n, α) ^{7}Li nuclear reaction is in the excited state (^{7}Li*). ^{7}Li* transitions to the ground state with a half-life of about 10^{-14} s and emits 478 keV prompt gamma-ray. The SPECT system measures the intensity distribution of the 478 keV gamma-rays emitted. The number of 478 keV gamma-rays is proportional to ^{10}B (n, α) ^{7}Li reactions, which directly indicates the therapeutic effect. The attenuation coefficient of 478 keV gamma rays in tissue is minimal (0.1 cm^{-1}), so most of the gamma-rays are emitted outside the body.

A collimator, typically made of tungsten or lead due to its high gamma-ray shielding capabilities, is positioned in front of the detector to define and control the direction of incoming 478 keV gamma-rays. Multiple gamma-ray detectors are arranged behind the collimator to measure only those 478 keV gamma-rays that pass through its precisely aligned apertures. The detected radiation dose data is then analyzed to map the distribution of (n, α) reactions occurring within the tumor. This information is used to reconstruct a three-dimensional image, providing a detailed view of the reaction activity across the targeted area. In this way, the BNCT-SPECT system enables real-time visualization and assessment of BNCT treatment efficacy, offering a valuable tool for monitoring therapeutic effects directly during treatment.

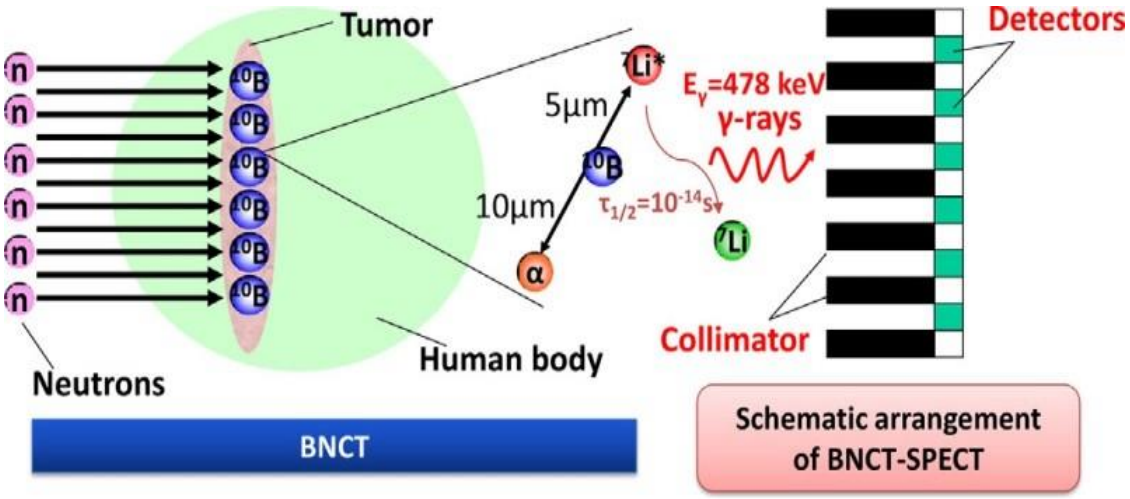

Figure 1.6 The principle of BNCT-SPECT

It is important to note, however, that in BNCT, the 478 keV gamma-ray measurements must be conducted within a high flux neutron field (high-background environment). In conventional SPECT, there is typically no background radiation from sources other than the administered single-photon-emitting radionuclide, allowing for nearly ideal measurement conditions with minimal background interference. In contrast, during BNCT, the neutron intensity near cancer cells can reach extremely high levels, approximately 1×10^9 n/sec/cm². However, the intensity of the $^{10}B(n,\alpha)^7Li$ reaction, which produces the 478 keV gamma-ray, is considerably lower—by several orders of magnitude—due to the boron concentration near cancer cells being in the range of tens of ppm. Consequently, in a high flux neutron field (high-background environment), selectively measuring the 478 keV gamma-rays from the $^{10}B(n,\alpha)^7Li$ reaction is extremely challenging. The primary interfering gamma rays, as shown in Figure 1-7, can be observed in the pulse height spectrum (PHS) obtained using a high-purity germanium semiconductor detector (HP-Ge detector) under actual BNCT treatment conditions. This spectrum provides insight into the gamma-ray background, allowing the identification of specific energy peaks associated with the $^{10}B(n,\alpha)^7Li$ reaction amid other radiation sources in the treatment environment. [19]

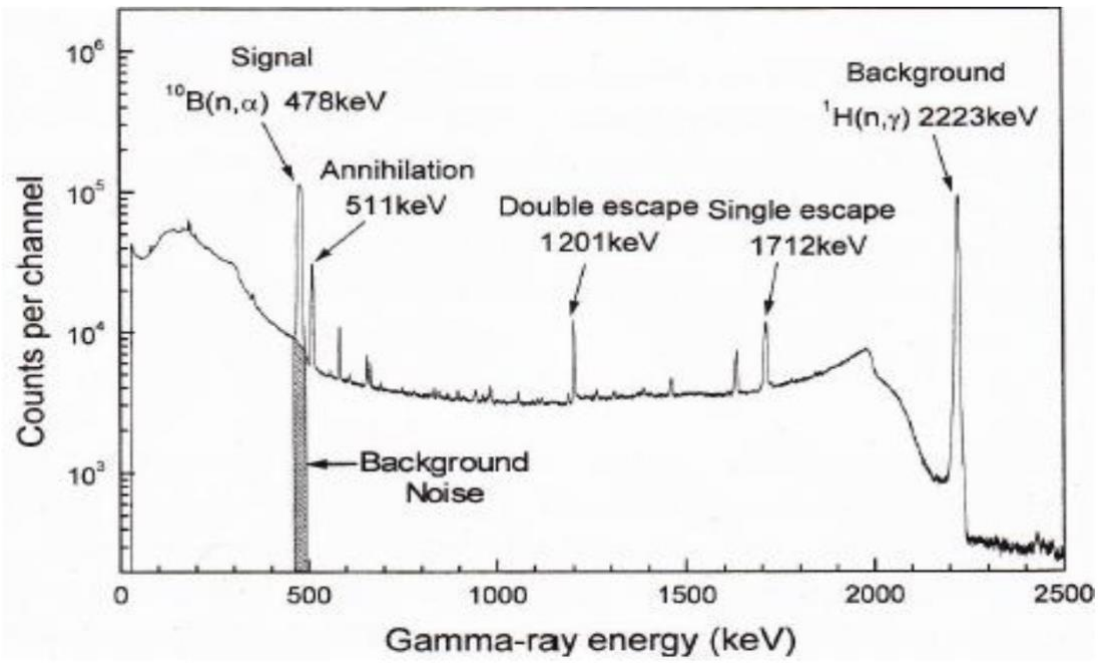

Figure 1.7 Gamma-ray pulse height spectrum (PHS) in the BNCT treatment environment obtained using a Hp-Ge detector.

From these results, it is evident that the following gamma rays present significant challenges:

1. Capture gamma-ray (2.22 MeV) produced by the $^{1}H(n,\gamma)^{2}H$ reaction near cancer cells.
2. Annihilation gamma-ray (511 keV) generated through the pair production/annihilation process.

The first issue arises from the fact that the human body contains a large amount of ^{1}H, making it unavoidable. The Compton continuum from the 2.22 MeV gamma-ray emitted by the $^{1}H(n,\gamma)^{2}H$ reaction overlaps with the photopeak at 478 keV, creating a significant background signal. To estimate the intensities of the 2.22 MeV and 478 keV gamma rays, intensity calculations were conducted. In these calculations, it was assumed that the hydrogen content in cancer cells was 11% by weight, based on actual treatment data, with a ^{10}B concentration of 10 ppm, and irradiation with thermal neutrons (0.025 eV) at an intensity of 1×10^{9} n/sec/cm^{2}. The calculations revealed that the production rate of 478 keV gamma-rays from the $^{10}B(n,\alpha)^{7}Li$ reaction is

approximately 2.2×10^6 γ/sec per cell. In contrast, the production rate of 2.22 MeV gamma-rays from the $^1H(n,\gamma)^2H$ reaction reaches 2.2×10^7 γ/sec per cell, resulting in an intensity ratio of roughly 10:1. This indicates that when the 2.22 MeV gamma-rays reach the detector, they contribute significantly to the background signal. Consequently, for accurate measurements, a gamma-ray detector with high detection efficiency specifically for 478 keV gamma-rays should be employed to mitigate this background effect as much as possible.

Additionally, regarding the second issue, the presence of annihilation gamma-rays at 511 keV close to the 478 keV gamma-rays introduces a risk of overlapping signals if the detector's energy resolution is insufficient. This overlap could prevent accurate separation of the 478 keV and 511 keV peaks, resulting in additive measurements of both gamma-rays. Therefore, to ensure accurate differentiation, a detector with an energy resolution capable of achieving a full width at half maximum (FWHM) of less than 33 keV (511 keV- 478 keV= 33 keV) is required. In other words, a gamma-ray detector with high energy resolution is essential for precise measurement in this paper.

1.6 Design of BNCT-SPECT in real treatment

In order to realize BNCT-SPECT, it is essential to accurately measure the 478 keV gamma rays generated during neutron irradiation while effectively separating them from other gamma rays. Considering the practical application in treatment, the following conditions must be met:

1. Neutron Irradiation Duration: The neutron irradiation time in BNCT is approximately 60 minutes. Therefore, the measurement of 478 keV gamma rays by BNCT-SPECT must be completed within this 60-minute time frame.
2. Measurement Accuracy: To ensure measurement precision within an acceptable range, the peak net count of 478 keV gamma-rays for each detector must be at least 1,000 counts.
3. Spatial Resolution of SPECT Images: From a treatment perspective, the spatial resolution of the obtained SPECT images must be within a few millimeters.
4. Energy Resolution: To effectively separate the 511 keV gamma-ray peak, which

is located closest to the 478 keV gamma ray, the energy resolution of the detector must be FWHM < 33 keV (= 511 keV- 478 keV).

To achieve the high spatial resolution required by the condition 3, the detector needs to be compact. Additionally, to meet the conditions 1 and 2 (i.e., obtaining more than 1,000 counts per detector within the 60-minute irradiation period), the detector must have a high detection efficiency for the 478 keV gamma-rays. Furthermore, to fulfill the condition 4 (excellent energy resolution), this study selects a GAGG (Gadolinium Aluminum Gallium Garnet) scintillator.

The GAGG detector is well-suited for this purpose because of its high light yield, fast decay time, and good energy resolution, which allow for accurate measurement of gamma rays with minimal interference from nearby peaks, such as the 511 keV gamma-rays. Its compact size enables high spatial resolution, and its efficiency at the relevant gamma-ray energies ensures that the required count rates can be achieved in the time constraints for BNCT-SPECT.

The basic characteristics and operating principles of the GAGG detector will be discussed in detail in Chapter 3.

1.7 Structure of this paper

This paper aims to investigate image reconstruction methods with limited-view-angle projection data using Bayesian estimation, with a particular focus on its application in BNCT-SPECT systems. This paper is composed of 7 chapters. The structure of the paper is organized as follows:

Chapter 2 discusses the core principles of Bayesian estimation, specifically applying Bayes' theorem and Maximum Likelihood Expectation Maximization (ML-EM) in the context of BNCT-SPECT image reconstruction. Performance evaluation indices such as Mean Absolute Error (MAE) and Structural Similarity Index Measure (SSIM) are also introduced to assess the quality of the reconstructed images.

Chapter 3 presents the experimental system, detailing the equipment used, including the GAGG scintillator, MPPC (Multi-Pixel Photon Counter), MCA (Multi Channel Analyzer), and phantom design. It also describes the experimental procedures in detail.

In Chapter 4, the MCNP5 simulation software is introduced, providing an in-depth discussion of Monte Carlo simulations, variance reduction methods, forced collision techniques, tally methods, and comparisons between simulation results and experimental data.

Chapter 5 focuses on the design of the mock-up system, elaborating on the design of the collimator, gamma-ray systems, and presenting the final design results.

Chapter 6 delves into the image reconstruction process, comparing mathematically ideal reconstruction with results obtained from experimental data. The chapter concludes with a summary of the findings from these experiments.

Finally, Chapter 7 concludes the paper, summarizing the main contributions and proposing directions for future research.

Each chapter contributes to a comprehensive understanding of BNCT-SPECT, from theoretical concepts and experimental design to practical implementation and evaluation.

References

[1] 厚生労働省政策統括官付参事官付人口動態・保健社会統計室, “令和4年(2022)人口動態統計月報年計（概数）の概況”,2024
https://www.mhlw.go.jp/toukei/saikin/hw/jinkou/geppo/nengai22/index.html

[2] U.S. Department of Health and Human Services, National Institutes of Health, National Cancer Institute, 2020

[3]公益財団法人医用原子力技術研究振興財団　日本中性子捕捉療法学会, “BNCT基礎から応用まで−BNCTを用いて治療にかかわる人のためのテキスト−”

[4] K. Shibata, O. Iwamoto, T. Nakagawa, N. Iwamoto, A. Ichihara, S. Kunieda, S. Chiba, K. Furutaka, N. Otuka, T. Ohsawa, T. Murata, H. Matsunobu, A. Zukeran, S. Kamada, and J. Katakura: "JENDL4.0: A New Library for Nuclear Science and Engineering," *J. Nucl. Sci. Technol.* **48**(1), 1-30 (2011).

[5] G.L. Locher, “Biological effects and therapeutic possibilities of neutrons”, Am..J.Roentgenol.,36, 1-13(1936).

[6] W.H.Sweet,” The Uses of Nuclear Disintegration in the Diagnosis and Treatmentof Brain Tumor”,N.Engl.J.Med.,245,875-878(1951).

[7] L.E.Farr, W.H. Sweet, J.S. Robertson, C.G.Foster , H.B. Locksley , D.L.Sutherland, M.L. Mendelsohn, E.E. Stickley, “NEUTRON CAPTURE THERAPY WITH BORON IN THE TREATMENT OF GLIOBLASTOMA MULTIFOMRE”,Am.J.Roentgenol.,71,279-293(1954).

[8] A. H. Soloway, H. Hatanaka, M. A. Davis,” Penetration of Brain and Brain Tumo

r.VII. Tumor-Binding Sulfhydryl Boron Compounds", J.Med.Chem., 10 (4), 714–717 (1967).

[9] H. Hatanaka, Y. Nakagawa," Clinical results of long-surviving brain tumor patients who underwent boron neutron capture therapy" Clinical results of long-surviving br ain tumor patients who underwent boron neutron capture therapy",J.Neurol.,209,81-9 4(1975).

[10] Y. Mishima, C. Honda, M. Ichihashi, H. Obara, J. Hiratsuka, H. Fukuda, H.Karas hima, T. Kobayashi, K.Kanda, K.Yoshino, "Treatment of malignant melanomaby sin gle thermal neutron capture therapy with melanoma-seeking 10B-compound",Lamcet, 12(2),388-389(1989).

[11] I. Kato, K. Ono, Y. Sakurai, M. Ohmae, A. Maruhashi, Y. Imahori, M. Kirihata, M. Nakazawa,Y.Yura,"Effectiveness of BNCT for recurrent head and neck malignancies",Appl.Radiat.Isot.,61(5),1069-1073(2004).

[12] C.N. Culbertson, S .Green, A.J. Mason, D. Picton, G. Baugh, R.P. Hugtenburg,Z . Yin, M.C.Scott, J.M. Nelson,"In-phantom characterisation studies at the Birmingham Accelerator-Generated epIthermal Neutron Source (BAGINS) BNCT facility"Appl R adiat Isot.,61(5),733-738(2004).

[13] S. Agosteo, P. Colautti, M.G. Corrado, F. d'Errico, M. Matzke, S. Monti, M.Silari and R. Tinti ,"Characterisation of an Accelerator-Based Neutron Source for BNCT of Explanted Livers", Radiat. Prot. Dosimetry,70 (1-4), 559-566(1997).

[14] A.J. Kreiner, V. Thatar Vento, P. Levinas, J. Bergueiro, H. Di Paolo, A.A. Burlo n, J.M. Kesque, A.A. Valda, M.E. Debray, H.R. Somacal, D.M. Minsky, L. Estrada, A . Hazarabedian, F. Johann, J.C. Suarez Sandin, W. Castell, J. Davidson, M.Davi dson, Y.Giboudot, M.Repetto, M.Obligado, J.P. Nery, H. Huck, M. Igarzabal, A.Fern andez Salares,"Development of a tandem-electrostatic-quadrupole accelerator facility for BNCT", Appl Radiat Isot., 67, S266–S269 (2009).

[15] I.Murata, T.Obata, "Boron Neutron Capture Therapy (BNCT) - Low-Energy Neutr onSpectrometer for Neutron Field Characterization", Plasma and Fusion Ref.,9,44011 07(2014).

[16] S.Tamaki, F.Sato, I.Murata, "A feasibility design study on a neutron spectrometer for BNCT with liquid moderator", Appl.Radiat.Isot,106,41-44(2015).

[17] X.Guan, M.Manabe, I.Murata and T.Wang,"Design of an epithermal neutron flux i ntensity monitor with GaN wafer for boron neutron capture therapy", Journal of Nu clear Science and Technology,52(4),503–508(2015).

[18] 国立研究開発法人 国立国際医療研究センター病院シンチレーションカメラ（SP ECT装置）https://www.hosp.ncgm.go.jp/s037/010/080/010/index.html

[19] M.Ishikawa, T. Kobayashi, Y. Sakurai, "Optimization technique for a prompt gam ma-ray SPECT collimator system" J.RADIAT.Res.,42, 387-400(2001).

Chapter 2 Image reconstruction using Bayesian estimation

2.1 Introduction

In this study, we employ Bayesian estimation, a widely recognized method in engineering for parameter estimation, to reconstruct the gamma-ray distribution within the body. [1] Specifically, we focus on detecting gamma-rays with an energy of 478 keV, which are produced by the ^{10}B (n,α)^{7}Li reaction that occurs during the BNCT treatment process. Since the therapeutic effect of BNCT is proportional to the number of ^{10}B (n,α)^{7}Li reactions and the intensity of the 478 keV gamma-rays emitted is directly related to the number of these reactions, measuring the gamma-ray distribution provides a quantitative means of evaluating the treatment's efficacy.

In SPECT imaging, image reconstruction techniques are generally categorized into analytical methods and iterative approximation methods. Analytical methods, such as the Fourier transform and superimposed integration methods, allow for the reconstruction of images through a single computational step, assuming the projection data has a sufficiently high sampling density. However, in situations where the sampling density is insufficient, as is often the case in BNCT-SPECT due to constraints on measurement time and angular coverage, analytical methods are less effective.

In contrast, iterative approximation methods refine the image through successive recalculations of pixel values. These methods are well-suited to situations where the projection data suffers from limited sampling or angular coverage. Given the inherent limitations in BNCT-SPECT, the iterative approach is more appropriate for producing reliable and high-quality images. This chapter details the principles of Bayesian estimation and its application in estimating the gamma-ray distribution in the context of BNCT-SPECT. [2][3]

2.2 Bayesian theorem and Bayesian estimation

Bayesian theorem, a fundamental theorem on probability and conditional probability,

is described below.

In contrast to the probabilities $P(A)$ and $P(B)$ of events A and B occurring, the conditional probability $P(A|B)$ of event A occurring given event B is defined by the following Equation (2.1).

$$P(A|B) = \frac{P(A \cap B)}{P(B)} \quad (P(B) > 0) \tag{2.1}$$

When considering the partition of the event A into $A1$, $A2$, ..., Equation (2.1) can be rewritten as Equation (2.2).

$$P(A_i|B) = \frac{P(A_i \cap B)}{P(B)} \tag{2.2}$$

Equation (2.3) holds as well.

$$P(B|A_i) = \frac{P(B \cap A_i)}{P(A_i)} \tag{2.3}$$

Then considering that $A_1 \cap B, A_2 \cap B,$ ...for $P(B)$ is a partition of B, the following equation is established together with Equation (2.4).

$$\begin{aligned} P(B) &= \sum_{k=1}^{N} P(A_k \cap B) \\ &= \sum_{k=1}^{N} P(B \cap A_k) = \sum_{k=1}^{N} P(A_k) \cdot P(B|A_k) \end{aligned} \tag{2.4}$$

From the above Equation (2.2), (2.3), (2.4), the conditional probability of event A_j can be described as Equation (2.5).

$$P(A_j|B) = \frac{P(A_j) \cdot P(B|A_j)}{\sum_{j=1}^{N} P(A_j) \cdot P(B|A_j)} \tag{2.5}$$

Equation (2.5) is the formula that expresses Bayesian theorem. In Bayesian theorem, $P(A_j)$ is called the prior probability, and $P(A_j|B)$, the probability that event A_j will occur under event B, is called the posterior probability.

Bayesian revision is a procedure that applies Bayesian theorem, described in the previous section, to obtain the posterior probability from Equation (2.5) based on observed events after giving an arbitrary prior probability. Then, the posterior probability obtained by this Bayesian revision is updated as a new prior probability, and by performing repeated Bayesian revisions, an objectively reliable probability distribution can be obtained. The method of estimating probability distributions by repeatedly performing this Bayesian revision is called the Bayesian estimation method.

2.3 Application of Bayesian estimation in BNCT-SPECT

In this study, we applied Bayesian estimation to the image reconstruction technique for BNCT-SPECT.

In order to obtain the distribution of gamma-ray sources in the x and y planes, we divide the whole head into several regions as a minimum unit. We divide the 3D brain into equal n 2D slices and generally divide the slice horizontally and vertically into n sections and consider them as n^2 regions. However, n must be an odd number greater than or equal to 3. Then, with the center of the head as the origin, n detectors and collimators are placed in the orthogonal direction to the x-axis of the cell. This system consisting of the detector and collimator will be referred to as the detector system in the following. The source intensity in the j-th region (j = 1, 2, ..., n^2) is Nj [photons/sec], and the count rate [CPS] value indicated by the detector at the i-th (i = 1, 2, ..., n) measurement position is Ai. [4] As an example, the initial arrangement of the experimental system in the case of n = 5 is shown in Figure 2.1.

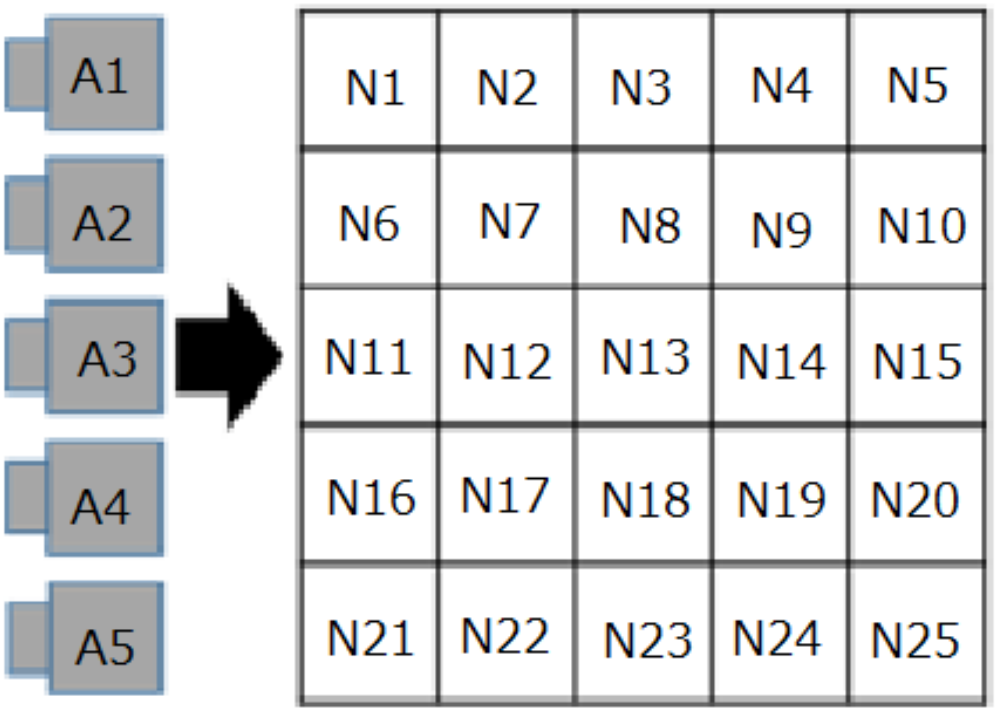

Figure 2.1 Image of the system (for n=5)

After completing the measurement at the initial position, rotate the detector system by a certain angle clockwise around the center of the origin and perform the measurement again. As shown in Figure 2.2, if we repeat this process and adjust the rotation angle so that a total of n measurements is made before the rotation angle relative to the initial state reaches 90 degrees, we end up with a total of n^2 measurements from A_1 to A_n^2.

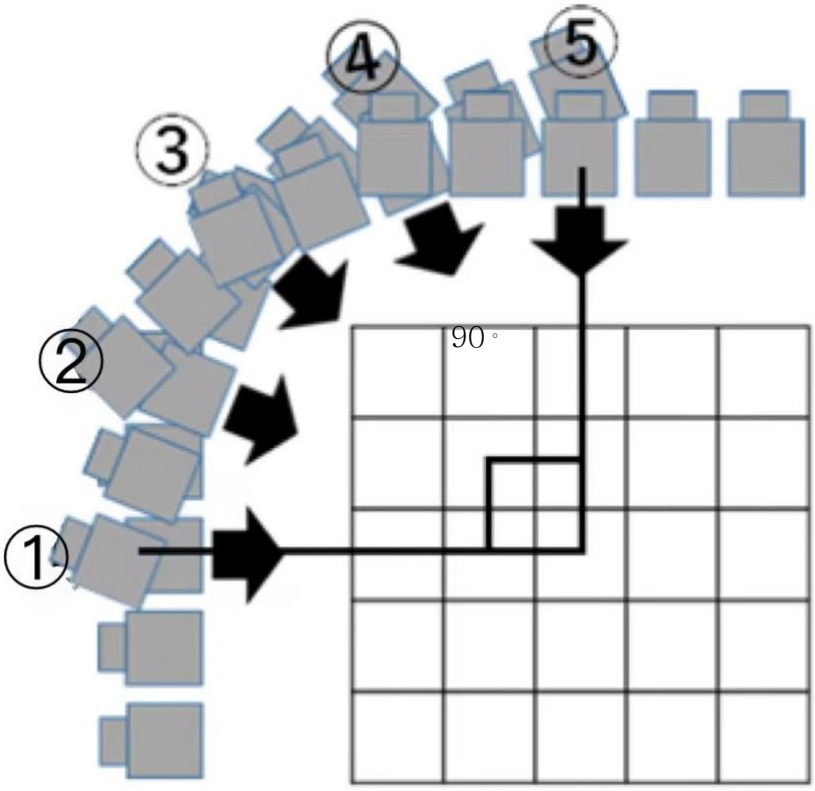

Figure 2.2 Detectors' moving angle θ=90 degrees

In this study, we classified the gamma-ray source states inside the cells in the system into the point source case and constructed simulation models for each of them.

In this detector system, radiation entering the detector is collimated to focus the measurements. Therefore, each detector has a field of view, as shown in Figure 2.3, which defines the detectable range. Let the collimator have a length of ℓ [cm], a hole radius at the center of the collimator of φ [cm], and the coordinates of the detector's center be x_sec and y_sec The range included in the detector's field of view can be expressed in the x,y -plane by the following Equation (2.6).

$$-\frac{2\varphi}{\ell}(x - x\_sec) + (y\_sec + \varphi) \leq y \leq \frac{2\varphi}{\ell}(x - x\_sec) + (y\_sec - \varphi) \quad (2.6)$$

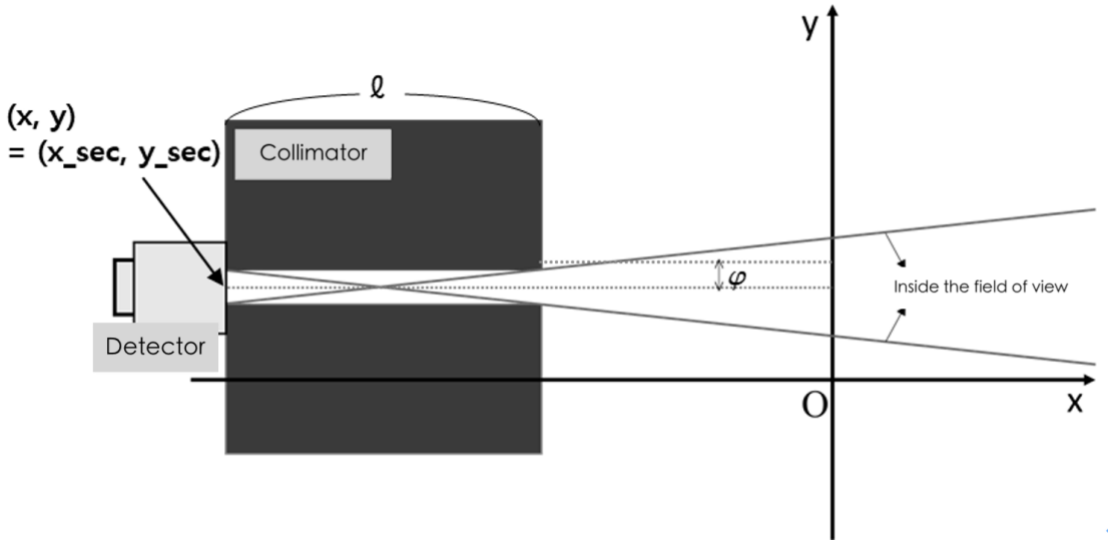

Figure 2.3 The field of view of the collimator and detector.

In the case of a point source, it is assumed that a radiation source with no area is placed in the center of the cell. Therefore, if the center of cell j is included inside the detector's field of view at position i, the radiation originating from cell j is determined to be incident on detector i.

On the other hand, in the case of a surface radiation source, it is assumed that the volume source exists uniformly spread out in the cell region. The difference between the point source and the area source is that even if the center of the cell is not included in the view of the detector, the radiation intensity corresponding to the percentage of the area included in the field of view is determined to be incident on the detector. The actual model determines whether the radiation originating from cell j is incident on the detector at position i or not, and then the fraction of radiation sources contained inside the detector's field of view is calculated.

In preparation for applying this system to Bayesian revision, we will treat the Nj and Ai defined earlier as vectors $\vec{N}$ and $\vec{A}$ in the following. The purpose of this study is to estimate the unknown vector, $\vec{N}$, from the known vector, $\vec{A}$, using Bayesian estimation. First, we define the probability that a gamma-ray emitted from the j-th region is incident on the detector placed at the i-th position as $R_{i,j}$, and define the matrix **R** in the same way. This **R** is called the response. The response

components $R_{i,j}$ can be expressed by the Equation (2.7). Here, $r_{i,j}$ represents the distance between the detector and the radiation source at measurement position i, $D_{i,j}$ is the distance the gamma rays emitted from the source in cell j travel through the head, con is the coverage ratio of the gamma rays from the source inside the detector's field of view in cell j, μ is the attenuation coefficient of the head, E_f is the detection efficiency of the detector, and φ is the radius of the collimator's hole.

$$\mathrm{R}_{i,j} = con \times \frac{\pi\varphi^2}{4\pi r_{i,j}^2} \times E_f \times e^{-\mu D_{i,j}} \tag{2.7}$$

The vectors $\vec{N}$, $\vec{A}$, and the matrix **R** can be expressed by the following Equation (2.8).

$$\vec{N} = \begin{pmatrix} N_1 \\ N_2 \\ \vdots \\ \vdots \\ N_{n^2} \end{pmatrix}, \qquad \vec{A} = \begin{pmatrix} A_1 \\ A_2 \\ \vdots \\ \vdots \\ A_{n^2} \end{pmatrix}, \qquad \boldsymbol{R} = \begin{pmatrix} R_{1,1} & \cdots & R_{1,n^2} \\ \vdots & \ddots & \vdots \\ R_{n^2,1} & \cdots & R_{n^2,n^2} \end{pmatrix} \tag{2.8}$$

We get the following equation to express these relationships in terms of matrix Equations (2.9).

$$\vec{A} = \mathbf{R} \cdot \vec{N} \tag{2.9}$$

In BNCT-SPECT, $\vec{A}$ is a known number, and $\vec{N}$ is an unknown number, so the above determinant is solved inversely. **R** is a regular matrix, and there is a possibility of obtaining a computational solution. However, since $\vec{A}$ is a measured value, it is not immune to the influence of error, and the result solved mathematically as an inverse problem is not considered the actual value. Therefore, to obtain a meaningful engineering solution, Bayesian estimation is used in this research.

First, let the sample space Ω be the 'radiation incident on the detector', representing

the whole event. Therefore, the probability $P(\Omega)$ is "the probability that radiation enters the detector. Then, let event Ej be the event 'when radiation is detected, the radiation originates from the j-th cell' and event Fi is the event 'radiation is incident on the detector at the i-th measurement position, and the detector emits a signal'. Therefore, the probability $P(Ej)$ represents 'the probability that the radiation originates from the j-th cell when it is detected', and similarly, the probability $P(Fi)$ represents 'the probability that the radiation is incident on the detector at the i-th measurement position and the detector emits a signal'.

The "parallel hypothesis" allows us to interpret the event group $\{Ej\}$ as "there are multiple parallel hypotheses that form the measurement result, and any one of them could be the correct hypothesis [2]. This gives the mixing proportions of each hypothesis, which are finally paralleled by Bayesian estimation and are given by the posterior probabilities of the hypotheses, $P(Ej\,|Fi\,)$. In this study, we calculate $P(Ej\,|Fi\,)$ as the probability that the gamma-ray incident on the detector at measurement position i originates from the j-th cell. This allows us to calculate an estimate of the distribution of gamma-ray sources in the head that is reasonable when the measurements are obtained. This probability $P(Ej\,|Fi\,)$ is shown as Equation (2.10).

$$\mathrm{P}\left(E_j|F_i\right) = \frac{P\left(E_j\right)\cdot P\left(F_i|E_j\right)}{\sum_{j=1}^{N} P\left(E_j\right)\cdot P\left(F_i|E_j\right)} \tag{2.10}$$

Referring to Equation (2.9), $P(Ej\,|Fi\,)$ corresponds to the response function $R(i,j)$, and $P(Ej)$ corresponds to the source intensity Nj. However, to perform Bayesian estimation, it is necessary to transform these equations based on the axiom of probability as follows.

First, the response function is normalized according to the equation (2.11) using the sum of the response function elements $\{R_{i,j}\}$ for i, $\sum_i R_{i,j}$.

$$R'_{i,j} = \frac{R_{i,j}}{\sum_i R_{i,j}} \tag{2.11}$$

From this definition, the sum of the elements of the normalized response function $\{R'_{i,j}\}$ for i, $\sum_i R'_{i,j}$, is 1 for all j. Also, using the sum of the response function elements $\{R_{i,j}\}$ for i $\sum_i R_{i,j} = f_j$, we define the matrix $\boldsymbol{Eff}$ represented by the following Equation (2.12).

$$\boldsymbol{Eff} = \begin{bmatrix} f_1 & 0 & \cdots & 0 \\ 0 & \ddots & \ddots & \vdots \\ \vdots & \ddots & \ddots & 0 \\ 0 & \cdots & 0 & f_n \end{bmatrix} \tag{2.12}$$

At this point, Equation (2.9) can be rewritten using the normalized response function matrix R', and the matrix $\boldsymbol{Eff}$ defined above, as shown in Equation (2.13) below.

$$\vec{A} = \boldsymbol{R'} \cdot \boldsymbol{Eff} \cdot \vec{N} \tag{2.13}$$

The corrected source intensity vector $\overrightarrow{N'}$, which normalizes $\boldsymbol{Eff} \cdot \vec{N}$ using the sum $|N_{Eff}| = \sum_j f_j N_j$ of each element of $\boldsymbol{Eff} \cdot \vec{N}$, is introduced according to the following Equation (2.14).

$$\overrightarrow{N'} = \frac{1}{|N_{Eff}|} \cdot \boldsymbol{Eff} \cdot \vec{N} \tag{2.14}$$

From this definition, the sum of the elements $\{N_j\}$ of the vector $\overrightarrow{N'}$ is 1. Equation (2.14) can be transformed as shown in Equation (2.15).

$$\vec{N} = |N_{Eff}| \cdot \boldsymbol{Eff^{-1}} \cdot \overrightarrow{N'} \tag{2.15}$$

Combining with Equation (2.13), we can obtain Equation (2.16)

$$\vec{A} = \left|N_{Eff}\right| \cdot \boldsymbol{R}' \cdot \overrightarrow{N'} \tag{2.16}$$

Each element of the vector $\vec{A}$ can be written as in equation (2.17).

$$A_i = \left|N_{Eff}\right| \sum\nolimits_j R'_{i,j} \cdot N'_j \tag{2.17}$$

On the other hand, if we take the sum $|A|$ of A_i and organize it, we can get the following equation.

$$\begin{aligned} |A| = \sum\nolimits_i A_i &= \sum\nolimits_i \left|N_{eff}\right| \sum\nolimits_j R'_{i,j} \cdot N'_j \\ &= \left|N_{Eff}\right| \sum\nolimits_j N'_j \sum\nolimits_i R'_{i,j} = \left|N_{Eff}\right| \end{aligned} \tag{2.18}$$

From this, if we normalize Equation (2.16) using $|\mathrm{A}|$ as $\overrightarrow{A'}$, Equation (2.9) is finally expressed by the following Equation (2.19).

$$\overrightarrow{A'} = \frac{\vec{A}}{|A|} = \frac{|N_{Eff}| \cdot \boldsymbol{R}' \cdot \overrightarrow{N'}}{|A|} = \boldsymbol{R}' \cdot \overrightarrow{N'} \tag{2.19}$$

When transformed in this way, each element $\{A'_i\}$, $\{R'_{i,j}\}$, and $\{N'_j\}$ of the matrices and vectors in Equation (2.19) can be regarded as a probability, and Bayesian estimation can be performed using them. Therefore, we rewrite the prior establishment $\mathrm{P}(E_j)$ into the corrected estimated source strength $est_j^{(k)}$, which is an expression keeping in mind the repeated application of Bayesian revision. This is an estimate of

the normalized source intensity $\overrightarrow{N'}$ defined by Equation (2.14), and therefore, as well as $\overrightarrow{N'}$, the sum of the elements $\{est_j^{(k)}\}$ of the corrected estimated source intensity vector is 1. As shown in Equation (2.20),

$$\sum_j est_j^{(k)} = 1 \tag{2.20}$$

The revised corrected estimated source strength $est_j^{(k+1)}$ is shown in the following Equation (2.21) from the correspondence with Equation (2.10),

$$est_j^{(k+1)}(i) = A'_i \cdot \frac{est_j^{(k)} \cdot R'_{i,j}}{\sum_j est_j^{(k+1)} \cdot R'_{i,j}} \tag{2.21}$$

(i) is the measured value of the i-th detector.

In addition, the following addition operation is performed to consider all measured values.

$$est_j^{(k+1)} = \sum_i \left(A'_i \cdot \frac{est_j^{(k)} \cdot R'_{i,j}}{\sum_j est_j^{(k)} \cdot R'_{i,j}} \right) \tag{2.22}$$

This yields the Bayesian revised corrected estimated source intensity $est_j^{(k+1)}$. This operation expands the meaning of Equation (2.10) derived from Bayes' theorem. In Equation (2.21), the factor A'_i, which is not in Equation (2.10), is multiplied. Finally, an addition operation is performed in Equation (2.22), which is equivalent to the operation of averaging, where multiple prior knowledge $est_j^{(k)}$ are weighted by A'_i. This operation is necessary when Bayesian revision is repeated on the aggregated data after completing the measurements. This is the idea behind the spectral Bayesian estimation method. The integral value of $est_j^{(k)}$ can be developed as the following

Equation (2.23).

$$\begin{aligned}\sum_j est_j^{(k)} &= \sum_i \sum_j \left(A'_i \cdot \frac{est_j^{(k)} \cdot R'_{i,j}}{\sum_j est_j^{(k)} \cdot R'_{i,j}} \right) \\ &= \sum_i A'_i \cdot \left(\frac{\sum_j est_j^{(k)} \cdot R'_{i,j}}{\sum_j est_j^{(k)} \cdot R'_{i,j}} \right) \\ &= \sum_i A'_i = 1 \end{aligned} \tag{2.23}$$

For the initial value of the corrected estimated source intensity, $\overrightarrow{est}^{(0)}$, we adopt the white spectrum in this study, where all elements have the same value. From Equation (2.23), the initial value is given as follows.

$$\begin{pmatrix} est_1^{(0)} \\ est_2^{(0)} \\ \vdots \\ est_{n^2}^{(0)} \end{pmatrix} = \frac{1}{n} \begin{pmatrix} 1 \\ 1 \\ \vdots \\ 1 \end{pmatrix} \tag{2.24}$$

The initial value can be determined by a known value, the measurement value. Using this and Equation (2.22), the Bayesian revision is repeated ic times to obtain the corrected estimated source strength $\overrightarrow{est}^{(ic)}$. Using $\overrightarrow{est}^{(ic)}$ instead of $\overrightarrow{N'}$ in Equation (2.14), the final estimated source intensity Nj can be obtained by solving the following Equation (2.25).

$$\vec{N} = |N_{Eff}| \cdot \boldsymbol{Eff}^{-1} \cdot \overrightarrow{est}^{(ic)} \tag{2.25}$$

This is the end of the procedure for applying Bayesian revision to image reconstruction methods for BNCT-SPECT in this study.

2.4 ML-EM

The Maximum-Likelihood Expectation Maximization method (ML-EM) is a currently used image reconstruction technique [5][6], classified as a successive approximation method. The iterative formula for this method is expressed by the following equation (2.26).

$$est_j^{(k+1)} = \frac{est_j^{(k)}}{\sum_i R_{i,j}} \sum_i \frac{A_i \cdot R_{i,j}}{\sum_{j'} R_{i,j} \cdot est_{j'}^{(k)}} \tag{2.26}$$

$est_j^{(k)}$ represents the pixel values of the k-th reconstructed image, $R_{i,j}$ is the elements of the response matrix, A_i is the measured projection data, and n is the number of detectors.

The procedure for the ML-EM method, broken down according to the calculation steps, is as follows:

1. From the i-th image $est^{(k)}$, create the i-th virtual projection data $y_i^{(k)}$. The projection equation is expressed by Equation (2.27).

$$y_i^{(k)} = \sum_{j'} R_{i,j'} \cdot est_{j'}^{(k)} \tag{2.27}$$

2. According to Equation (2-28), calculate the ratio y_i' , which is the ratio of the k-th virtual projection data to the actual measured projection data.

$$y_i' = \frac{A_i}{y_i^{(k)}} \tag{2.28}$$

3. Perform back projection on this ratio to create the image λ_j' . The back projection equation is shown in Equation (2.29).

$$\lambda_j' = \frac{1}{\sum_i R_{i.j}} \sum_i y_i' \cdot R_{i,j} \tag{2.29}$$

4. According to Equation (2.30), multiply the image λ_j', which is the back projected ratio of virtual to measured projection data, by the k-th image $est_j^{(k)}$, and update it to the (k+1)-th image.

$$est_j^{(k+1)} = est_j^{(k)} \cdot \lambda_j' \tag{2.30}$$

The initial input $\overrightarrow{est}^{(0)}$ is an image with all values set to 1. This is the general procedure of the ML-EM method, which is widely known as a successive approximation-based image reconstruction method.

2.5 Performance evaluation index

The following two types of error evaluation indices were adopted to compare the performance of the proposed Bayesian estimation method and that of the existing ML-EM image reconstruction method. [7][8]

2.5.1 MAE

The Mean Absolute Error (MAE) is the average of the absolute values of the errors [9][10]. In statistics, MAE is a measure of errors between paired observations expressing the same phenomenon, and its definition is given by Equation (2.31).

$$(MAE) = \frac{1}{N} \sum_{i=1}^{n} |est_i - t_i| \tag{2.31}$$

n represents the total number of pixels, est_i denotes the pixel values of the reconstructed image, and t_i represents the pixel values of the true image, where $|est_i - t_i|$ represents the absolute error. The smaller this value, the smaller the error

in the estimated values of the reconstructed image.

2.5.2 SSIM

The Structural Similarity Index Measure (SSIM) is devised to evaluate the structural similarity of images as perceived by the human eye and has recently become frequently used in the field of image reconstruction [11][12]. The SSIM index is a full reference metric; in other words, the measurement or prediction of image quality is based on an initial uncompressed or distortion-free image as a reference. It is calculated using Equation (2.32).

$$(SSIM) = \frac{(2\mu_t\mu_{re} + c_1)(2\sigma_{t,re} + c_1)}{(\mu_t^2 + \mu_{re}^2 + c_1)(\sigma_t^2 + \sigma_{re}^2 + c_2)} \tag{2.32}$$

μ_t is the mean of the pixel values of the true image, μ_{re} is the mean of the pixel values of the reconstructed image, σ_t^2 is the variance of the true image, σ_{re}^2 is the variance of the pixel values of the reconstructed image, and $\sigma_{t,re}$ is the covariance between the true and reconstructed images. Additionally, c_1 and c_2 can be set arbitrarily. In this study, we used the prescribed values $c_1 = (0.01 \times 255)^2$ and $c_2 = (0.03 \times 255)^2$.

From this equation, SSIM is 1 when the reconstructed and true images are perfectly matched and approaches 0 as the structural similarity decreases [13].

2.6 Summary

In Chapter 2, we provide an in-depth explanation of the Bayesian estimation method and its practical application within the BNCT-SPECT imaging framework. We begin by introducing the foundational principles of Bayesian estimation, emphasizing how it enables accurate estimation of gamma-ray distributions by iteratively updating prior probabilities based on acquired data. For this study, we use a detector array with n detectors to acquire projection data over multiple angles, resulting in a comprehensive dataset of projections for an $n \times n$ pixel true image.

To estimate each pixel value, the response matrix **R** is normalized and used in

Bayesian revisions, facilitating the reconstruction of high-resolution images for BNCT-SPECT. This approach compensates for the limited projection angles and measurement times inherent in BNCT by improving reconstruction accuracy through iterative calculations. Additionally, we introduced ML-EM, a widely used method for image reconstruction.

Finally, we introduce two critical error evaluation indices used to assess the quality of reconstructed images: Mean Absolute Error (MAE) and Structural Similarity Index Measure (SSIM). MAE quantifies the average deviation between estimated and true pixel values, providing an overall measure of reconstruction accuracy, while SSIM assesses structural fidelity by comparing patterns of luminance and contrast, thus capturing more nuanced aspects of image quality. These indices are essential in evaluating and optimizing the performance of the BNCT-SPECT imaging system.

References

[1] Iwasaki S: “A new approach for unfolding problems based only on the Bayes’ Theorem” Proceedings of the 9th International Symposium on Reactor Dosimetry (1997) pp.245-252.

[2] Lange, K. "Overview of Bayesian methods in image reconstruction." Digital image synthesis and inverse optics. Vol. 1351. SPIE, 1990. 10.1117/12.23640

[3] Iwasaki, S. “A new approach for unfolding problems based only on the Bayes’ Theorem” Proceedings of the 9th International Symposium on Reactor Dosimetry, 1997, pp.245-252.

[4] Hanson, Kenneth M. "Bayesian and related methods in image reconstruction from incomplete data." Image Recovery: Theory and Application (1987): 79-125.

[5] Cui, J., Pratx, G., Meng, B., Levin, C. S. "Distributed MLEM: An iterative tomographic image reconstruction algorithm for distributed memory architectures." IEEE transactions on medical imaging 32.5 (2013): 957-967. 10.1109/TMI.2013.2252913

[6] Boudjelal, A., Elmoataz, A., Attallah, B., Messali, Z. "A novel iterative MLEM image reconstruction algorithm based on beltrami filter: application to ECT images." Tomography 7.3 (2021): 286-300. 10.3390/tomography7030026

[7] Maulik, U., Bandyopadhyay, S. "Performance evaluation of some clustering algorithms and validity indices." IEEE Transactions on pattern analysis and machine intelligence 24.12 (2002): 1650-1654. 10.1109/TPAMI.2002.1114856

[8] Lahoulou, A., Bouridane, A., Viennet, E., & Haddadi, M. "Full-reference image quality metrics performance evaluation over image quality databases." Arabian Journal for Science and Engineering 38 (2013): 2327-2356. 10.1007/s 13369-012-0509-6

[9] Willmott, C. J., Matsuura, K. "Advantages of the mean absolute error (MAE) over the root mean square error (RMSE) in assessing average model performance." Climate research 30.1 (2005): 79-82. 10.3354/cr030079

[10] Chai, T., Draxler, R. R. Draxler. "Root mean square error (RMSE) or mean absolute error (MAE)." Geoscientific model development discussions 7.1 (2014): 1525-1534. 10.5194/gmdd-7-1525-2014

[11] Wang, Z., Bovik, A. C., Sheikh, H. R., Simoncelli, E. P. “Image quality assessment: from error visibility to structural similarity”. IEEE transactions on image processing, 13(4) 2004: 600-612.1. 10.1109/TIP.2003.819861

[12] Hore, A., Ziou, D.. "Image quality metrics: PSNR vs. SSIM." 2010 20th international conference on pattern recognition. IEEE, 2010. 10.1109/ICPR.2010.579

[13] Bakurov, I., Buzzelli, M., Schettini, R., Castelli, M., & Vanneschi, L. "Structural similarity index (SSIM) revisited: A data-driven approach." Expert Systems with Applications 189 (2022): 116087. 10.1016/j.eswa.2021.116087

Chapter 3 The experimental system

3.1 Introduction

In the previous chapter, we discussed the core features and performance of our method. Here, we provide a detailed overview of the experimental system constructed to evaluate its practical applicability. In this chapter, we present the initial construction of the experimental system, detailing each component's structure and operating principles. The primary purpose of this chapter is to evaluate the applicability of our method to existing systems by examining the functionality and integration of each part in the experimental setup. This groundwork establishes a foundation for further testing and refinement of our approach.

3.2 The configuration of the experimental system

Figure 3.1 shows the simplified experimental system used in this study. To simulate brain tumors emitting gamma-rays during neutron irradiation, we constructed a head phantom containing a ^{137}Cs source, which was strategically placed at various locations. This source, selected for its monochromatic gamma emission near 478 keV, approximates the gamma-ray characteristics expected in BNCT. A standard ^{137}Cs gamma-ray source with an intensity of 1.0×10^{7} Bq was used for the experiments. In this setup, gamma-rays were detected, and the total measured value was calculated. To derive the response matrix element, this total value was divided by the product of the source intensity in becquerels (Bq) and the measurement time in seconds (s), yielding the normalized detection response.

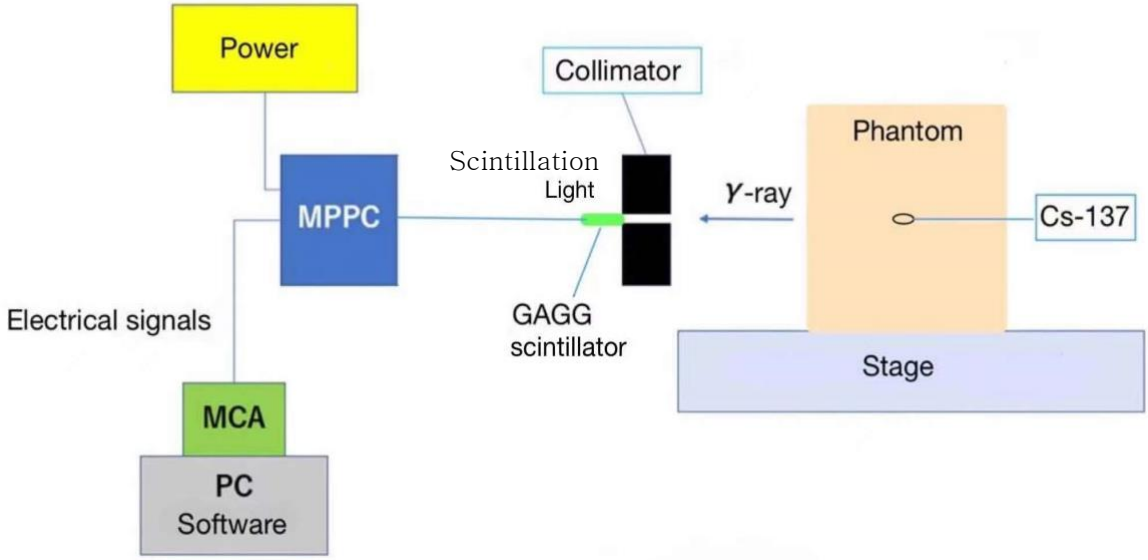

Figure 3.1 Simplified experimental system

Table 3.1 Equipment of the experimental system

Equipment	Product model
Motorized stage (rotation)	SIGMAKOKI OSMS-120YAW
Motorized stage (translation)	SIGMAKOKI OSMS26-200
Stage controller	SIGMAKOKI SHOT-702
MPPC	HAMAMATSU MPPC C14047-9955
MCA	AMTEK MCA8000D

The phantom is positioned on a stage, allowing emitted gamma rays to be directed accurately through a lead collimator toward the GAGG scintillation detector. This collimation ensures that gamma rays are captured precisely from the intended locations within the phantom, based on the field of view of each detector. Using this setup, we obtain the spatial energy distribution of gamma rays throughout the phantom, facilitating a detailed analysis of radiation behavior at different locations.

Table 3.1 lists the equipment used in the experimental system. The motorized stage enables precise control over the position and orientation of the phantom, allowing for targeted adjustments of which part of the phantom enters the detector's field of view. This setup ensures that specific areas can be consistently analyzed, optimizing data acquisition and improving the accuracy of gamma-ray distribution measurements

within the phantom.

3.3 GAGG scintillator

3.3.1 Inorganic scintillator

When radiation enters certain types of materials, the electrons within these materials are elevated to a high-energy state (excited state). As they return to their original state (ground state), they release the energy difference in the form of light, or fluorescence. This phenomenon is known as scintillation, and materials that exhibit this property are called scintillators. Since the emitted light is usually very faint, scintillators are often paired with devices such as photomultiplier tubes, which amplify the weak light signal into a readable electronic signal.

Scintillators are broadly categorized into two types: inorganic and organic scintillators. Inorganic materials generally offer superior light output and linearity, although most have relatively long response times. Due to their high atomic numbers and densities, inorganic scintillators are particularly well-suited for gamma-ray spectroscopy. On the other hand, organic scintillators tend to have fast response times, though they produce lower light output. They are commonly used for beta-ray spectroscopy and, because they contain hydrogen, are also effective for neutron detection. [1] In this study, an inorganic scintillator was employed as the gamma-ray detector, so the following will focus on the properties and characteristics of inorganic scintillators.

In inorganic materials, the scintillation mechanism is determined by the energy states defined by the crystal lattice structure. As shown in Figure 3.2, electrons within an insulator or semiconductor material are restricted to specific energy bands. Valence band electrons are bound to specific lattice positions, while conduction band electrons have sufficient energy to move freely within the crystal. Between these bands lies a forbidden gap, an energy range where electrons cannot exist in a pure crystal. In pure crystals, the process of an electron in the conduction band returning to the valence band by emitting a photon is inefficient. Additionally, the width of this gap results in photons with energy levels too high to produce visible light, making the scintillation process

ineffective for practical applications without specific modifications.

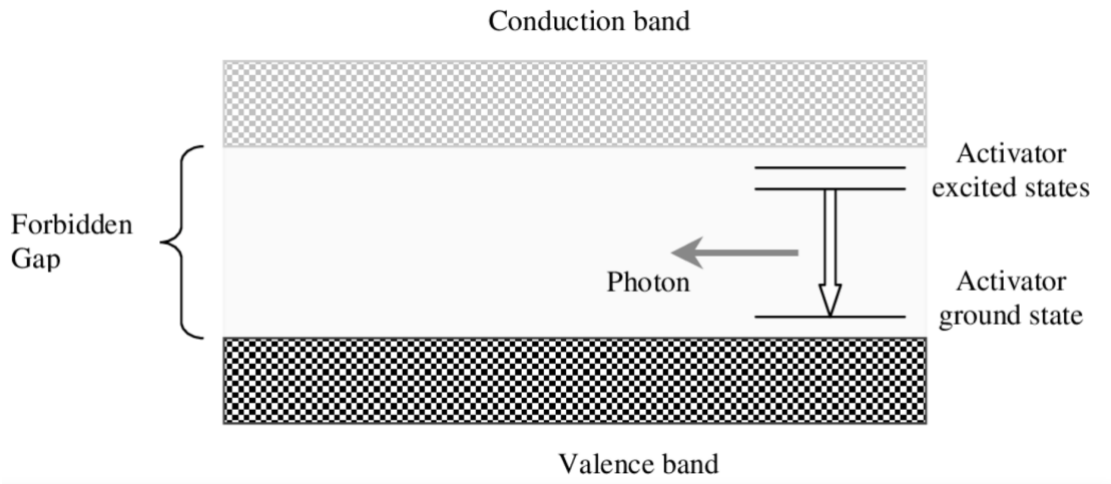

Figure 3.2 Energy band structure and scintillation mechanism of an activated crystalline scintillator. [5]

To enhance the probability of visible light emission through transition processes, inorganic scintillators are typically doped with a small amount of impurity, known as an activator. This activator creates specific sites within the crystal lattice and alters the structure of the energy bands in the pure crystal. Consequently, new energy states are formed within the forbidden gap, allowing electrons to transition more effectively from the conduction band to the valence band. These transitions release energy in the form of visible photons, thereby increasing the scintillation efficiency of the material.

3.3.2 Scintillator Properties

For scintillators used in radiation measurement, characteristics such as luminescence intensity and decay time are carefully considered based on the type of radiation being measured and the specific purpose of the measurement. This section provides an overview of these fundamental characteristics, and in the following section, we discuss the rationale behind selecting the GAGG(Ce) scintillator, taking these properties into account.

1. Atomic Number and Density

Inorganic scintillators, primarily used for gamma-ray measurement, achieve

higher detection efficiency for gamma rays when composed of materials with a higher atomic number. This is due to an increased probability of interactions, particularly the photoelectric effect, which enhances the ability to detect gamma rays effectively.

2. Luminescent Wavelength

The emission spectrum of scintillator crystals varies depending on the type of crystal used. To maximize the utilization of scintillation light, this spectrum mus t align closely with the wavelength range of the photodetector's peak sensitivity. This matching optimizes the efficiency of light detection, ensuring that the maximum amount of scintillation light contributes to the detection process.

3. Attenuation Constant

The luminescence produced by a scintillator decay exponentially over time. Although many inorganic scintillators exhibit more than one decay component, in most cases, only the primary decay component is considered for practical purposes. If we denote the decay time of fluorescence as τ and the initial luminescence intensity as I_0, the luminescence intensity I at time t after excitation can be expressed by Equation (3.1):

$$I = I_0 \cdot e^{-\frac{t}{\tau}} \tag{3.1}$$

This exponential decay behavior is crucial for determining the timing characteristics of scintillation detectors, as it influences the resolution and count rate capability in radiation detection applications.

4. Luminescence Yield

Luminescence yield refers to the number of photons emitted when 1 MeV of energy is deposited in the scintillator. This measure is critical for evaluating the efficiency of a scintillator material in converting the energy of incoming radiation into detectable light. High luminescence yield is desirable, as it leads to stronger signals and improves the precision and accuracy of radiation detection.

3.3.3 Selection of GAGG(Ce) scintillators

Figure 4 illustrates the GAGG scintillator implemented in the mock-up experiments, selected due to its favorable properties tailored for BNCT-SPECT systems.

Firstly, in systems utilizing inorganic scintillators, achieving optimal detection performance demands that the scintillator material possesses high density and a suitable atomic number, as these factors contribute directly to the material's gamma-ray detection efficiency by increasing photon interaction probabilities within the detector volume. The high atomic number enhances photoelectric interactions, which is particularly beneficial for detecting low-energy gamma rays.

Secondly, achieving fine energy resolution is critical to accurately separate the 478 keV gamma rays from the nearby 511 keV annihilation gamma rays, as overlapping peaks would otherwise compromise the reconstruction accuracy. Thus, it is essential for the material to exhibit high luminescence yield under gamma-ray interaction, generating a sufficient number of photons per incident gamma event. This reduces statistical variations in photon count, leading to improved energy resolution and allowing for a precise distinction between close energy peaks.

Finally, another essential property for BNCT-SPECT applications is the scintillator's decay time. A short decay time minimizes signal overlap from successive events, which is vital for maintaining high count rates without substantial dead-time losses, especially under the high-flux conditions often encountered in clinical BNCT settings. The absence of intrinsic self-radiation further reduces background noise, which is beneficial for low-background measurements in medical imaging.

Table 3.2 presents the properties of various inorganic scintillators [2]. For this study, we selected a Ce-doped GAGG (Gadolinium Aluminum Gallium Garnet; $Gd_3Al_2Ga_3O_{12}$: Ce) scintillator from among the options. Figure 3.5 shows the GAGG(Ce) scintillator crystal used in the experiments. GAGG(Ce) is a recently developed scintillator crystal and has several advantages compared to traditional scintillator crystals, such as NaI and CsI. Notably, it offers a high density of 6.63 g/cm^3 [3] and excellent energy resolution of 6.3% at 662 keV for ^{137}Cs gamma rays.

While other scintillators like LuAG(Pr) and $LaBr_3$(Ce) could also be potential candidates due to their comparable resolution and density, each presents limitations. LuAG(Pr), for instance, has a short emission wavelength of 312 nm, making it incompatible with the silicon-based photodetectors used for small-scale and arrayed configurations, such as the Multi-Pixel Photon Counter (MPPC) intended for this system. $LaBr_3$(Ce), on the other hand, is deliquescent, posing handling and durability challenges in typical lab or clinical environments.

Therefore, GAGG(Ce) was chosen for this study due to its favorable properties and compatibility with the MPPC detection system, which will be explained in detail in the following section. In this research, a 3.5×3.5×30 mm^3 GAGG(Ce) is used considering the spatial resolution is 5mm or less, and the statistical accuracy is less than 4.39% [4]. This selection allows for effective gamma-ray detection while ensuring system reliability and ease of maintenance in practical applications.

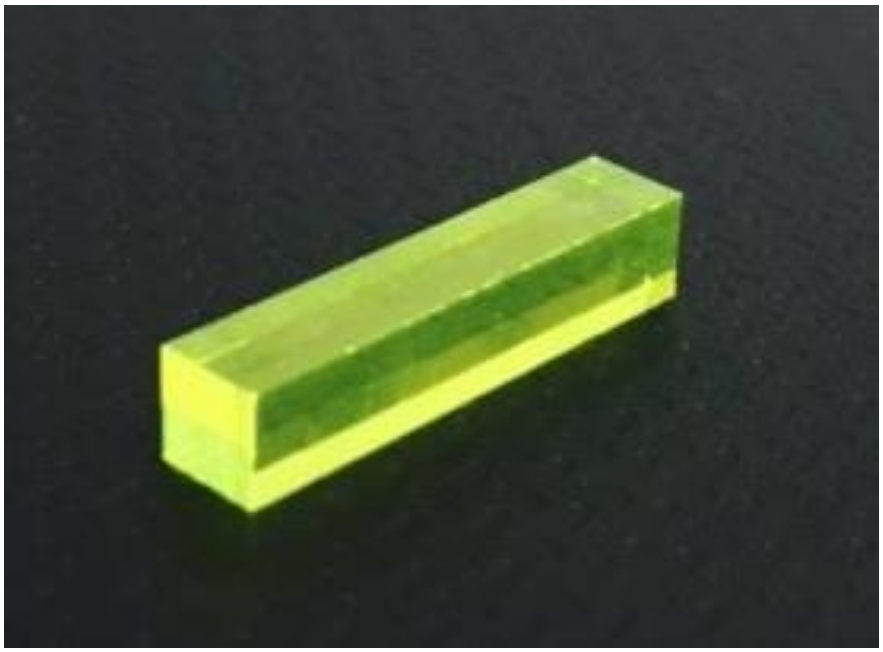

Figure 3.5 GAGG scintillator used in the experiments

(Left: before shielding Right: after shielding)

Table 3.2 Performance comparison of major inorganic scintillators

Scintillator	GAGG (Ce)	NaI (Tl)	CsI (Tl)	$LaBr_3$ (Ce)	LuAG (Pr)	BGO
Intensity [g/cm^3]	6.63	3.67	4.53	5.08	6.7	7.13
Luminous Intensity [photon/MeV]	60,000	45,000	56,000	75,000	22,000	8,000
Deliquescence	No	Yes	Yes	Yes	No	No
Energy Resolution [%@Cs-662keV]	6.3	5.6	5.7	2.6	4.2	12
Luminescent Wavelength [nm]	520	415	550	375	312	480
γ-ray Stopping Power $\rho Zeff^4[\times 10^6]$	43	25	38	25	79	186

3.3.4 Detection efficiency

The performance of gamma-ray detectors is primarily evaluated through two key metrics: counting efficiency and energy resolution. To understand intrinsic efficiency, we first define counting efficiency. Counting efficiency represents the ratio between the

number of pulses counted by a radiation detector and the activity of the radiation source. A higher counting efficiency indicates a more effective detector, as it captures a larger portion of the emitted radiation, making it well-suited for sensitive and precise measurements. Intrinsic efficiency builds upon this by considering the detector's inherent ability to detect gamma-rays independently of external factors.

All radiation detectors output pulse signals as a result of interactions between incident radiation and the sensitive volume within the detector. For charged particles, such as alpha and beta particles, interaction is inevitable once the particle enters the sensitive volume, generating a sufficient number of electron-hole pairs along its path. This interaction produces a detectable pulse signal. Therefore, in the case of charged particles, detection is guaranteed as long as the particle enters the sensitive volume, ensuring reliable detection within the specified range of the detector.

In contrast, uncharged particles such as X-rays, gamma rays, and neutrons, due to their lack of charge and high penetration capability, often pass through the detector without interacting. Occasionally, they do interact with the detector, and the resulting charged particles generated from these interactions can then be detected. Consequently, the detection efficiency for uncharged particles is generally less than 100%, making it essential to precisely determine the counting efficiency.

Counting efficiency can be categorized into two types: absolute efficiency (ε_{abs}) and intrinsic efficiency (ε_{int}). Absolute efficiency depends not only on the characteristics of the detector but also on the distance between the radiation source and the detector. Absolute efficiency and intrinsic efficiency are defined by the following Equations (3.2) and (3.3), respectively:

$$\varepsilon_{abs} = \frac{\text{Number of pulses detected}}{\text{Total radiation emitted by the source}} \tag{3.2}$$

$$\varepsilon_{int} = \frac{\text{Number of pulses detected}}{\text{Radiation entering the detector's sensitive volume}} \tag{3.3}$$

For an isotropic radiation source, these two types of efficiency are related, as shown

in Equation (3.4). Here, Ω represents the solid angle subtended by the detector from the position of the source. As indicated by Equation (3.4), intrinsic efficiency is less dependent on the detector's position relative to the source compared to absolute efficiency.

$$\varepsilon_{int} = \varepsilon_{abs} \cdot \frac{4\pi}{\Omega} \tag{3.4}$$

In this measurement, the denominator of Equation (3.3) is determined using Equation (3.5). In Equation (3.5), S represents the detector's entrance area, r is the distance between the source and the detector, and Bq denotes the standard source activity. Additionally, T is the half-life of the standard source, and t indicates the elapsed time since the calibration date of the standard source. The emission ratio represents the fraction of gamma rays emitted per decay event of the standard source.

$$\text{Radiation entering the detector's sensitive volume} = \frac{S}{4\pi r^2} \times Bq \times \left(\frac{1}{2}\right)^{\frac{t}{\tau}} \times \text{emission ratio} \times detection\ tim \tag{3.5}$$

3.3.5 Energy resolution

One of the key characteristics of a radiation detector is its energy resolution, which can be evaluated by observing the detector's response to a monoenergetic radiation source.

Figure 3-6 shows the formal definition of the energy resolution of a detector. The width $\Gamma(E_0)$ at half of the peak maximum is referred to as the Full Width at Half Maximum (FWHM). The detector's ability to discriminate particles at the energy peak E_0 is known as the energy resolution $R(E_0)$, which is defined by Equation (3.6). Here, $\Gamma(E_0)$ is expressed in units of energy, while $R(E_0)$ is dimensionless.

$$R(E_0) = \frac{\Gamma(E_0)}{E_0} \tag{3.6}$$

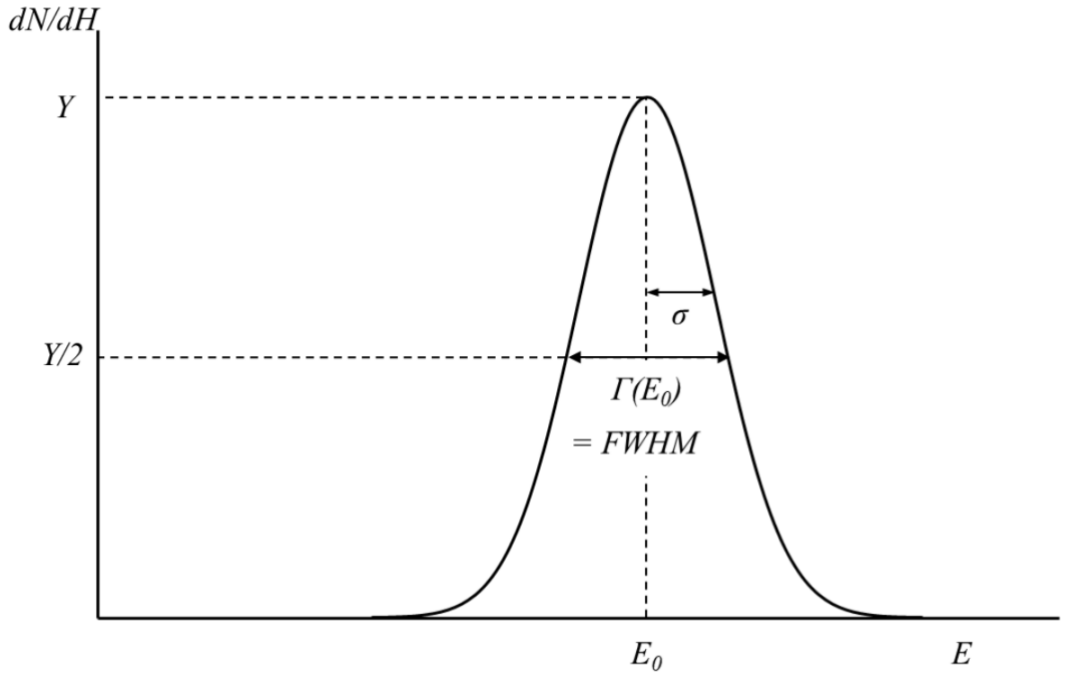

Figure 3.5 Definition of the energy resolution of a detector.

The factors affecting the energy resolution of a detector's response can be categorized into the following three aspects:

1. Statistical fluctuations in the number of electron-hole pairs created within the detector – These fluctuations arise from the inherent randomness in the particle interactions within the detector material.
2. Electronic noise from the detector body or connected circuitry – This includes noise introduced by vibrations, electromagnetic fields, and other sources that can interfere with the signal processing.
3. Imperfect creation of electron-hole pairs within the detector – This factor stems from irregularities in the semiconductor crystal structure, which can lead to incomplete or inconsistent electron-hole pair formation.

Each of these factors contributes to broadening the detector's response function, thereby impacting its energy resolution.

Among these factors, the statistical fluctuations in the number of electron-hole pairs

(factor 1) are the most significant. This is because factors 2 and 3 contribute a baseline level of noise that cannot be eliminated, even with a perfectly constructed detector; they represent unavoidable fluctuations present in any detector signal. The number of electron-hole pairs generated within the detector due to radiation is inherently discrete and varies, even when the incoming energy is the same. This discrete nature of electron-hole pair production introduces statistical noise, which affects the consistency of the signal and thus the energy resolution of the detector.

Suppose radiation enters the detector, depositing an energy E. If the average energy required to produce one electron-hole pair in the scintillator is ε, then the average number of electron-hole pairs N produced can be expressed by the following Equation (3.7):

$$N = \frac{E}{\varepsilon} \tag{3.7}$$

In radiation measurements, N is typically a large value, meaning that if it were the only source of signal fluctuation, the distribution of counts would follow a Gaussian distribution, as shown in Figure 3.5 (or a Poisson distribution if the count numbers are low). Thus, the relationship between the standard deviation σ and the measured count of electron-hole pairs N is given by Equation (3.8):

$$\sigma = \sqrt{\frac{E}{\varepsilon}} = \sqrt{N} \tag{3.8}$$

Additionally, a Gaussian distribution can be expressed as shown in Equation (3.9):

$$G(E) = \frac{A}{\sigma\sqrt{2\pi}} \exp\left(-\frac{(E - E_0)^2}{2\sigma^2}\right) \tag{3.9}$$

From this distribution, theFWHM, denoted as Γ, can be determined using the

relationship given in Equation (3.10):

$$\Gamma = 2\sqrt{2ln2}\sigma \approx 2.355\sigma \tag{3.10}$$

Here, A represents the peak area. Generally, there is a proportional relationship between the pulse height E_0 and the number of electron-hole pairs N, which can be expressed as $E_0 = KN$, where K is a proportional constant. Given that the standard deviation σ of the pulse height spectrum is related to the pulse height, we can convert it to energy using Equation (3.8), resulting in: $\sigma = K\sqrt{N}$. Substituting this into Equation (3.10), the FWHM becomes: $\Gamma = 2\sqrt{2ln2}\sigma \approx 2.355K\sqrt{N}$. Equation (3.11) provides the energy resolution R as a function of N, indicating how statistical variations influence the precision of energy measurements.

$$R = \frac{\Gamma}{E_0} = \frac{2.355K\sqrt{N}}{KN} = \frac{2.355}{\sqrt{N}} \tag{3.11}$$

From Equation (3.11), we can see that the energy resolution R depends solely on the number of counted electron-hole pairs N; the larger N is, the better the resolution. However, in practice, individual electron-hole pair creation events are not entirely independent, and the variance in N is smaller than what would be expected from a Poisson process. To quantify this deviation from the Poisson process in electron-hole pair generation, the Fano factor F is introduced, which is defined by Equation (3.12).

The Fano factor adjusts the expected variance, accounting for the sub-Poissonian behavior observed in real materials, thus providing a more accurate representation of statistical fluctuations in radiation detection.

$$F = \frac{The\ variance\ in\ the\ total\ measured\ number\ of\ electron-hole\ pairs\ N}{The\ expected\ variance\ N\ in\ an\ ideal\ Poisson\ distribution} = \frac{\sigma_{abs}^2}{N} \tag{3.12}$$

Here, σ_{abs} represents the standard deviation adjusted by the Fano factor F, and it is given by Equation (3.13):

$$\sigma_{abs} = \sqrt{FN} \tag{3.13}$$

The value of the Fano factor F ranges between 0 and 1. Therefore, considering the Fano factor, the FWHM Γ can be expressed in relation to the adjusted standard deviation σ_{abs} as shown in Equation (3.14):

$$\Gamma = 2\sqrt{2ln2}K\sigma_{abs} \approx 2.355K\sigma_{abs} \tag{3.14}$$

Additionally, from Equations (3.13) and (3.14), we can derive Equation (3.15):

$$\Gamma = 2.355K\sqrt{FN} \tag{3.15}$$

The energy resolution R, as determined by the Fano factor, is equivalent to the expression given in Equation (3.6).

$$R = \frac{\Gamma}{E_0} = \frac{2.35K\sqrt{N}\sqrt{F}}{KN} = 2.355\sqrt{\frac{F}{N}} \tag{3.16}$$

This R is known as the "Fano limit." In scintillation detectors, the value of F is typically 1. In this study, we use Γ, which is more intuitive for assessing energy resolution, as the primary parameter. By rearranging Equation (3.15) using Equation (3.8) and taking the logarithm of both sides, we obtain Equation (3.17),

$$log_{10}(\Gamma) = \frac{1}{2}log_{10}(\mathrm{E}) + C \tag{3.17}$$

where C is a constant independent of E. This transformed expression allows for a simplified analysis of energy resolution using Γ as a key parameter.

This relationship highlights that the statistical variation in the signal, represented by the standard deviation, is proportional to the square root of the number of detected electron-hole pairs. This variance influences the precision of energy measurements within the detector.

3.4 MPPC

MPPC stands for Multi-Pixel Photon Counter, a type of device known as a Si-PM (Silicon Photomultiplier). It is a photodetector that operates in Geiger mode, utilizing an array of avalanche photodiodes (APDs) arranged in multiple pixels to enhance photon detection capabilities. The main characteristics of MPPCs are as follows, with an image of the MPPC used in this study shown in Figure 3.6. [6]

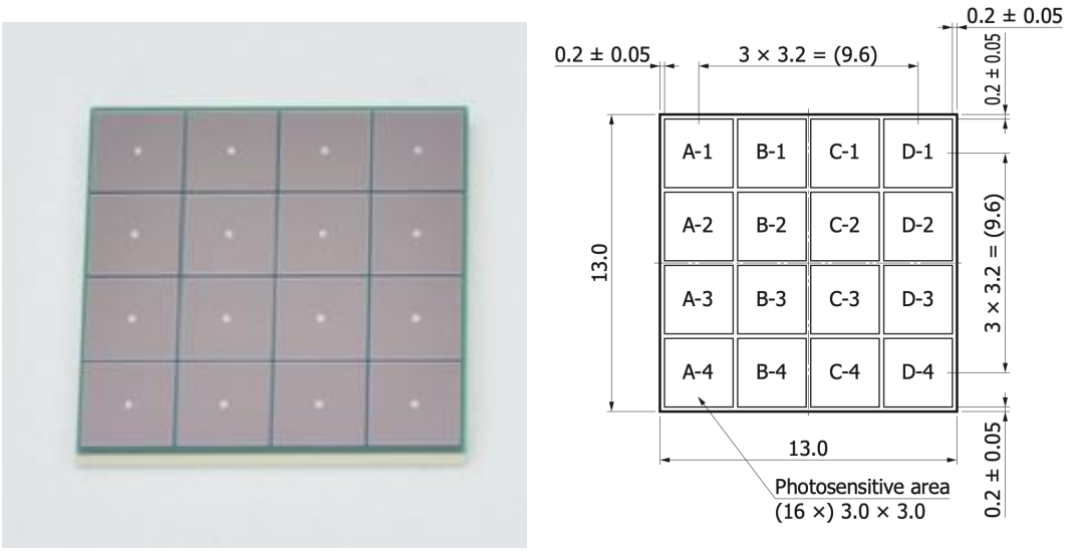

Figure 3.6 MPPC dimensional outlines

The main features of MPPCs are as follows:

1. Compact and Cost-Effective: MPPCs are small in size and relatively inexpensive compared to other photodetectors.
2. Operates at Low Bias Voltage: They require only a low bias voltage for

operation, making them energy-efficient and easy to handle.

3. High Quantum Efficiency: MPPCs have a high quantum efficiency, enabling efficient photon detection.

4. Fast Response: They exhibit high-speed response, suitable for applications requiring rapid signal processing.

5. Resistant to Magnetic Fields: MPPCs are less affected by magnetic fields, making them reliable in environments with strong electromagnetic interference.

These characteristics make MPPCs highly versatile and effective for use in photon detection applications, including those in this study.

3.4.1 Operating principle

Before explaining the operating principle of the MPPC, it is essential to understand the fundamental component behind its operation: the APD (Avalanche Photodiode). An APD is a highly sensitive photodiode that amplifies photocurrent by applying a specific reverse voltage. While the mechanism for generating photocurrent in an APD is similar to that of a conventional photodiode, the key difference lies in the APD's ability to multiply the generated charge carriers, enhancing its sensitivity compared to standard photodiodes.

When light with energy exceeding the bandgap enters a photodiode, electron-hole pairs are generated as a result of the light energy. When a reverse voltage is applied to a p-n junction, the electron-hole pairs produced within the depletion region drift under the influence of the electric field. The drift velocity of these carriers increases as the electric field strengthens. At a certain field strength, known as the breakdown voltage, the frequency of collisions between carriers and the crystal lattice increases, reaching a point where it saturates.

As the electric field further increases, carriers that avoid collisions with the lattice gain very high energy. When such high-energy carriers eventually collide with the crystal lattice, they generate additional electron-hole pairs, a process known as ionization. This ionization can trigger a chain reaction where newly created electron-hole pairs

themselves initiate further ionization, a phenomenon referred to as avalanche multiplication. A photodiode that amplifies the signal via avalanche multiplication is known as an APD. This process enables APDs to achieve significant signal amplification, making them highly sensitive detectors for low-level light signals. [7][8]

When an APD is operated with a reverse voltage exceeding the breakdown voltage, it detects a fixed signal regardless of the number of incident photons. This phenomenon is known as Geiger discharge, and the operation of an APD under such a voltage is referred to as Geiger mode. To stop the Geiger discharge and prepare the APD for detecting the next photon, the operating voltage must be reduced.

To achieve this, a quenching resistor is connected in series with the APD, as shown in Figure 3.7. During Geiger discharge, the current generated causes a voltage drop across the quenching resistor, which lowers the APD's operating voltage, effectively halting the discharge. The output current from Geiger discharge has a sharp rising edge, forming a pulse-like signal, while the falling edge of the output current, regulated by the quenching resistor, has a gradual slope, resulting in a smoothed pulse shape.

This quenching mechanism ensures the APD is ready for subsequent photon detection, making it suitable for applications requiring high sensitivity and precise detection timing.

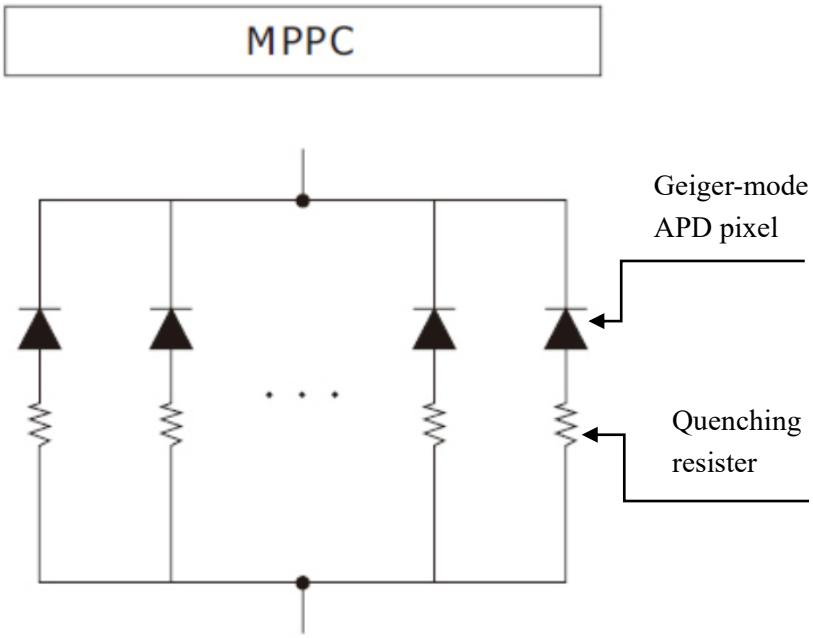

Figure 3.6 Structure of MPPC

3.4.2 MPPC Properties

The MPPC has various characteristics, some of which are highlighted below.

1. Gain

The gain M of an MPPC is defined as the ratio of the charge Q generated by a single pixel detecting one photon to the elementary charge e. It can be expressed by Equation (3.18):

$$M = \frac{Q}{e} \tag{3.18}$$

Here, e is the elementary charge, given as 1.60×10^{-19} C. This gain represents the level of signal amplification achieved by the MPPC for detecting individual photons.

The charge Q depends on the reverse voltage V_R and the breakdown voltage V_{BR}, as expressed in Equation (3.19):

$$Q = C \times (V_R - V_{BR}) \tag{3.19}$$

where C represents the capacitance of a single pixel. This relationship indicates that the charge generated by each pixel is proportional to the difference between the reverse voltage and the breakdown voltage, with the pixel capacitance acting as a scaling factor.

Equations (3.18) and (3.19) indicate that the gain M increases with both a larger pixel capacitance C and a higher reverse voltage V_R. This means that the amplification capability of the MPPC is enhanced when the capacitance of each pixel is greater or when a higher reverse voltage is applied, as both factors contribute to a larger charge Q generated per detected photon.

2. Dark Count

In an MPPC, pulses can also be generated by thermally produced carriers, which are known as dark pulses. These thermally induced carriers are amplified to a consistent signal level and are observed alongside actual signals, potentially causing detection errors. The rate of dark counts increases with rising ambient temperature, as higher temperatures promote the generation of thermal carriers. This dark count rate is an important factor to consider in applications requiring high sensitivity and low noise.

3. Crosstalk

In an MPPC, when a single photon enters one pixel, it is sometimes possible to observe two or more pulses. This occurs when secondary photons generated during the avalanche process in one pixel enter an adjacent pixel, triggering an additional avalanche and causing a detectable signal in the neighboring pixel. This phenomenon is known as optical crosstalk.

The probability of crosstalk is largely independent of temperature within the operating temperature range but increases with higher reverse voltage. As the reverse voltage rises, the likelihood of secondary photons inducing signals in neighboring pixels also rises, thereby increasing the frequency of crosstalk events. This effect must be managed to maintain signal accuracy in high-sensitivity applications.

4. Photosensitivity and Detection Efficiency

Two key characteristics that indicate the optical detection sensitivity of an MPPC are

photosensitivity and detection efficiency. Photosensitivity is defined as the ratio of the MPPC's output current to the amount of incident light when continuous light is directed onto the MPPC. In contrast, detection efficiency refers to the ratio of detected photons to the number of incident photons when pulsed light is used for photon counting with the MPPC.

Since photosensitivity is proportional to the gain, it increases with the reverse voltage applied to the MPPC. However, it is essential to note that photosensitivity includes contributions from effects such as crosstalk, which may artificially enhance the measured sensitivity. Therefore, careful interpretation is required when evaluating photosensitivity, especially in applications where high precision is necessary.

3.5 MCA

The MCA8000D is a state-of-the-art, high-performance multichannel analyzer (MCA) developed by Amptek. It serves as an upgrade to the MCA8000A, which has been a reliable tool in spectroscopic applications for over 15 years. The MCA8000D incorporates modern digital signal processing technology and features contemporary high-speed USB and Ethernet interfaces, addressing the obsolescence issues associated with the MCA8000A's architecture.

An MCA is a critical component of a complete instrumentation system, widely used in applications requiring detailed signal analysis. Typically, a sensor generates a series of current pulses as its signal in response to incoming radiation or particles. Signal processing electronics then shape these pulses into forms where the peak voltage corresponds directly to a quantity of interest, such as the deposited energy or particle size.

The MCA processes these shaped pulses and outputs a pulse height spectrum, which is essentially a histogram of pulse heights. This spectrum provides valuable insights into the distribution of energies or other properties of the detected particles, making the MCA an essential tool in spectroscopic and particle detection applications.

The MCA operates by detecting the peak voltage of each shaped pulse and converting it into a digital value. This digital value is proportional to the peak voltage of the pulse.

For instance, with a 10-bit resolution, the MCA divides the full voltage scale into 1024 channels. For a gain setting of 1V full scale, a pulse with a peak voltage of 0.5V would be assigned to channel 512.

Each time a pulse's peak falls into a particular channel, the MCA increments the counter for that channel. The resulting array of integer counter values constitutes the pulse height spectrum, which is the MCA's primary output. This spectrum is either displayed directly or transmitted to spectrum processing software for further analysis.

In addition to the histogram, the MCA provides supplementary data, including the total measurement time, a dead time correction factor, and the total number of counts detected. These outputs enhance the utility of the MCA in applications requiring precise spectroscopic measurements. [9]

Figure 3.7 shows the dimensions of the MCA used in this study.

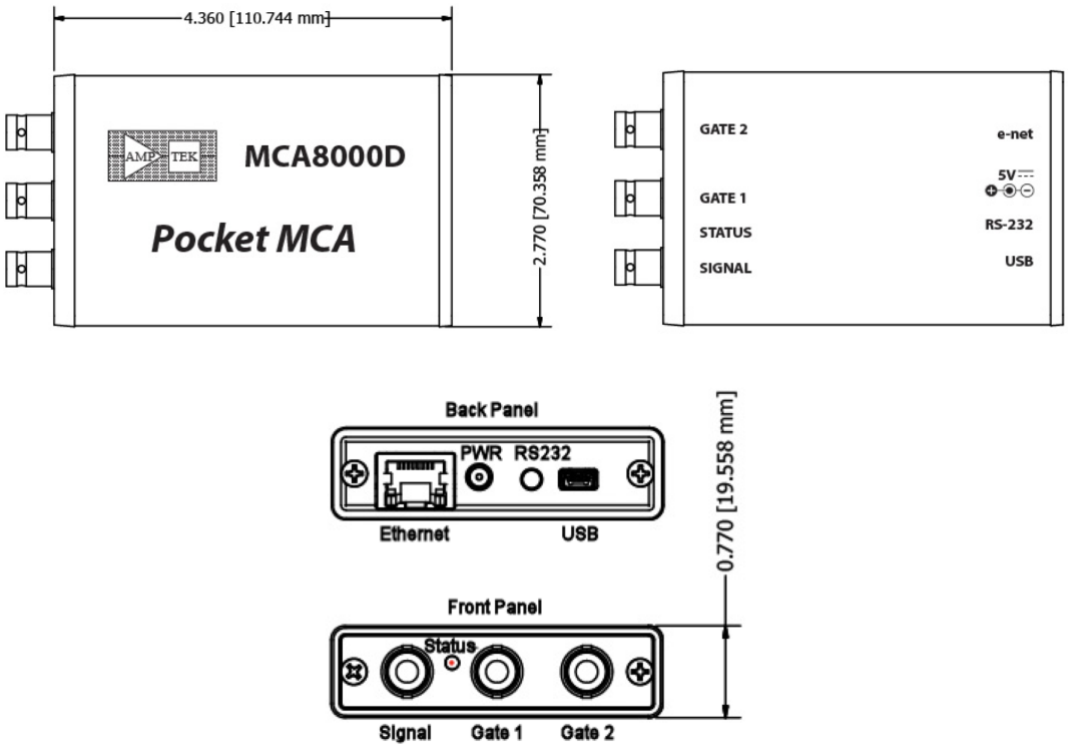

Figure 3.7 Dimensions of MCA8000D

The MCA8000D incorporates a threshold parameter that is configurable through software and plays a key role in the peak detection logic. For a pulse to be recognized

as having a peak, its height must exceed the threshold value, and then it must fall below the peak by the threshold amount. Typically, the MCA only records pulses that are above this threshold. However, in the case of bipolar pulses, it is possible for below-threshold pulses to be recorded.

Additionally, the MCA8000D features a separate parameter known as the LLD (low-level discriminator). Unlike the threshold parameter, the LLD functions strictly as a lower cutoff, ensuring that only pulse heights exceeding this limit are recorded. This dual-threshold system enables the MCA8000D to filter unwanted low-amplitude signals effectively while maintaining flexibility for various signal processing scenarios.

In our experimental system, it is common practice to measure the spectrum of a sample containing at least two peaks of known energies. These known energies are used to correlate the measured centroids of the peaks, allowing for the calibration of not only the MCA but also the entire signal processing chain, including the detector, preamplifier, and shaping amplifier.

Since the characteristic energies of X-rays and gamma rays are universal physical constants, there is no requirement for NIST-traceable calibrations; the system is calibrated against these fixed constants. However, it is essential to have a spectrum containing peaks with known energies to perform this calibration accurately. This approach ensures that the energy scale of the system is correctly aligned with the physical properties of the incident particles.

By combining the MCA functionality described in this section with the GAGG detector discussed in Section 3.3.3 and the explanation of energy resolution in Section 3.3.5, the energy resolution of the GAGG detector used in this experiment can be determined. The experimental results for the FWHM, which is for the energy resolution, are presented in Table 3.3, with the corresponding graph depicted in Figure 3.8.

Table 3.3 FWHM measurement results

Source	E/MeV	R	FWHM
Co	1.33249	0.039347	0.05243
Eu	1.40801	0.038305	0.053934
Cs	0.66166	0.05507	0.036438
Na	0.551	0.060009	0.033065
	1.27454	0.040207	0.051246
Ba	0.356	0.073259	0.02608

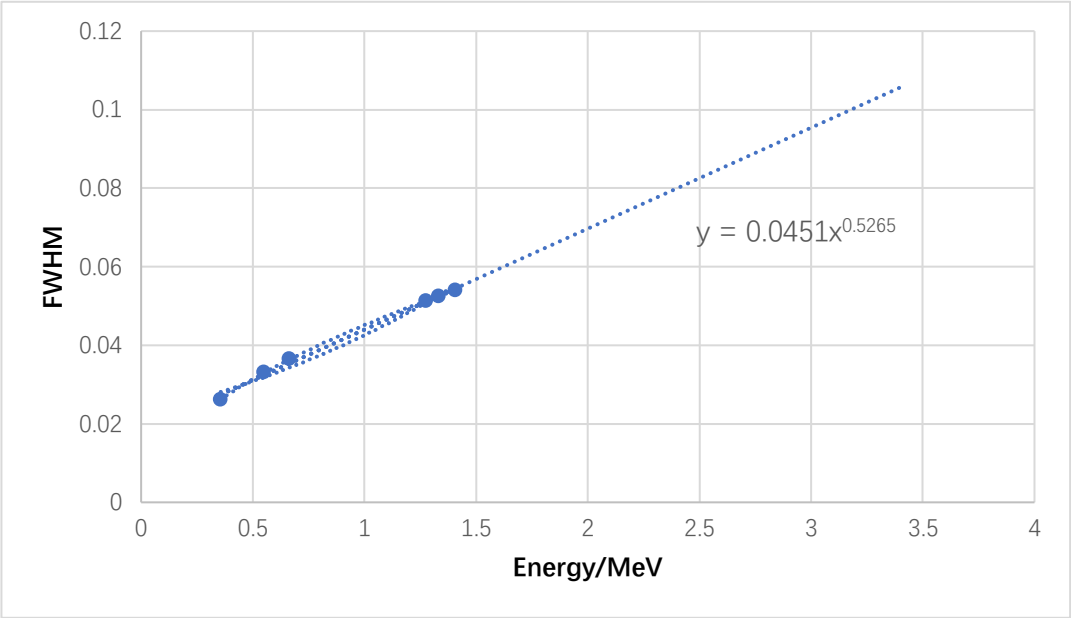

Figure 3.8 Measurement results of FWHM

The relationship between FWHM and energy observed in our experiments is expressed in Equation (3.20).

$$\Gamma = 0.0451E^{0.5625} \tag{3.20}$$

3.6 Design of phantom

Figure 3.9 illustrates the human head phantom used in the experiments. A cylindrical

phantom with a diameter of 20 cm and a height of 20 cm, made of acrylic and water, was developed. This phantom was placed on a stage that allowed for free adjustment of its position and rotation. Since the position of the detector could not be altered due to the setup of the experimental system, the stage was utilized to change the position of the simulated tumor, effectively replicating the position change of the detector. An adjustable acrylic platform was incorporated into the phantom to enable precise placement and height adjustment of the gamma-ray source, simulating a tumor. The right-hand portion of the figure depicts the Monte Carlo N-Particle 5 (MCNP5) simulation model of the experimental system. MCNP, a general-purpose three-dimensional Monte Carlo N-particles transport code, is employed to simulate particle motion in various environments, replicating natural conditions. Further details on MCNP5 will be provided in Chapter 4.

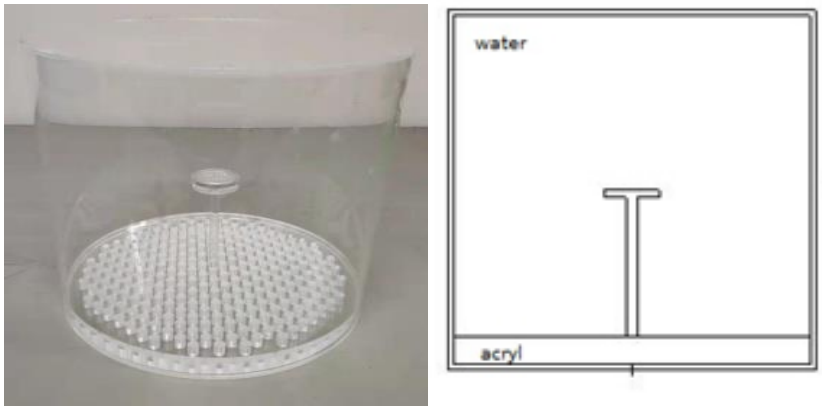

Figure 3.9 Phantom used in the experiments

In this study, we adopted a grid system of n=50, representing the image area, and positioned the head phantom within this grid. As shown in Figure 3.10, the black region represents the observation area, a square with a side length of 20 cm, resulting in a pixel size of 0.4^2 cm^2. The white circle denotes the border of the phantom, which is made of acrylic and has a thickness of 0.3 cm. This configuration provides a detailed framework for the imaging and analysis of gamma-ray distributions within the phantom.

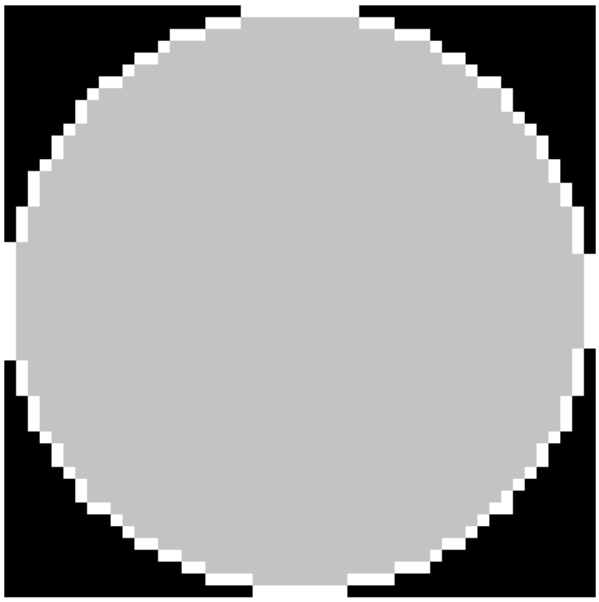

Figure 3.10 Head phantom placed in the observation area

3.7 Experimental procedure

Based on the head constructed above, the gamma-ray source can be positioned within the brain region to simulate cancer cells. For instance, as shown in Figure 3.11, the red point represents the gamma-ray source, while the green blocks indicate the GAGG scintillator array. The gray area corresponds to the brain, with a diameter of 48 pixels. This setup enables a realistic simulation of gamma-ray emissions and their detection within the brain region of the phantom.

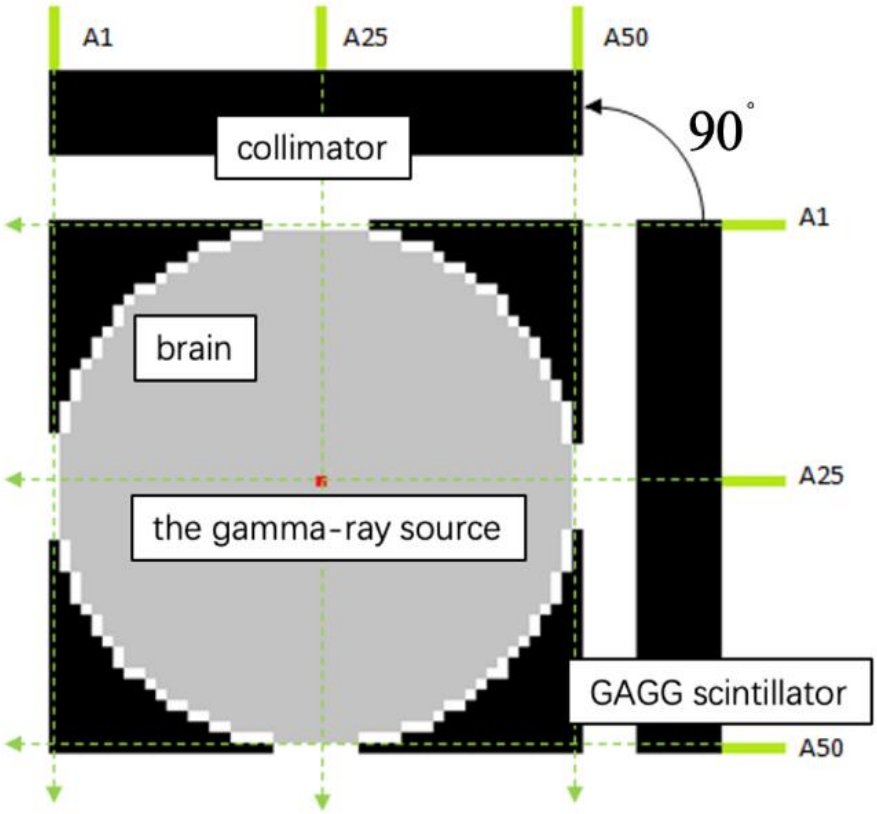

Figure 3.11 A simple schematic view of the detection process for experiments with moving angle θ=90 degrees and n=50.

During treatment, the patient is positioned in close contact with the neutron exit wall, making it impractical to acquire projections from a full 360 degrees. Instead, the projection angle is typically limited to less than 180 degrees. Furthermore, the detector's movement is constrained to a 90-degree range due to the physical setup, with the detector angle fixed less than 90 degrees.

Using the Bayesian estimation method, projections are taken m times at every degree increment defined as $\Delta\theta$ around the patient's head. For instance, as shown in Figure 3.11, with $n = 50$, the head is divided into 2500 pixels. This means that each detector row, comprising 50 detectors, captures 50 measurements at evenly distributed angles. By detecting the emitted gamma rays in this manner, we can reconstruct $n \times n$ pixel data from $m \times n$ projection data using the Bayesian estimation method.

This process involves the calculation of a response function **R**, which defines the

relationship between the detected projection data and the reconstructed image data, as discussed in Chapter 2. This method provides a practical and efficient approach to image reconstruction under the constrained conditions of BNCT treatment.

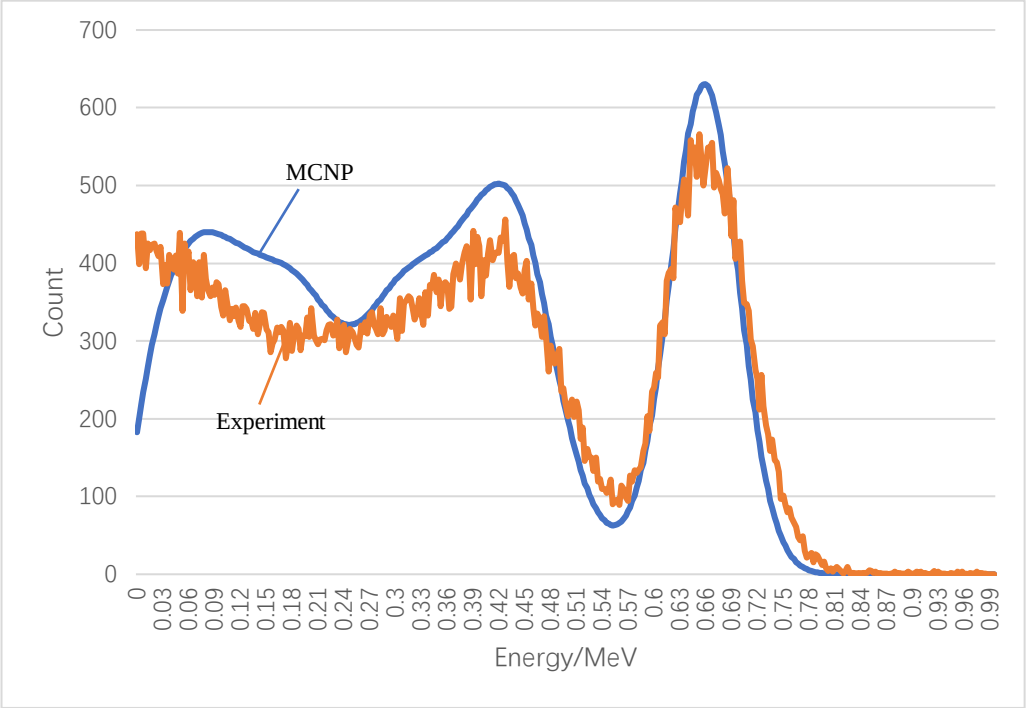

Figure 3.12 Comparison between experimental result and MCNP result

We designed and constructed an experimental system and conducted experiments to evaluate its performance. MCNP5 simulations were performed to generate limited-view-angle projection data and compute the response function, enabling successful image reconstruction. The experimental system was developed to explore experimental specifications for a real BNCT-SPECT system and to validate the measurement system's response function, as evaluated by MCNP5.

The gamma-ray spectra obtained from our experiment and MCNP simulation are shown in Figure 3.12. The response of ^{137}Cs was successfully reproduced using the MCNP code by placing the ^{137}Cs source at the center of the phantom and detecting gamma rays for 2 hours. This confirmed that MCNP can effectively be used in this study to evaluate the system's response functions.

It became evident that directly simulating the real BNCT-SPECT system using the

experimental system poses significant challenges. One major limitation is the absence of background noise in the experimental system, which fails to replicate the complexities of real-world conditions. Moreover, the MCNP simulations do not account for background noise, further reducing the accuracy of system replication.

Additionally, the experimental system lacks the source intensity required to match the conditions of an actual BNCT-SPECT system. This limitation significantly impacts its ability to achieve the necessary accuracy. To address these issues, we established a mock-up system with statistical accuracy and a signal-to-noise ratio comparable to real BNCT-SPECT systems. For this purpose, a ^{137}Cs and a ^{60}Co source were employed to simulate the gamma rays produced during real treatment, providing more representative conditions for testing and validating the system's response. The details of this improved experimental mock-up system will be discussed in Chapter 5.

3.7 Summary

Chapter 3 provides a comprehensive description of the experimental system designed for this study. It begins with an Introduction that outlines the purpose and scope of the experimental system, emphasizing its role in testing and validating the performance of key components for BNCT-SPECT.

The Configuration of the Experimental System describes the overall structure and integration of the system, focusing on the interconnection of various components to achieve accurate gamma-ray detection.

The chapter then delves into the GAGG Scintillator, a core component of the detection system. It first introduces inorganic scintillators and highlights their fundamental properties, such as density, energy resolution, and luminescence efficiency. Section 3.3.3 explains the rationale for selecting GAGG(Ce) scintillators, comparing their performance with other options like NaI(Tl) and CsI(Tl). The chapter further evaluates the detection efficiency and energy resolution of the GAGG(Ce) scintillator, providing experimental results and discussions on its suitability for BNCT-SPECT.

The MPPC component is then detailed, starting with an explanation of its operating principle based on avalanche photodiode technology and Geiger mode. Section 3.4.2

highlights MPPC properties, such as high gain, fast response, and low susceptibility to magnetic fields.

The MCA describes the multichannel analyzer's role in processing and analyzing the signals generated by the MPPC, with details on its digital architecture and spectral processing capabilities.

The Design of the Phantom outlines the human head phantom used to simulate gamma-ray emissions, including its material composition, dimensions, and adaptability for positioning the source.

Finally, the Experimental Procedure provides a step-by-step explanation of how the experiments were conducted, detailing the methodologies used for data collection and analysis. This section integrates all components into a cohesive experimental workflow, ensuring accurate and reproducible results.

This chapter lays the foundation for evaluating the performance of the BNCT-SPECT system and guides the development of improved detection methodologies in subsequent chapters.

References

[1] Glenn F. Knoll 著,神野郁夫,木村逸郎,阪井英次 共訳,"放射線計測ハンドブック 第4版" 日刊工業新聞社(2013)

[2] 古河機械金属株式会社 その他事業 放射線測定器ガンマスポッター シンチレータ結晶物性比較表

[3] 浜松ホトニクス,"光半導体素子ハンドブック第03章 Si APD,MPPC"(2015)

[4] I. Murata et al.," Design of SPECT for BNCT to measure local boron dose with GAGG scintillator", Applied Radiation and Isotopes, 181, 110056 (2022).

https://www.cancer.gov/about-cancer/treatment/types

[5] Sawant, Amit R.. "Portal Imaging Using a CSI (TL) Scintillator Coupled to a Cooled CCD Camera." (1999).

[6] "MPPC arrays in a chip size package miniaturized through the adoption of TSV structure", Hamamatsu, https://www.hamamatsu.com/content/dam/hamamatsu-photonics/sites/documents/99_SALES_LIBRARY/ssd/s13361-3050_series_kapd1054e.pdf

[7] 浜松ホトニクス,光半導体素子ハンドブック 第 03 章 Si APD,MPPC"(2015)

[8] 斉藤博,今井和明,大石正和,澤田孝幸,鈴木和彦 共著,"入門 固体物性 基礎からデバイスまで",共立出版株式会社(1997)

[9] "MCA8000D use manul", AMTEK materials analysis division,

https://www.amptek.com/-/media/ametekamptek/documents/resources/products/user-manuals/mca8000d-user-manual-b1.pdf?la=en&revision=75b93881-a2e4-4d92-9d84-0d67b5d34614

Chapter 4 MCNP5

4.1 MCNP

As mentioned in Section 3.6, MCNP stands for A General Monte Carlo N-Particle Transport Code [1]. It is a radiation transport simulation code widely used for calculating particle transport and interactions in various environments.

MCNP was developed in the mid-1970s by the Los Alamos National Laboratory in the United States. Initially, it was designed to simulate the transport of neutrons and photons. Starting with the fourth version, MCNP4, it was expanded to include electron transport calculations. Currently, the code has been updated to version MCNP6. For the simulations in this study, version 5, MCNP5, was used.

MCNP is widely utilized across various fields for design and safety evaluations, such as for nuclear reactors, accelerators, and satellites. The code supports a broad energy range for calculations: neutrons from 10^{-5} eV to 20 MeV (up to 150 MeV for certain isotopes), photons from 1 keV to 100 GeV, and electrons from 1 keV to 1 GeV. These simulations rely on evaluated nuclear data libraries such as JENDL and ENDF for transport calculations.

4.2 Monte-Carlo method

The transport calculations in MCNP are performed using the Monte Carlo method, a numerical simulation technique that tracks individual particle interactions to statistically solve complex transport problems. The Monte Carlo method, invented by mathematicians J. von Neumann and S. Ulam, was first formally introduced in 1949 in a paper titled "The Monte Carlo Method" by N. Metropolis and S. Ulam [2][3]. Initially developed to study neutron diffusion in atomic nuclei, the method has since found applications in diverse fields such as transportation, financial engineering, and physics.

In essence, the Monte Carlo method involves performing numerous repetitions of an experiment or simulation using random numbers within a computer. Random numbers are employed because many real-world phenomena—such as radiation from radioactive isotopes, traffic congestion on national highways, or fluctuations in

property prices—are inherently random. By utilizing random sampling, the Monte Carlo method can generate solutions that closely approximate real-world behaviors, making it a powerful tool for solving complex problems.

The primary advantage of the Monte Carlo method lies in the simplicity of its calculation algorithm. In traditional methods, if the desired outcome depends on a function of several random variables (e.g., radiation energy or direction), a specific program must be written for each stochastic event (e.g., elastic or inelastic scattering).

In contrast, the Monte Carlo method simplifies this process by using random sampling based on a probability distribution defined by the random variables. Radiation events, characterized by parameters such as energy and position, are repeatedly simulated according to a physical model (e.g., the experimental system). The average result from these simulations provides an approximate solution.

This approach eliminates the need to solve complex equations like the Boltzmann transport equation directly. Instead, the Monte Carlo method offers a computationally efficient way to obtain approximate solutions that closely represent real-world phenomena.

The Monte Carlo method is used for replicating statistical processes, such as the interactions of nuclear particles with materials, and is particularly effective for solving complex problems that are beyond the scope of deterministic computational methods. This approach involves sequentially simulating the individual probabilistic events that make up a process. By statistically sampling from the probability distributions that govern these events, the method provides a comprehensive representation of the overall phenomenon.

Due to the large number of trials required to accurately model these processes, simulations are typically conducted on digital computers. The statistical sampling relies on the use of random numbers, akin to rolling dice in a casino, which is why the technique is named "Monte Carlo."

In particle transport, the Monte Carlo method offers a highly realistic numerical experiment. It involves tracking numerous particles individually, from their initial emission to their eventual termination in outcomes such as absorption or escape. At

each step, transport data is used to randomly sample probability distributions, determining the particle's behavior and trajectory. This step-by-step simulation ensures a detailed and accurate depiction of particle interactions.

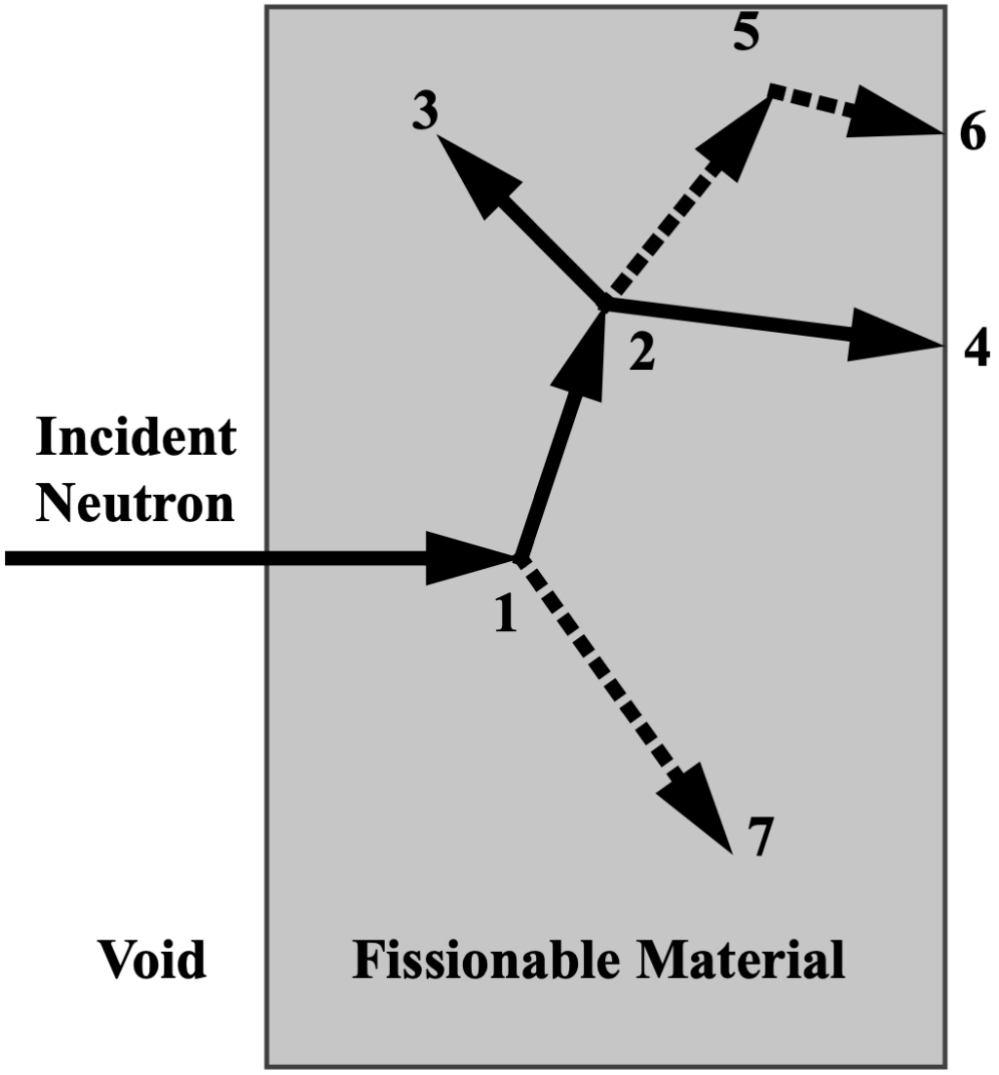

Figure 4.1 Various particles random walks

Figure 4.1 illustrates the random trajectory of a neutron interacting with a slab of material capable of undergoing fission. Random numbers between 0 and 1 are generated to determine the type and location of interactions based on the governing physics and probabilistic transport data for the materials involved. [4]

In this example, the neutron undergoes a collision at event 1, where it is scattered in a randomly selected direction, derived from the physical scattering distribution. A photon

is also produced during this interaction and is temporarily stored, or banked, for later analysis. At event 2, a fission reaction occurs, resulting in the termination of the initial neutron and the creation of two new neutrons and one photon. One of these neutrons and the photon are banked for subsequent analysis.

The first fission neutron is captured and terminated at event 3. The banked neutron is then retrieved and, through random sampling, is shown to leak out of the slab at event 4. The photon produced during the fission event collides at event 5 and subsequently escapes the slab at event 6. Finally, the photon generated at event 1 is tracked and captured at event 7.

It is important to note that MCNP retrieves banked particles using a last-in, first-out (LIFO) method, meaning the most recently stored particle is the first to be processed. This example demonstrates the sequential random sampling process that underpins the Monte Carlo method in particle transport simulations.

This neutron history is now complete. As more individual histories are simulated, the distributions of neutrons and photons become increasingly well-defined. The quantities of interest, as specified by the user, are systematically tallied during the simulation. Additionally, the statistical precision (uncertainty) of the results is calculated, providing an estimate of the reliability of the computed data.

4.3 Tallies

We can configure MCNP to perform diverse tallies, such as those for particle currents, flux distributions, and energy deposition. In most scenarios, these tallies are normalized per initial particle, with exceptions primarily in cases involving criticality sources. Particle currents can be recorded based on directionality and calculated for any combination of surfaces, surface segments, or an aggregate of surfaces within the simulation. Additionally, the code supports tallying charges specifically for electrons and positrons. It also supports flux tallies across various configurations, including specific surfaces, surface segments, aggregated surfaces, cells, cell segments, or combinations of cells. Standard tallies include flux measurements at designated detector points or rings, as well as radiography detectors. Additionally, fluxes can be

recorded on a mesh grid overlaid on the problem's geometry. Energy deposition can be assessed using heating and fission tallies, which provide energy values for specified cells. A pulse height tally records the energy distribution of pulses generated in a detector by radiation. Particles can also be flagged upon crossing specified surfaces or entering designated cells, and their contributions to the tallies are reported separately.

MCNP enables the calculation of a wide range of parameters, such as the number of fissions, absorption events, total helium production, or any product of the flux and approximately 100 standard ENDF reaction types, along with several nonstandard reactions, using its tally system. In essence, any quantity expressed in the form $C = \int \phi(E) f(E)\, dE$ can be calculated using MCNP's tally capabilities. Here, $\phi(E)$ represents the energy-dependent fluence, while $f(E)$ can be any product or summation of values derived from the cross-section libraries or a specified response function. Tallies in MCNP can account for line-of-sight attenuation, allowing for more precise simulation results. It is possible to calculate tallies for specific segments of cells or surfaces without incorporating these segments directly into the problem geometry. All tallies are user-defined as functions of time and energy and are normalized per initial particle. Similarly, mesh tallies are energy-dependent and are also normalized on a per-particle basis, ensuring consistency across simulations.

Table 4.1 Tally mnemonic

Tally Mnemonic					**Description**
F1:N	or	F1:P	or	F1:E	Surface current
F2:N	or	F2:P	or	F2:E	Surface flux
F4:N	or	F4:P	or	F4:E	Track length estimate of cell flux
F5a:N	or	F5a:P			Flux at a point or ring detector
F6:N	or	F6:P	or	F6:N,P	Track length estimate of energy deposition
F7:N					Track length estimate of fission energy deposition
F8:N	or	F8:P	or	F8:E	Pulse height tally
			or	F8:P,E	

Table 4.2 Tally quantities scored

Tally	Score	Physical Quantity	Units
F1	W	$J = \int dE \int dt \int dA \int d\Omega \ \lvert\hat{\Omega} \cdot \hat{n}\rvert \ \psi(\vec{r}, \hat{\Omega}, E, t)$	particles
F2	$\frac{W}{\lvert\mu\rvert A}$	$\bar{\phi}_S = \frac{1}{A}\int dE \int dt \int dA \int d\Omega \ \psi(\vec{r}, \hat{\Omega}, E, t)$	particles/cm^2
F4	$W\frac{T_l}{V}$	$\bar{\phi}_V = \frac{1}{V}\int dE \int dt \int dV \int d\Omega \ \psi(\vec{r}, \Omega, E, t)$	particles/cm^2
F5	$\frac{W \cdot p(\Omega_P)e^{-\lambda}}{R^2}$	$\phi_P = \int dE \int dt \int d\Omega \ \psi(\vec{r}_P, \hat{\Omega}, E, t)$	particles/cm^2
F6	$W T_l \sigma_t(E) H(E) \frac{\rho_a}{m}$	$H_t = \frac{\rho_a}{m}\int dE \int dt \int dV \int d\Omega \ \sigma_t(E) H(E) \psi(\vec{r}, \hat{\Omega}, E, t)$	MeV/g
F7	$W T_l \sigma_f(E) Q \frac{\rho_a}{m}$	$H_f = \frac{\rho_a}{m} Q \int dE \int dt \int dV \int d\Omega \ \sigma_f(E) \psi(\vec{r}, \hat{\Omega}, E, t$	MeV/g
F8	W_C put in bin E_D	pulses	pulses

MCNP offers seven standard tally types shown in Table 4.1, encompassing seven neutron tallies, six photon tallies, and four electron tallies. These standard tallies serve as the foundation for simulation data collection and can be customized extensively by the user to suit specific requirements.

All tally results are normalized on a per-starting-particle basis, with the exception of KCODE criticality calculations, where tallies are normalized per fission neutron generation. To facilitate the interpretation of results, MCNP includes a tally plotter feature, which provides graphical visualizations of the tally outputs, making it easier to analyze and present the data. In this study, we utilized the F8 tally, which is used for energy deposition in detectors.

4.4 Variance reduction

The estimated relative error R in MCNP simulations is inversely proportional to $1/\sqrt{N}$, where N represents the number of particle histories. Since the computational time T is directly proportional to N, the relationship $R = C/\sqrt{T}$ holds, where C is a positive constant.

Reducing R can be achieved in two ways: (1) increasing the computational time T or (2) decreasing the constant C. However, practical constraints, such as limited

computational resources, often restrict the first option. For instance, achieving R=0.10 might take 2 hours, but reducing R to 0.01 would require 200 hours—a prohibitive increase.

To address this, MCNP provides specialized variance reduction techniques to minimize C, which represents the variance divided by the number of samples. The value of C depends on the tally choices and sampling strategy, making variance reduction an essential tool for improving simulation efficiency without excessive computational costs.

4.4.1 Tally choices

An example of how the tally choice impacts results can be seen in estimating the fluence within a cell. This can be achieved using either a collision estimates or a track length estimate.

The collision estimate involves tallying $1/\sum_t$ (where $\sum_t$ is the macroscopic total cross-section) at each collision within the cell. Conversely, the track length estimate calculates the fluence by tallying the distance a particle travels inside the cell. When $\sum_t$ is very small, collisions become infrequent, but each collision contributes disproportionately large tallies, leading to high variance in the results. In contrast, the track length estimate contributes a tally for every particle that passes through the cell, regardless of whether a collision occurs. This difference significantly reduces variance in most scenarios.

For this reason, MCNP includes track length tallies as a standard option, while collision tallies are generally not standard, except when used for specific calculations like estimating k_{eff}. This preference reflects the efficiency and reliability of track length tallies in minimizing variance.

4.4.2 Variance reduction tools in MCNP

Variance reduction techniques in MCNP can be categorized into four distinct classes, ranging from straightforward methods to more advanced and complex approaches. These techniques are designed to enhance simulation efficiency by reducing statistical

variance without requiring an impractical increase in computation time.

1. Truncation Methods are the most straightforward variance reduction techniques. These methods accelerate calculations by excluding portions of the phase space that have minimal impact on the solution. A common example is geometry truncation, where irrelevant sections of the geometry are omitted from the model.

In MCNP, specific truncation methods include:

- Energy cutoff: Eliminates particles with energies below a specified threshold, as their contribution to the tally is negligible.
- Time cutoff: Stops tracking particles after a certain time, focusing only on interactions within the timeframe of interest.

These truncation methods reduce the computational load by streamlining the simulation to focus on the most significant aspects of the problem.

2. Population Control Methods are variance reduction techniques that use particle splitting and Russian roulette to regulate the number of samples tracked in different regions of phase space. These methods aim to concentrate computational effort on regions of greater importance while reducing it in less significant areas.

In important regions, particles are split into multiple lower-weight samples to increase statistical sampling. Conversely, in less important regions, fewer particles are tracked, but they are assigned higher weights. This approach ensures the solution remains unbiased through proper weight adjustments.

Specific Population Control Methods in MCNP include:

- Geometry splitting and Russian roulette: Particles entering critical regions are split into several tracks, while those in less critical regions may be eliminated probabilistically.
- Energy splitting/roulette: Particles are split or eliminated based on their energy levels to emphasize specific energy ranges.
- Time splitting/roulette: Particles are split or terminated based on their time of existence, focusing on relevant timeframes.

- Weight cutoff: Particles with weights below a threshold are eliminated.
- Weight windows: A range of acceptable weights is defined, and particles are adjusted to fit within this range using splitting or roulette.

These methods allow simulations to achieve high efficiency and reduced variance by tailoring sampling efforts to the most impactful regions of the problem.

3. Modified Sampling Methods adjust the statistical sampling process to increase the number of meaningful tallies per particle. In Monte Carlo simulations, particles can be sampled from distributions that differ from their physical probabilities, provided that their weights are appropriately adjusted to maintain the unbiased nature of the solution.

With these methods, particles are preferentially directed toward desired regions of phase space—such as specific directions, time intervals, energy ranges, or collision locations/types—thereby enhancing the efficiency of the simulation. This targeted sampling ensures that the simulation focuses on regions or events of higher significance.

Modified sampling techniques available in MCNP include:

- Exponential transform: Alters the sampling of particle paths to favor specific directions or reduce particle attenuation in exponential decays.
- Implicit absorption: Avoids particle termination after capture by redistributing the particle's weight to other interactions, increasing the tally contribution.
- Forced collisions: Ensures that a particle interacts within a specified region, even if the natural probability of collision is low.
- Source variable biasing: Adjusts the initial sampling of source particles to favor certain energies, directions, or positions.
- Neutron-induced photon production biasing: Enhances the sampling of photon production events caused by neutron interactions.

These methods allow the simulation to gather more statistically relevant data from fewer particle histories, significantly improving computational efficiency while maintaining accuracy.

4. Partially-Deterministic Methods are the most complex type of variance reduction techniques, as they bypass the standard random walk process by incorporating deterministic-like strategies. These methods leverage approaches such as next-event estimators or control of the random number sequence to improve computational efficiency and accuracy.

In MCNP, partially-deterministic methods include:

- Point Detectors: Estimate the contribution of radiation to a specific point in space by calculating the direct path from the source to the point without relying solely on random sampling.
- DXTRAN: Creates a deterministic path for particles to travel toward a predefined region while preserving randomness in other aspects of the simulation, allowing for focused analysis of specific areas.
- Correlated Sampling: Uses a controlled random number sequence to analyze variations between different scenarios or parameters efficiently, reducing variance in comparative studies.

These advanced methods are particularly useful for problems requiring precise calculations in specific regions or conditions where traditional random sampling would be inefficient or yield high variance.

Variance reduction techniques, when applied correctly, can significantly enhance the efficiency of calculations, allowing users to achieve accurate results with reduced computational time. However, improper use of these techniques can lead to erroneous results with seemingly good statistical precision, often providing few indications that the results are flawed.

Certain variance reduction methods are broadly applicable and relatively straightforward to implement, minimizing the risk of misuse. Others, however, are highly specialized and carry a greater risk of errors if not applied carefully.

In many cases, variance reduction is not merely a tool to accelerate simulations but an essential requirement to obtain results at all. For instance, simulations involving deep penetration scenarios or pipe detector problems would be computationally prohibitive—running slower by factors of trillions—without the application of effective

variance reduction strategies. [4]

4.5 Simulation results with MCNP

Based on the MCNP description provided above, we utilized MCNP in this study to simulate and replicate the actual BNCT-SPECT process.

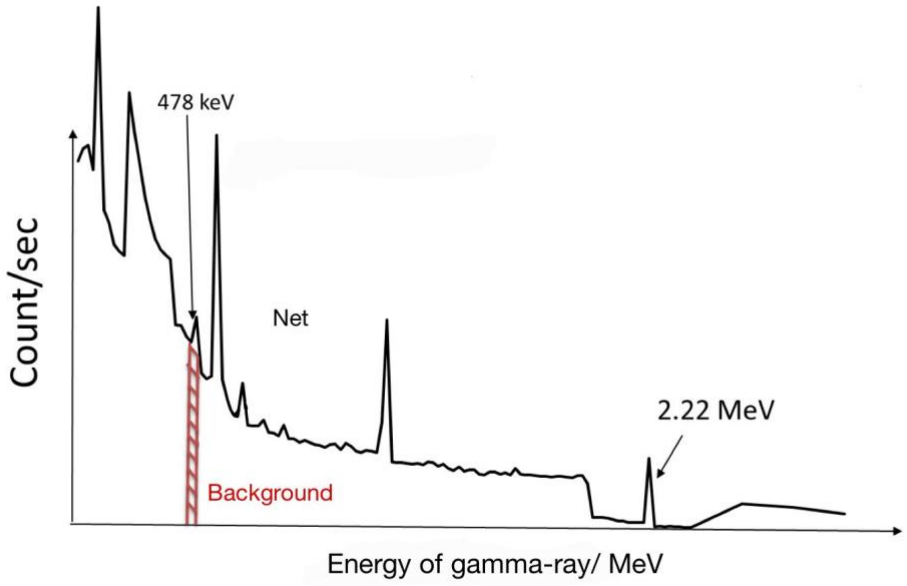

Figure 4.2 Ideal PHS for BNCT-SPECT

Figure 4.2 shows the ideal Pulse Height Spectrum (PHS) for the BNCT-SPECT system. At 478 keV, the red region represents the background (BG), while the remainder of the peak corresponds to the net count. The background originates from gamma rays emitted due to various reactions within the experimental system.

In addition to the immediate 478 keV gamma rays generated from the $^{10}B(n, \alpha)^{7}Li$ reaction, which reflects the therapeutic effect, background gamma rays are produced by other neutron interactions. These include gamma rays from reactions such as $^{1}H(n, \gamma)^{2}H$, $^{155}Gd(n, \gamma)$, $^{157}Gd(n, \gamma)$, and $^{nat}Gd(n, \gamma)$ within GAGG and water. All these gamma rays contribute to the background and are a result of neutron interactions.

In this study, neutrons are not utilized, so alternative methods are required to simulate the background generated by neutron interactions. A ^{137}Cs source is employed to

simulate cancer cells, with the gamma rays produced by ^{137}Cs representing those emitted during actual BNCT treatments. Additionally, a ^{60}Co source is used to generate background gamma rays, replicating the background conditions observed in real BNCT scenarios.

To evaluate the performance of the BNCT-SPECT system, it is crucial to ensure that the statistical accuracy remains below 5%. Statistical accuracy is an indicator of the reliability of the 478 keV gamma rays produced by the ^{10}B(n,α)^{7}Li reaction obtained from calculations. A lower value of statistical accuracy indicates more reliable results. The method for determining this statistical accuracy is described below.

When the counting time is consistent, the net count N_{net} can be expressed using the total count N_{total} and the background count N_{BG}, as shown in Equation (4.1). Additionally, the standard deviation of the net count, σ_{net}, is calculated using Equation (4.2) [7]. These equations form the basis for evaluating the reliability of the measurement results.

$$N_{net} = N_{total} - N_{BG} \tag{4.1}$$

$$\sigma_{net} = \sqrt{\sigma_{total}^2 + \sigma_{BG}^2} = \sqrt{N_{total} + N_{BG}} \tag{4.2}$$

If the total count N_{total} cannot be obtained, Equations (4.1) and (4.2) can be rewritten as Equations (4.3) and (4.4), respectively.

$$N_{net} = (N_{net} + N_{BG}) - N_{BG} \tag{4.3}$$

$$\sigma_{net} = \sqrt{\sigma_{net}^2 + \sigma_{BG}^2 + \sigma_{BG}^2} = \sqrt{N_{net} + 2N_{BG}} \tag{4.4}$$

The statistical accuracy, defined as the ratio of the standard deviation σ_{net} to the net

count N_{net}, is quantified using Equation 4.5. This metric evaluates the relative statistical fluctuations in the net count, providing a quantitative measure of the reliability and precision of the experimental data. Achieving high statistical accuracy is crucial for ensuring precise imaging results, which are essential for the effective performance of the BNCT-SPECT system.

$$\text{Statistical accuracy } [\%] = \frac{\sigma_{net}}{N_{net}} \times 100 = \frac{\sqrt{N_{net} + 2N_{BG}}}{N_{net}} \times 100 \qquad (4.5)$$

To replicate the designed experimental system using the two gamma-ray sources, it is essential to achieve an accuracy of 4.39% and a signal-to-noise ratio (S/N) of 0.21. The S/N is calculated using Equation (4.2), which defines the relationship between the signal and background noise levels in the system. Meeting these criteria ensures the experimental setup closely approximates the conditions and performance of the real BNCT system.

$$\frac{\mathrm{S}}{\mathrm{N}} = \frac{\mathrm{NET}}{\mathrm{BG}} \qquad (4.2)$$

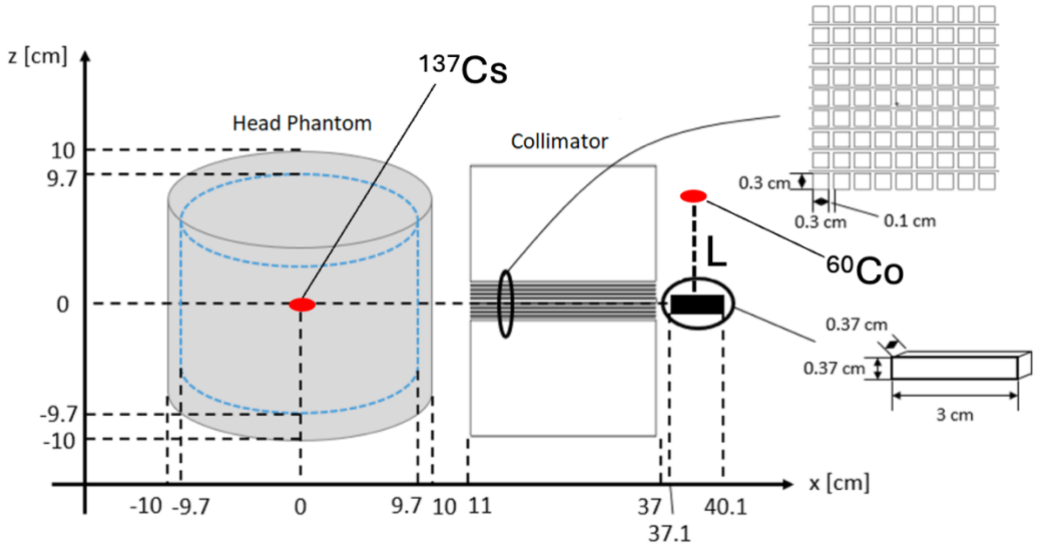

Figure 4.3 Simulation model in MCNP

The placement of the ^{60}Co source significantly impacts the S/N ratio. To analyze this, MCNP simulations were performed based on the model shown in Figure 4.3. In these simulations, the ^{137}Cs source was positioned at the center of the phantom [5], while the ^{60}Co source was placed at varying distances L to the right of the detector. This setup allowed the calculation of different S/N ratios depending on the location of the ^{60}Co source relative to the detector [6].

Figure 4.4 shows the calculated results for different distances: the upper part represents calculations for distances ranging from 2 to 8 cm, while the lower part focuses on distances between 4.1 and 5 cm. Table 4.3 provides detailed calculation data for distances in the range of 4.1 to 5 cm.

The S/N ratio reached 0.20798 when the ^{60}Co source was positioned at a distance of 4.9 cm from the detector. This value is the closest to the target S/N ratio of 0.21, confirming the optimal placement for achieving the desired experimental conditions.

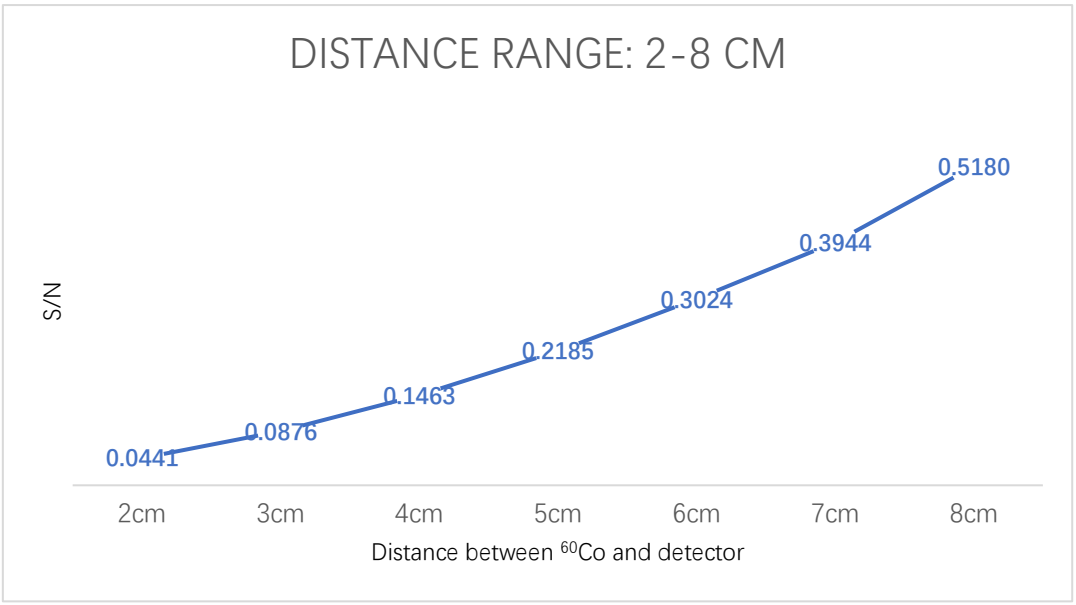

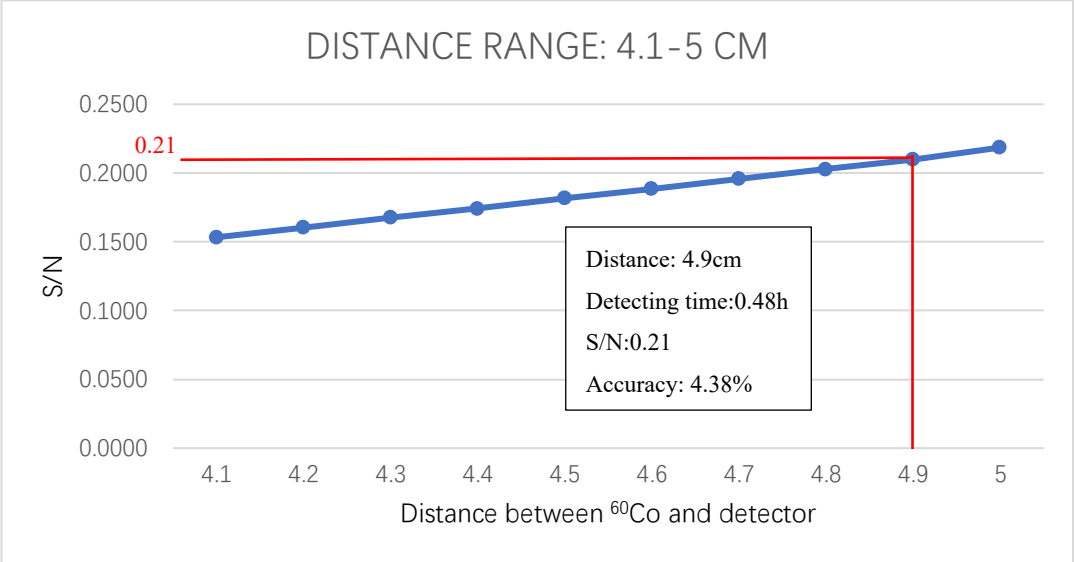

Figure 4.4 Calculation results of S/N.

(Top: Distance range 2-8 cm; Bottom: Distance range 4.1-5 cm)

Table 4.3 Calculation results of S/N for a distance range of 4.1-5 cm

Distance/cm	4.1	4.2	4.3	4.4	4.5	4.6	4.7	4.8	4.9	5.0
S/N ratio	0.1533	0.1604	0.1677	0.1744	0.1819	0.1886	0.1959	0.2027	0.2098	0.2185

After establishing the simulation mock-up system, the counts for various detection times were calculated. The optimal accuracy of 4.38% was achieved with a detection time of 0.48 hours. Additionally, the net count for ^{137}Cs was 5474, with a background

count of 26,024, meeting the specified design criteria.

Table 4.4 Simulation result

Accuracy	4.38%
S/N	0.2098
time	0.48h
NET	5474.21
BG	26024.23
Distance	4.9cm

Under the specified calculation conditions, the MCNP simulation results are presented in Figure 4.5. The orange line represents the simulation outcome for the ^{137}Cs source in isolation, while the gray line depicts the standalone simulation result for the ^{60}Co source. The blue line illustrates the combined simulation results for an experimental setup incorporating both ^{137}Cs and ^{60}Co under the previously described experimental conditions. These results provide a comprehensive comparison of the individual and combined behaviors of the sources within the experimental configuration.

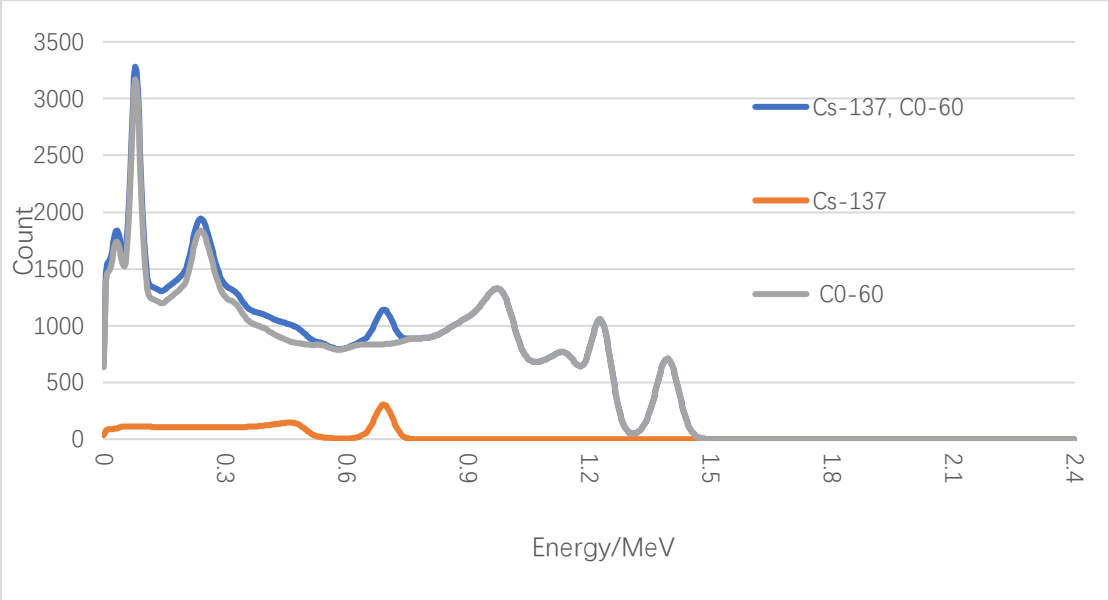

Figure 4.5 Simulation result of mock-up system

This experimental model successfully reproduces the S/N ratio and accuracy required for actual BNCT treatment scenarios. It demonstrates the viability of the system design and validates the methodology for achieving the precision and detection conditions necessary for practical application in BNCT.

Furthermore, the results confirm the feasibility and reliability of MCNP simulations for use in this study, reinforcing its role as a dependable tool for modeling and analysis.

4.6 Summary

Chapter 4 provides a detailed exploration of the use of MCNP5, a powerful Monte Carlo simulation tool, within the context of this study. It begins with an overview of MCNP, outlining its capabilities as a general-purpose Monte Carlo N-Particle transport code for modeling particle interactions and transport in various physical environments. This section introduces its historical development and the range of applications it supports, from nuclear reactor design to medical physics.

Monte Carlo Simulation discusses the underlying principles of the Monte Carlo method, emphasizing its role in solving complex stochastic problems. This section elaborates on how particles are tracked through random sampling based on probability distributions, ensuring realistic and accurate simulations.

The chapter then focuses on Tally, explaining how MCNP tallies are used to collect statistical data about particle interactions. Subsection 4.3.1 introduces tally choices, detailing the various standard tallies available for neutrons, photons, and electrons, as well as the flexibility to customize them for specific applications. Subsection 4.3.2 introduces the variance reduction tools in MCNP, which improve computational efficiency by focusing simulation efforts on important regions and interactions. Methods such as truncation, population control, and modified sampling are discussed, highlighting their practical applications.

Variance Reduction elaborates on techniques designed to reduce statistical uncertainties and enhance simulation performance. Examples include energy and time

cutoffs, track-length tallies, and advanced tools like point detectors and DXTRAN. These methods ensure that simulations are both computationally efficient and accurate.

Finally, Simulation Results with MCNP presents the outcomes of the MCNP simulations conducted in this study. It includes detailed analyses of the signal-to-noise ratio (S/N) and detection precision, showcasing the effectiveness of the mock-up system and its ability to replicate conditions relevant to real BNCT treatment scenarios. The results confirm the feasibility and reliability of MCNP as a tool for modeling and validating experimental designs.

This chapter serves as a comprehensive guide to the application of MCNP5 in this research, demonstrating its critical role in achieving accurate simulations, optimizing experimental designs, and validating theoretical models.

References

[1] ブルックヘブン国立研究所核データセンターのホームページ, http://www.nndc.bnl.gov/exfor/endf00.jsp

[2] X-5 Monte Carlo Team, 2003. MCNP-A General Monte Carlo N-Particle Transport Code, Version 5, LA-UR-03-1987, Los Alamos National Laboratory, Los Alamos, New Mexico.

[3] X-5 Monte C. Team: Briesmeister F.J. (Hrsg.) 2008 General Monte Carlo N-Particle Transport Code, Version 5. (Los Alamos National Laboratory, New Mexico).

[4] 情報システム用語辞典,IT media エンタープライズ

[5] National Institute of Standards and Technology (6 September 2009). "Radionuclide Half-Life Measurements". Retrieved 7 November 2011.

[6] Delacroix, D.; Guerre, J. P.; Leblanc, P.; Hickman, C. (2002). Radionuclide and Radiation Protection Handbook. Nuclear Technology Publishing. ISBN 978-1870965873.

[7] 古河機械金属株式会社 その他事業 放射線測定器ガンマスポッター シンチレータ結晶物性比較表

Chapter 5 Design of mock-up system

5.1 Introduction

The construction of a mock-up system was undertaken to replicate the experimental specifications of the actual BNCT-SPECT system. A ^{137}Cs source was used to simulate the gamma-rays emitted by ^{10}B during actual BNCT treatment, while a ^{60}Co source was utilized to mimic the background radiation present in the designed BNCT system. The following content provides an overview of the developed mock-up system for BNCT-SPECT. This setup served as the foundation for validating the experimental and simulation methodologies developed in this study.

5.2 Design of collimator

5.2.1 Spatial Resolution

Spatial resolution refers to the ability of an imaging system to distinguish between two closely spaced objects or details. In the context of BNCT-SPECT systems, it is a critical parameter that determines the system's capability to accurately reconstruct the distribution of gamma-ray sources within the target area. Higher spatial resolution implies finer detail and more precise localization of the gamma-ray emissions, which is essential for effective imaging and treatment planning. Achieving the required spatial resolution involves optimizing factors such as detector design, pixel size, and system configuration.

The BNCT-SPECT system requires a spatial resolution of 5 mm or less to meet the precision standards necessary for treatment. Figure 5.2 illustrates a scenario where the pitch length of the scintillator exceeds the spatial resolution requirement. In such cases, gaps occur where the scintillators fail to capture any information. Specifically, if the spacing between detectors is greater than the field of view of a single detector, there will be regions within the system that remain undetected, creating blind spots in the imaging process. This highlights the importance of optimizing detector placement and

spacing to ensure comprehensive coverage and accurate data acquisition.

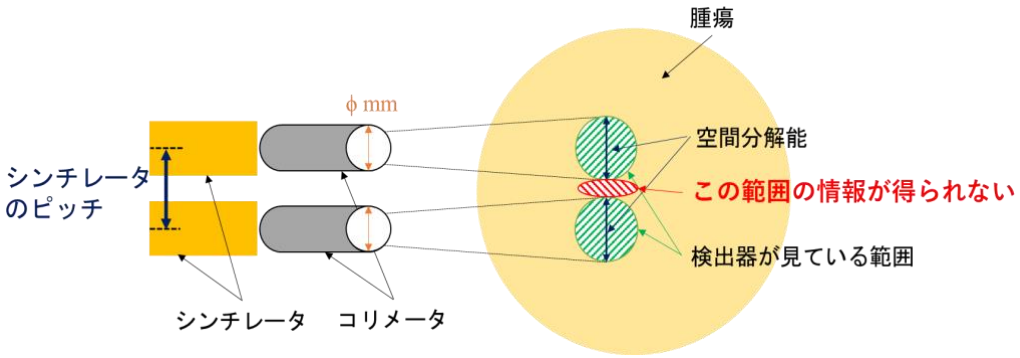

Figure 5.2 Relationship between spatial resolution and scintillator pitch [1]

5.2.2 Construction of collimator

Based on previous research, the collimator length is 26 cm, with a single circular hole of 0.35 cm in diameter. The spatial resolution, as shown in Figure 5.3, is 0.42 cm. In this study, to design and produce a collimator suitable for actual BNCT treatment, we opted for a design featuring 64 square holes. Each square hole is designed to have the same area as the circular hole in previous studies, calculated as $\left(\frac{0.35}{2}\right)^2 \cdot \pi = 0.31\ cm$.

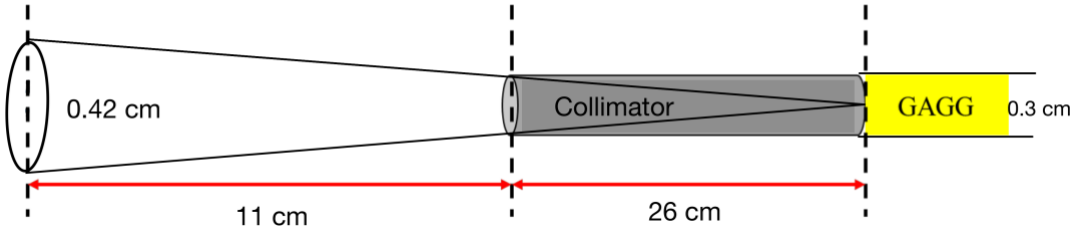

Figure 5.3 System Configuration for Calculating Spatial Resolution

However, during the manufacturing process, achieving an exact precision of 0.31 cm proved highly challenging. To ensure manufacturability while maintaining the required spatial resolution, the collimator holes are square-shaped with a side length of 0.3 cm, and the spacing between adjacent holes is 0.1 cm. This configuration results in a scintillator pitch of 0.4 cm, as illustrated in Figure 5.4. This adjustment ensures both production feasibility and compliance with the spatial resolution requirements.

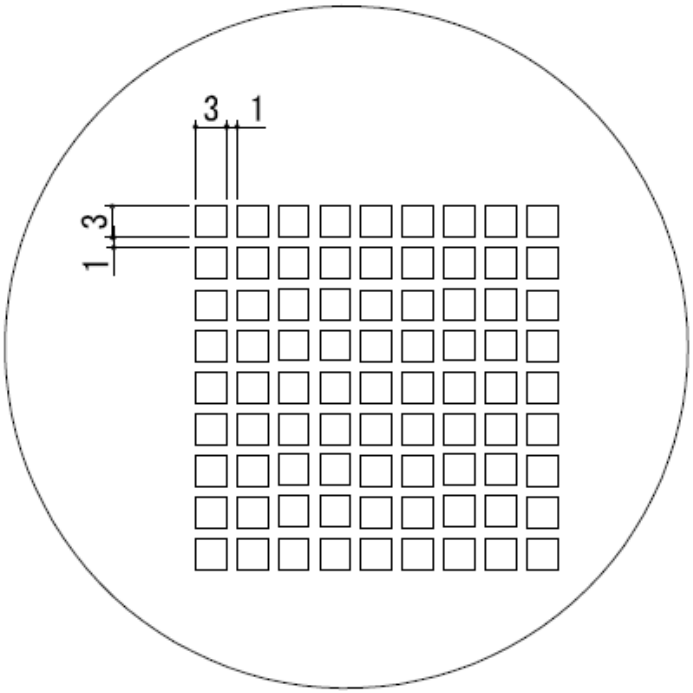

Figure 5.4 Size of holes in the collimator

The production of the collimators, as shown in Figure 5.5, involves a modular design consisting of tungsten plates and tungsten rods. These components are engineered to be stacked on top of each other, allowing for precise assembly and alignment to achieve the desired collimator configuration.

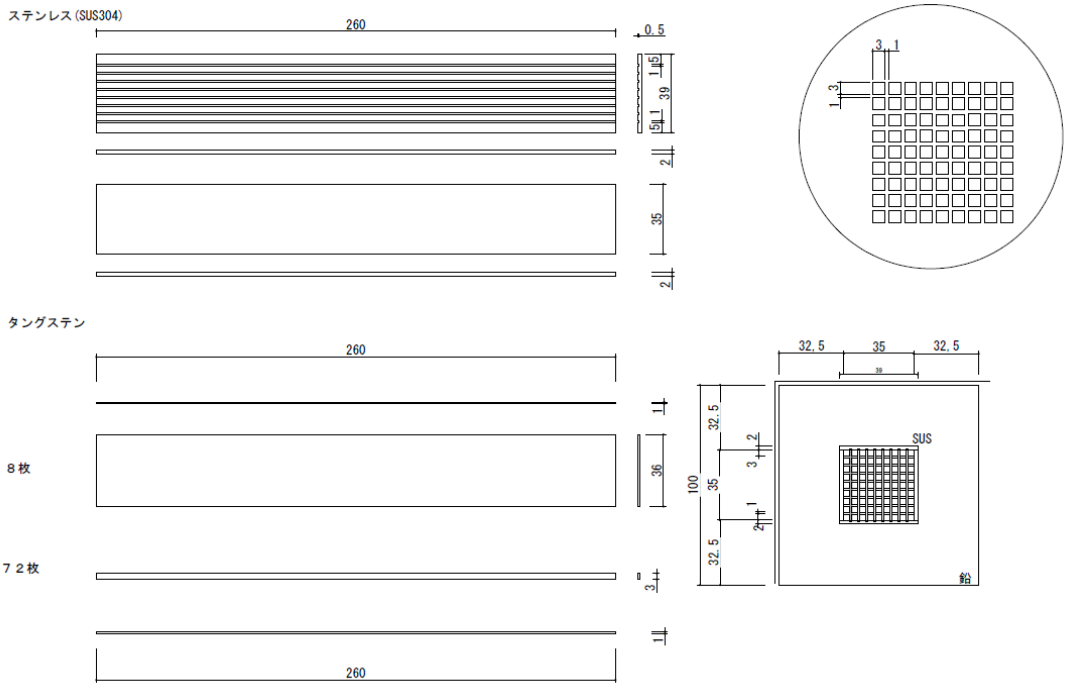

Figure 5.5 Design of collimator

The details of the manufactured collimator are shown in Figure 5.6 below, providing a comprehensive view of its design and construction.

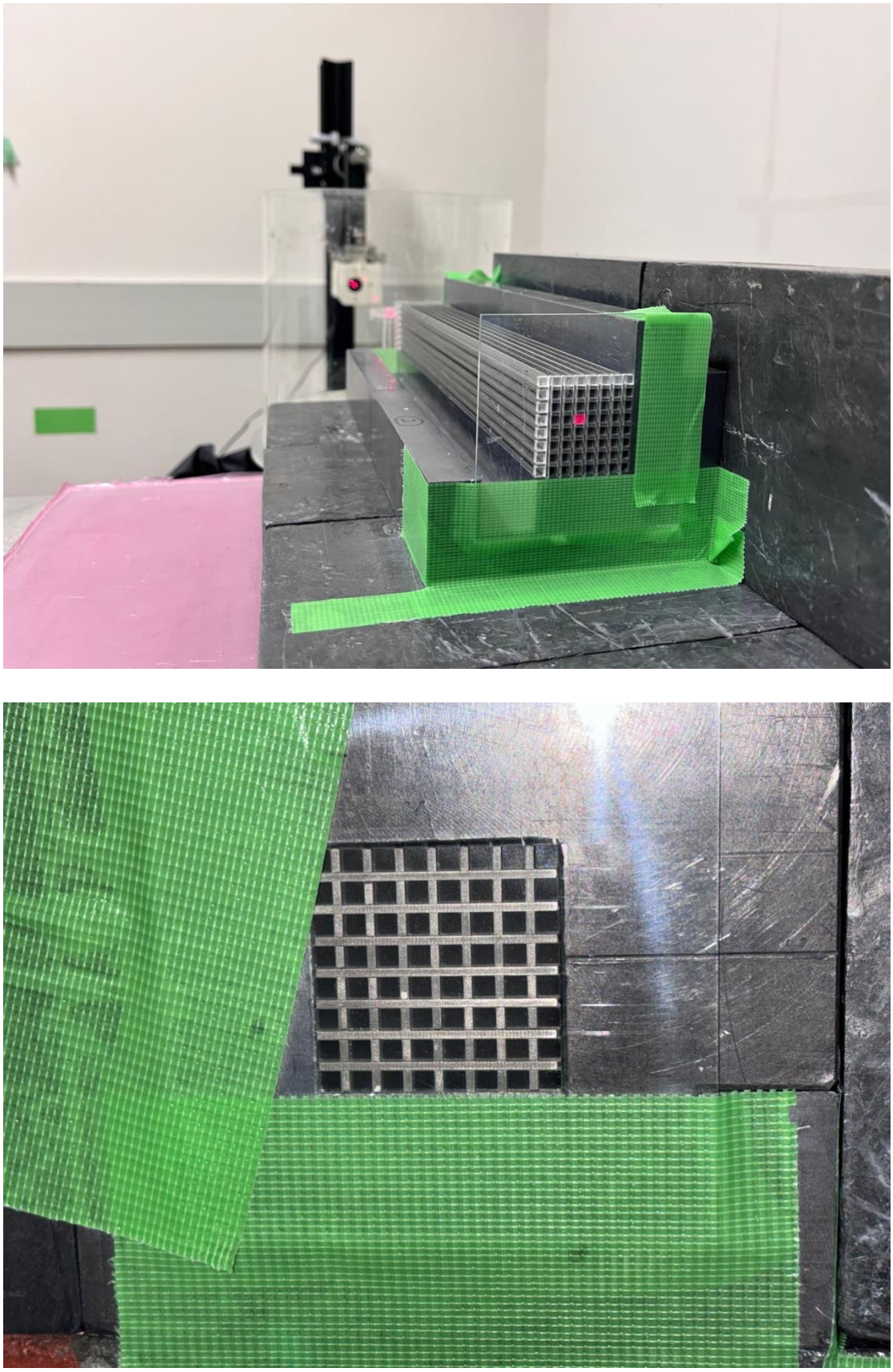

Figure 5.6 Detailed Design of the Manufactured Collimator

5.3 Design of gamma-ray

5.3.1 ^{137}Cs

^{137}Cs is a radioactive isotope of cesium with significant applications in medicine, industry, and scientific research due to its unique properties. It is a fission product of uranium and plutonium, making it one of the prominent radionuclides in nuclear waste and fallout.

1. Physical and Nuclear Properties

   Atomic Number: 55 (Cesium)

   Atomic Mass: 137.91 u

   Decay Mechanism:

   - ^{137}Cs undergoes beta decay (β−) to form a metastable state of barium, ^{137m}Ba (Barium-137m).
   - The transition from ^{137m}Ba to stable ^{137}Ba is accompanied by the emission of a gamma photon with an energy of 662 keV.
   - This two-step decay process accounts for its usefulness as a gamma-ray source.

   Half-Life:

   - ^{137}Cs has a half-life of approximately 30.17 years.
   - ^{137m}Ba, its decay product, has a half-life of about 2.55 minutes, ensuring a consistent gamma-ray emission.

   Radiation Type:

   - Beta Particles (from ^{137}Cs decay).
   - Gamma Rays (from ^{137m}Ba a decay, primarily at 662 keV).

2. Applications of ^{137}Cs

   Medical Applications:

   - Historically used in radiotherapy for cancer treatment, particularly in cesium-based teletherapy units.

- Its gamma-ray emission at 662 keV is ideal for penetrating tissues while maintaining a localized treatment effect.

Industrial Applications:

- Non-destructive Testing (NDT): Used in industrial radiography to inspect welds and materials for structural integrity.
- Moisture and Density Gauges: Widely applied in construction, agriculture, and petroleum industries for density and moisture content measurement.

Scientific and Research Applications:

- Calibration Source: Frequently used for calibrating gamma spectrometers and radiation detection equipment due to its well-defined energy emission.
- Environmental Monitoring:
  - Traces of ^{137}Cs in the environment are used as markers to study soil erosion, sedimentation, and the effects of nuclear fallout.
  - It is one of the key radionuclides monitored after nuclear accidents, such as Chernobyl and Fukushima.
- Educational Use: Demonstrates principles of radioactive decay and gamma-ray detection in laboratories.

Environmental Significance:

- ^{137}Cs is a major component of nuclear fallout due to its high fission yield.
- Its long half-life and mobility in the environment make it a critical isotope for assessing long-term radiological contamination.

3. Safety Considerations

^{137}Cs poses both external and internal radiation hazards:

- External Hazard: Its gamma-ray emission (662 keV) requires adequate shielding, typically with lead or concrete.

- Internal Hazard: If ingested or inhaled, it accumulates in soft tissues, especially muscles, and poses a significant health risk.

Handling ^{137}Cs requires adherence to strict safety protocols:

- Use of protective equipment and remote handling tools.
- Proper containment and shielding during storage and transportation.
- Regulatory compliance for disposal of radioactive waste.

4. Role of ^{137}Cs in This Study

In this study, the primary objective is to investigate image reconstruction techniques and validate the ability of the BNCT-SPECT system to reproduce the desired signal-to-noise ratio (S/N) as defined in the system's design. A key focus is on accurately replicating the net count and background count associated with the 478 keV gamma-rays emitted during the $^{10}B(n,\alpha)^{7}Li$ reaction, as these parameters are critical for effective image reconstruction and system performance evaluation.

However, directly handling the 478 keV gamma rays from the neutron interaction poses significant practical challenges in experimental conditions. Instead, ^{137}Cs is employed as a substitute gamma-ray source, emitting 662 keV gamma-rays. This substitution is justified because the absolute energy resolution for 478 keV is inherently superior to that for 662 keV, making it reasonable to conclude that if the system performs adequately with 662 keV gamma rays, it will also perform well for 478 keV gamma rays.

In this setup, ^{137}Cs is used as the primary source to simulate the net count, representing the gamma-rays of interest in BNCT. To reproduce the background contribution and achieve a realistic S/N ratio, another radioactive source that does not emit interfering gamma-rays at or near 662 keV is selected. This secondary source provides background radiation that complements the ^{137}Cs emissions, ensuring the background levels are accurately modeled according to the design criteria.

By substituting the neutron-induced gamma-rays with those from ^{137}Cs, this study effectively bypasses the complexities of neutron handling while maintaining the integrity of experimental objectives. The use of ^{137}Cs as a controlled and stable gamma-ray source enables precise replication of the S/N ratio and energy resolution required for BNCT-SPECT system validation, highlighting its critical role in ensuring the feasibility and accuracy of this research.

5.3.2 ^{60}Co

^{60}Co is a synthetic radioactive isotope of cobalt widely used in industrial, medical, and scientific applications due to its stable gamma-ray emissions and high-energy radiation. It is produced by neutron activation of ^{59}Co in nuclear reactors and plays a crucial role in radiation-based technologies.

1. Physical and Nuclear Properties

   Atomic Number: 27 (Cobalt)

   Atomic Mass: 59.933 u

   Decay Mechanism:

   - ^{60}Co undergoes beta decay (β−), transforming into stable ^{60}Ni (Nickel-60).
   - This decay process emits two primary gamma rays with energies of 1.173 MeV and 1.332 MeV.

   Half-Life: Approximately 5.27 years, making it a relatively long-lived source suitable for extended use.

   Radiation Type:

   - Beta Particles: Emitted during the decay to ^{60}Ni.
   - Gamma Rays: High-energy photons at 1.173 MeV and 1.332 MeV, which are particularly useful in various applications.

2. Applications of ^{60}Co

   Medical Applications:

   - Radiotherapy: Historically used in external beam radiation therapy (teletherapy) for treating cancer. The high-energy gamma rays from ^{60}Co are effective in delivering precise doses to deep-seated tumors.
   - Sterilization of Medical Equipment: Used to sterilize disposable medical devices such as syringes, surgical instruments, and implants, due to its high penetration and efficiency in destroying microorganisms.

   Industrial Applications:

   - Non-destructive Testing (NDT): Employed in industrial radiography to inspect welds, castings, and structural materials for defects.
   - Irradiation of Materials: Used in food preservation and to prevent spoilage by killing bacteria and insects in agricultural products.
   - Thickness Gauging: Helps measure material thickness in industries such as steel and paper production by monitoring gamma-ray attenuation.

   Scientific and Research Applications:

   - Calibration Source: Serves as a standard gamma-ray source for calibrating detectors and spectrometers due to its well-defined energy emissions.
   - Environmental Tracer: Used in studies to trace the movement of particles or materials in ecosystems or industrial processes.

   Environmental and Safety Monitoring:

   - Frequently employed in studies assessing radiation exposure risks, including those associated with nuclear facilities or accidents.

3. Safety Considerations

   ^{60}Co poses both external and internal radiation hazards due to its high-energy gamma rays:

   - External Hazard: Requires significant shielding, typically using lead or concrete, to protect against its penetrating gamma radiation.

- Internal Hazard: If inhaled or ingested, ^{60}Co accumulates in tissues and presents a serious health risk.

Safe handling involves strict adherence to radiation safety protocols, including:

- Proper containment and transport in shielded containers.
- Remote handling tools to minimize direct exposure.
- Monitoring and compliance with disposal regulations for radioactive waste.

4. Role of ^{60}Co in This Study

In this study, ^{60}Co serves a critical role in simulating the background radiation required to evaluate the signal-to-noise ratio (S/N) and validate the performance of the BNCT-SPECT system. For this purpose, it was essential to select a radioactive source that meets specific criteria: it must produce gamma rays that do not interfere with the emissions from ^{137}Cs, and it must contribute an appropriate level of background radiation to accurately replicate the conditions of a real BNCT treatment environment.

The gamma-ray emissions of ^{60}Co, at energies of 1.173 MeV and 1.332 MeV, are significantly higher than the 662 keV gamma-rays emitted by ^{137}Cs. This clear separation in energy ensures that the background radiation from ^{60}Co does not overlap or interfere with the ^{137}Cs signal, preserving the integrity of the experimental measurements. Additionally, the high-energy photons from ^{60}Co provide a stable and consistent background source that effectively mimics the scattering and noise present in a clinical BNCT scenario.

By incorporating ^{60}Co as the background source, the study achieves a realistic approximation of the radiation environment encountered during BNCT. This enables the experimental system to replicate the design conditions accurately, ensuring the validity of the S/N ratio and energy resolution measurements. Furthermore, the use of ^{60}Co demonstrates its reliability and effectiveness in creating a controlled and realistic testing environment, reinforcing its role as an indispensable component in this research.

5.4 Design results

The development and construction of an advanced mock-up system were undertaken to replicate the experimental specifications of the actual BNCT-SPECT system. In this system, a ^{137}Cs source was utilized to simulate the gamma-rays emitted by ^{10}B during actual BNCT treatment, while a ^{60}Co source was employed to generate the background radiation. This design was informed by the research above and tailored to reproduce the conditions necessary for evaluating the system's performance under realistic treatment scenarios. Figure 5.7 shows the front and top views of the actual developed mock-up system.

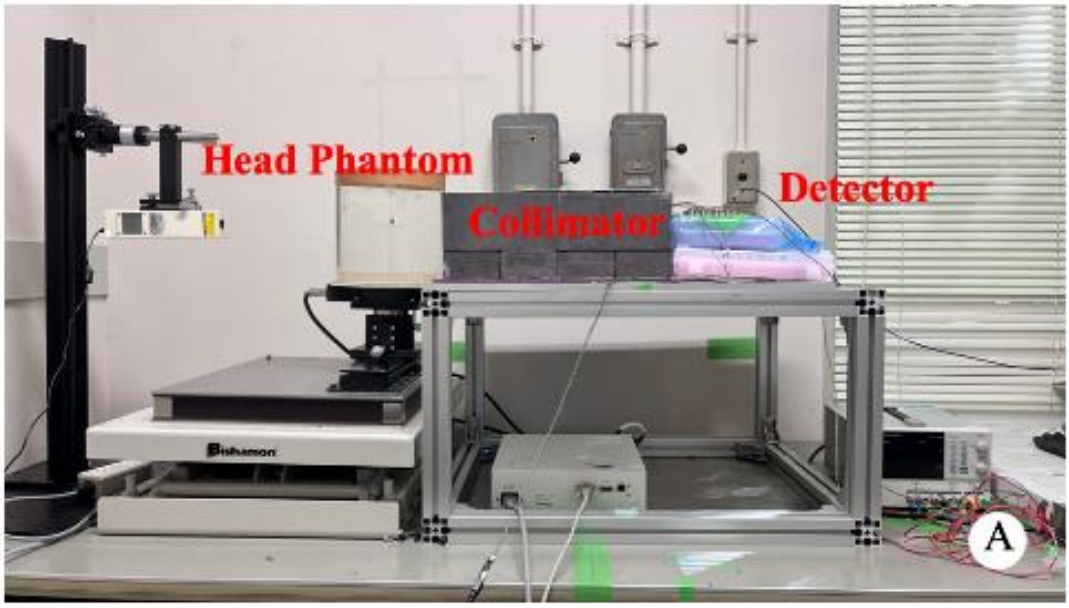

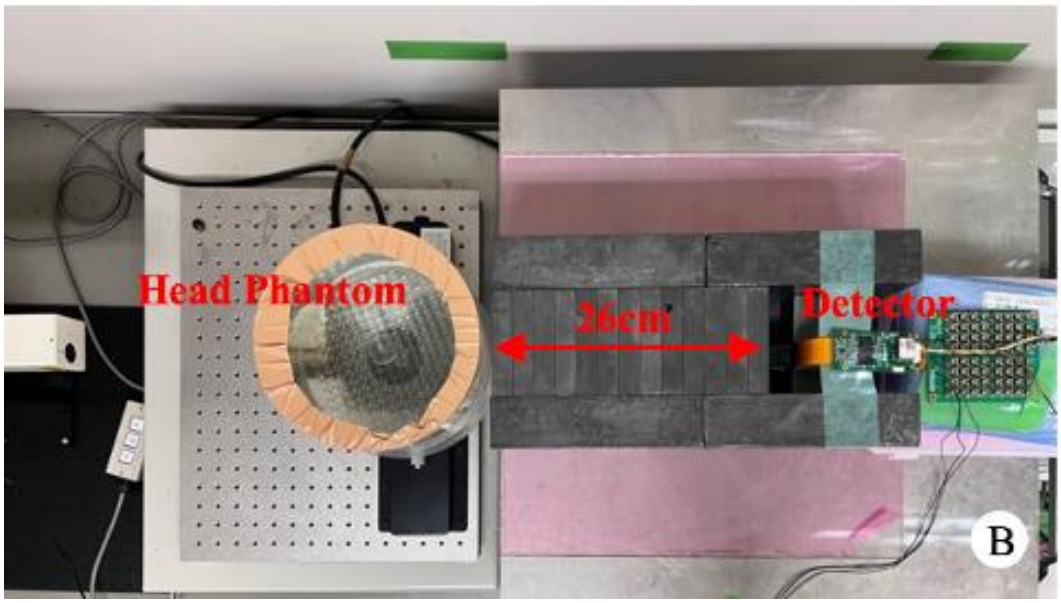

Figure 5.7 Mock-up system: front view (A) and top view (B).

A ^{137}Cs source was positioned at the center of a head phantom composed of acrylic and water [2], while a ^{60}Co source was placed at various distances (d) above the detector to evaluate the statistical accuracy and signal-to-noise (S/N) ratio of the system. Given its critical role in cancer treatment, the BNCT-SPECT system is designed to achieve a spatial resolution of 0.5 cm or finer, ensuring precise imaging capabilities. Based on previous studies, the collimator's optimal length was established at 26 cm [1]. A detailed summary of the specifications for the developed mock-up system, along with a comparison to the designed BNCT-SPECT system, is provided in Table 5.1, offering a clear overview of the system's parameters and performance alignment.

Table 5.1 Specifications of the experimental system compared to the designed BNCT-SPECT system.

Design item		Present mock-up system	Designed BNCT-SPECT
Scintillator	Material	→	GAGG(Ce)
	Dimensions	→	0.35 cm × 0.35 cm × 3 cm [1]
Collimator	Material	Pb	W
	Thickness	→	26cm
	Hole size	0.3 cm × 0.3 cm×64	Ø 0.35 cm×64
Phantom	Material	Acryl and water	-
	Dimensions	Ø20 cm × 20 cm	-
Statistical accuracy		4.39%	4.39%
(S/N)		0.21	0.21 [8]

Subsequently, experiments were conducted using the aforementioned designed system to evaluate its performance under the specified conditions. In parallel, the MCNP simulation code was utilized to construct a virtual system identical to the designed mock-up system, enabling detailed computational analyses and validation of the experimental results.

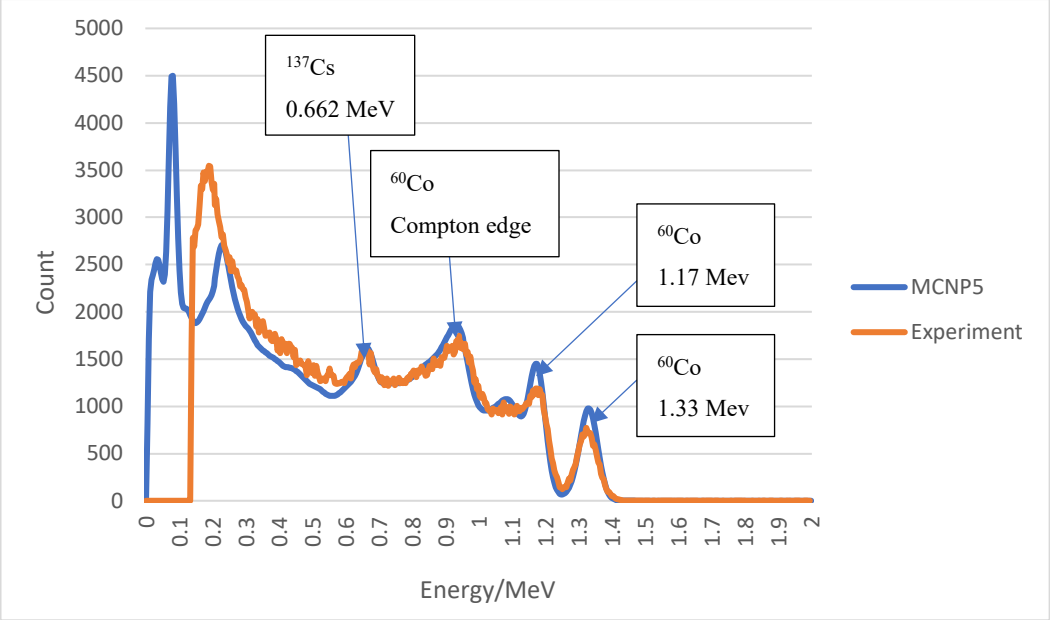

Figure 5.8 Comparison between experimental result and MCNP5 result.

Figure 5.8 presents a comparison of the pulse height spectra obtained from the mock-up experiments and MCNP5 simulations, showing agreement between the two. Clear and distinct peaks corresponding to ^{60}Co and ^{137}Cs gamma-ray emissions are observed, effectively replicating the designed BNCT-SPECT conditions. These peaks serve as the background and signal components necessary for testing the system's performance.

Table 5.2 provides the intensities of the ^{137}Cs and ^{60}Co gamma-ray sources used in the study. As described in Chapter 4, the ^{137}Cs source, with an activity of 1×10^{7} Bq, is placed at the center of the head phantom, while the ^{60}Co source, with an intensity of 1.06×10^{6} Bq, is positioned 4.9 cm above the detector. The intensities of ^{137}Cs and ^{60}Co were chosen based on the most suitable sources available in our laboratory to ensure an optimal balance between experimental conditions and measurement duration. This setup ensures realistic replication of the experimental and simulation conditions for validating the BNCT-SPECT system.

Table 5.2 Simulation condition.

^{137}Cs intensity	1×10^{7} Bq
^{60}Co intensity	1.06×10^{5} Bq

Based on the findings from Chapters 4 and 5, the mock-up system demonstrated remarkable performance, achieving a statistical accuracy of 4.39% within a counting time of just 0.48 hours, which is less than one hour. This result closely aligns with the design specifications of the BNCT-SPECT system. Furthermore, the count rate per hour for ^{137}Cs confirmed that the mock-up system is suitable for practical measurements under experimental conditions.

Notably, the mock-up system achieved a statistical accuracy of 4.4% and an S/N ratio of 0.21, both of which are consistent with the expected performance of the designed BNCT-SPECT system. These results highlight the mock-up system's ability to closely replicate the statistical accuracy and signal quality required for effective BNCT-SPECT imaging, making it a reliable platform for further experimental validation and system development.

5.5 Summary

Chapter 5 provides a detailed account of the design and development of the mock-up system for the BNCT-SPECT experiment, focusing on its key components such as the collimator and gamma-ray sources. The purpose of the mock-up system is to replicate the performance of the designed BNCT-SPECT system, ensuring its suitability for practical applications and experimental validation.

The spatial resolution of the BNCT-SPECT system, critical for accurate imaging, is designed to be 0.5 cm or finer. The chapter discusses the impact of collimator pitch and geometry on achieving the desired resolution, highlighting adjustments made to eliminate undetected regions. Based on prior studies, the optimal collimator length was set to 26 cm. The collimator features square holes with a side length of 0.3 cm, redesigned from a circular hole of equivalent area to ensure manufacturability while maintaining spatial resolution.

For gamma-ray sources, a ^{137}Cs source with an activity of 1×10^{7} Bq was placed at the center of an acrylic and water phantom to simulate the gamma-rays emitted by ^{10}B during BNCT treatment. Its 662 keV gamma-ray emissions closely approximate the

conditions required for evaluating system performance. Additionally, a ^{60}Co source with an intensity of 1.06×10^{6} Bq was positioned 4.9 cm above the detector to simulate background radiation. The high-energy gamma emissions of ^{60}Co (1.173 MeV and 1.332 MeV) ensured non-interference with the ^{137}Cs signal, effectively replicating the S/N ratio observed in real BNCT-SPECT systems.

The mock-up system demonstrated excellent performance, achieving a statistical accuracy of 4.39% within a counting time of 0.48 hours, closely matching the design results of the BNCT-SPECT system. Additionally, the system achieved a favorable S/N ratio of 0.21, confirming its ability to replicate the designed system's specifications. These results underscore the reliability of the mock-up system as a platform for experimental validation and further development, ensuring all components align with the requirements of the BNCT-SPECT system.

References

[1] 南 健太郎: GAGG シンチレータを用いた BNCT 用 SPECT 装置の設計と製作," 修士学位論文, 大阪大学大学院工学研究科 (2019).

[2] Kanno, I., Nishimatsu, D., Funama, F. "Simulation study on the feasibility of current-mode SPECT for B-10 concentration estimation in boron neutron capture therapy." *Journal of Instrumentation* 14.02 (2019): C02002.

Chapter 6 Image reconstruction

6.1 Introduction

In this chapter, we focus on the process of image reconstruction for the BNCT-SPECT system using two distinct methodologies. The first involves employing an idealized response function, constructed mathematically and implemented through Python, to perform image reconstruction under theoretically perfect conditions. The second approach utilizes the experimentally derived response function obtained from the mock-up system designed and constructed in Chapter 5.

By comparing the reconstructed images from these two methods, we aim to evaluate the practicality and accuracy of the experimental system against the theoretically ideal conditions. This comparison highlights the strengths and limitations of the mock-up system, providing insights into the feasibility of achieving accurate image reconstruction in real-world BNCT applications.

The chapter proceeds as follows: Section 6.2 discusses the reconstruction process using a mathematically ideal response function, providing a foundation for understanding theoretical image reconstruction. Section 6.3 details the experiments conducted using the designed mock-up system to collect experimental data, while Section 6.4 focuses on reconstructing images based on the experimentally derived response function. Finally, Section 6.5 summarizes the findings and outlines the implications of these results for the development of BNCT-SPECT systems.

6.2 Reconstruction with the mathematically ideal process

Based on the content introduced in Chapter 2, pseudo-projection data was generated to evaluate the performance of the image reconstruction methods. A true image of size 50×50 pixels was used, with 50 detectors per projection angle. This setup allowed for the acquisition of projection data across multiple angles, resulting in a comprehensive sinogram comprising $50 \times m$ $(m = 90/\Delta\theta)$ data points.

Figure 3.1 illustrates the portion of the detector system used for image reconstruction in a single cross-section. In this setup, multiple detectors arranged in a straight line

simultaneously measure gamma-rays to determine the intensity of radiation emitted by the source inside the head phantom at the respective positions of each detector. In the actual measurement system, detector arrays, such as those shown in Figure 3.1, are vertically stacked at different heights. These stacked arrays collect data that is subsequently used to reconstruct cross-sectional images for each height.

The majority of the radiation detected by each detector originates from the source directly in front of the collimator hole. As a result, radiation from sources positioned above or below a given detector row has minimal impact on the reconstruction results. However, the effects of cross-talk, a phenomenon in which radiation entering one detector undergoes Compton scattering and is subsequently detected by adjacent detectors, must be considered. This is particularly important when multiple scintillator detectors are placed in close proximity.

When cross-talk occurs, a single incident radiation event may result in detections by multiple detectors, causing the total detection count to exceed the expected number based on the calculated detection efficiency. According to prior research conducted in the author's laboratory, this issue can be mitigated by considering coincident counting of radiation detected simultaneously by neighboring detectors. This approach not only resolves the cross-talk problem but also improves the statistical accuracy of the measurements.

In BNCT-SPECT, cross-sectional images are reconstructed for each height, and the resulting slices are stacked to estimate the three-dimensional distribution of the radiation source. This method enables accurate reconstruction of the spatial distribution of gamma-ray sources, critical for BNCT applications.

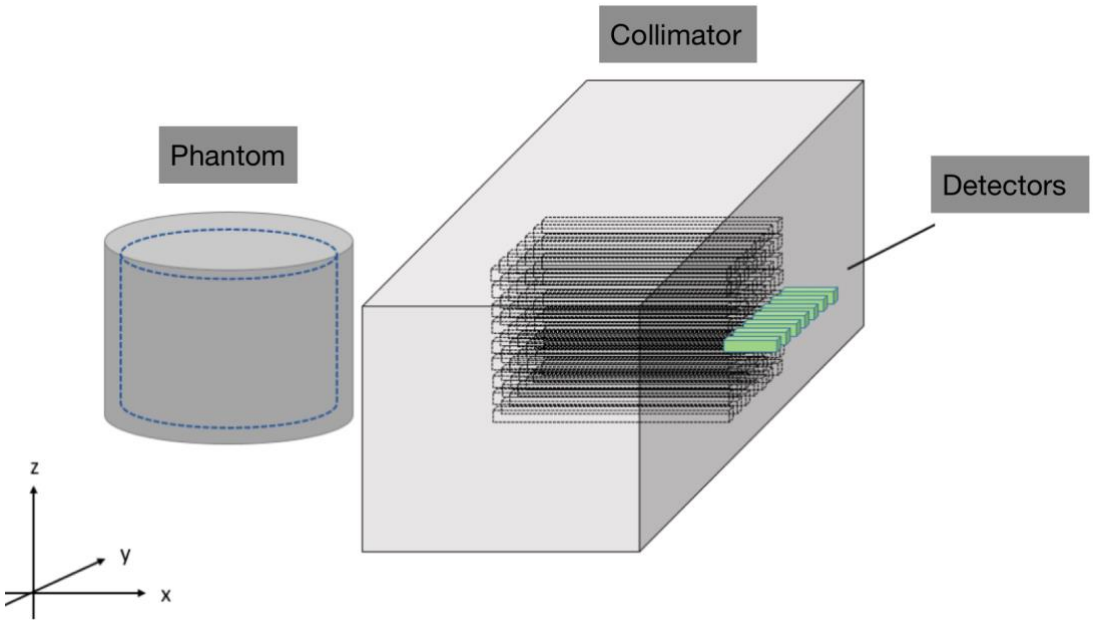

Figure 6.1 Overall Diagram of the Detector System Assumed in the Image Reconstruction Program

The sinogram was subsequently utilized to reconstruct the image using the proposed method. Each reconstruction was iteratively refined over 100 iterations to ensure convergence and accuracy. Following the reconstruction process, a Gaussian filter [1] was applied to the images to enhance quality by smoothing out noise and improving visual clarity.

The performance of the reconstructed images was quantitatively assessed using two evaluation metrics: Mean Absolute Error (MAE) and Structural Similarity Index (SSIM). MAE measured the pixel-wise difference between the true and reconstructed images, while SSIM provided an assessment of structural and perceptual fidelity. This analysis enabled a comparative evaluation of the proposed method against ML-EM, demonstrating the effectiveness of the techniques in achieving high-quality image reconstruction.

6.2.1 Reconstruction at $\Delta\theta = 30°$ with a single model

According to the calculations by our research group in 2021, the optimal choice is to irradiate four times with $\theta = 90°$ and $\Delta\theta = 30°$. This conclusion is based on a

comprehensive evaluation of the SSIM and MAE results, which demonstrate that this configuration yields the best performance. [2] The mean MAE values, calculated from the estimated results over 50 iterations for each Δθ, are presented in Figure 3. Similarly, the mean SSIM values obtained under the same conditions are displayed in Figure 4. These results provide a comprehensive evaluation of the reconstruction performance for different Δθ settings.

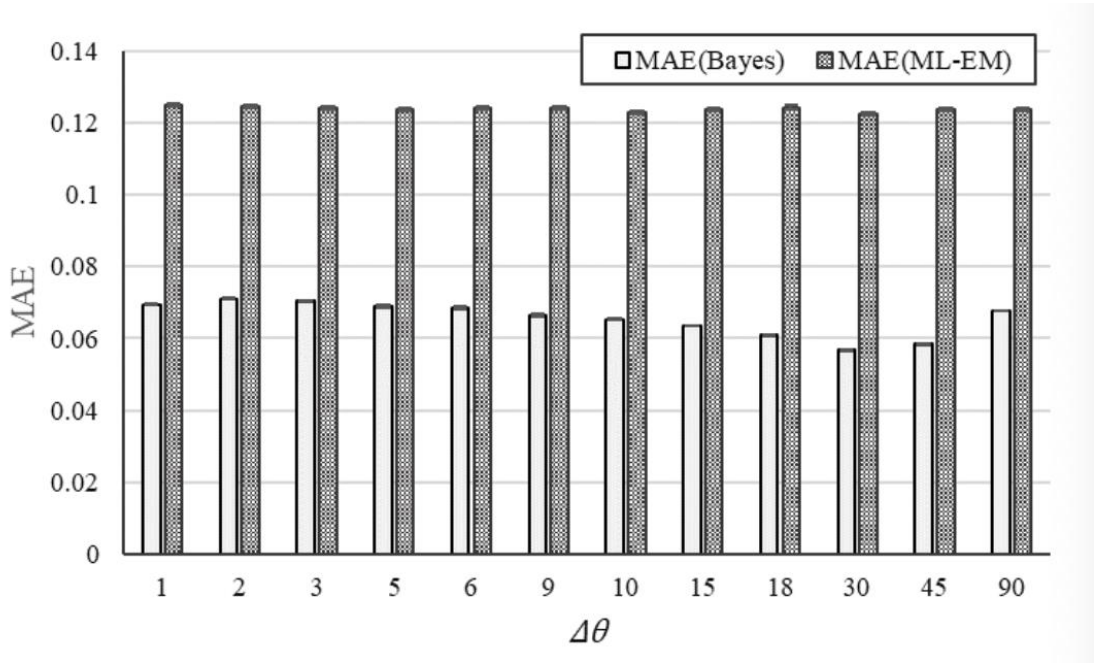

Figure 6.2 Relationship between projection angle $\Delta\theta$ and MAE.

Figure 6.2 shows that the MAE reached its lowest value of 0.0568±0.0002 at $\Delta\theta = 30°$. Across all Δθ values, the MAE trends highlight that $\Delta\theta = 30°$ offers optimal accuracy for image reconstruction, making it a key parameter choice for achieving precise results. This result underscores the importance of carefully selecting Δθ in ensuring minimal error in the reconstructed images.

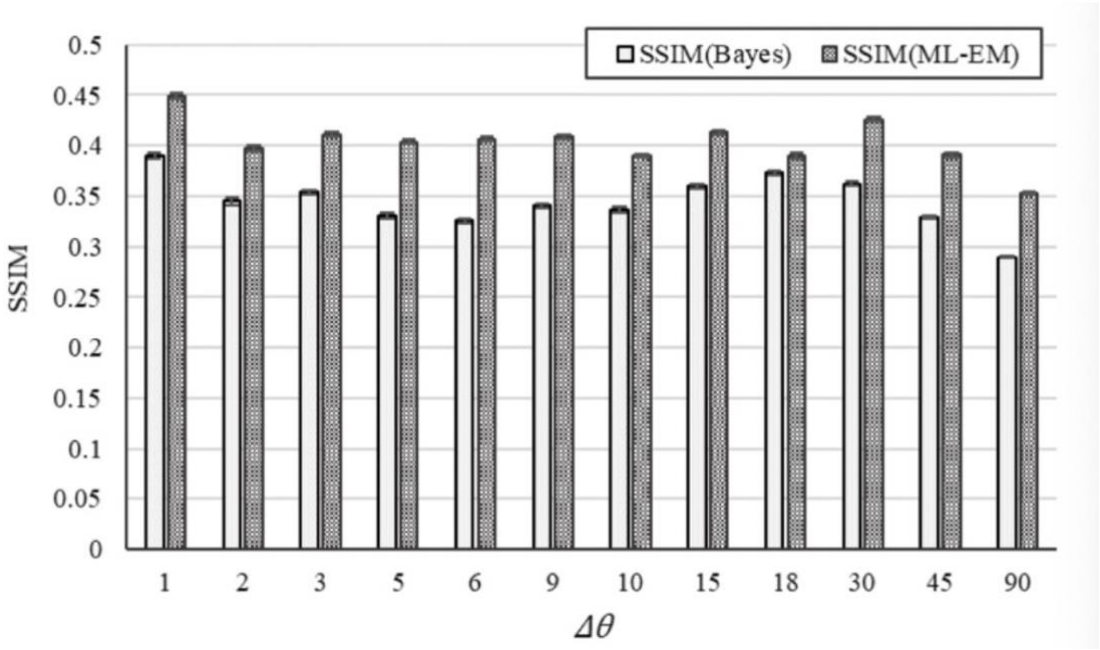

Figure 6.3 Relationship between projection angle $\Delta\theta$ and SSIM.

Figure 4 demonstrates that the highest SSIM values are achieved at $\Delta\theta = 30°$. This finding suggests that $\Delta\theta = 30°$ is the optimal setting for balancing structural similarity and accuracy, particularly when prioritizing precise estimates in normal cells, as supported by the MAE trend.

Based on these findings, it can be concluded that, under the expected conditions of BNCT-SPECT, performing image reconstruction on projection data captured with a 30-degree angular step achieves optimal results.

Figure 6.4 presents the true image, the corresponding sinogram, and the reconstructed images obtained from the initial calculations with a projection angle $\Delta\theta = 30°$. The captions accompanying each figure detail the number of estimation iterations required to generate the images, along with the MAE and SSIM values for the respective reconstructions.

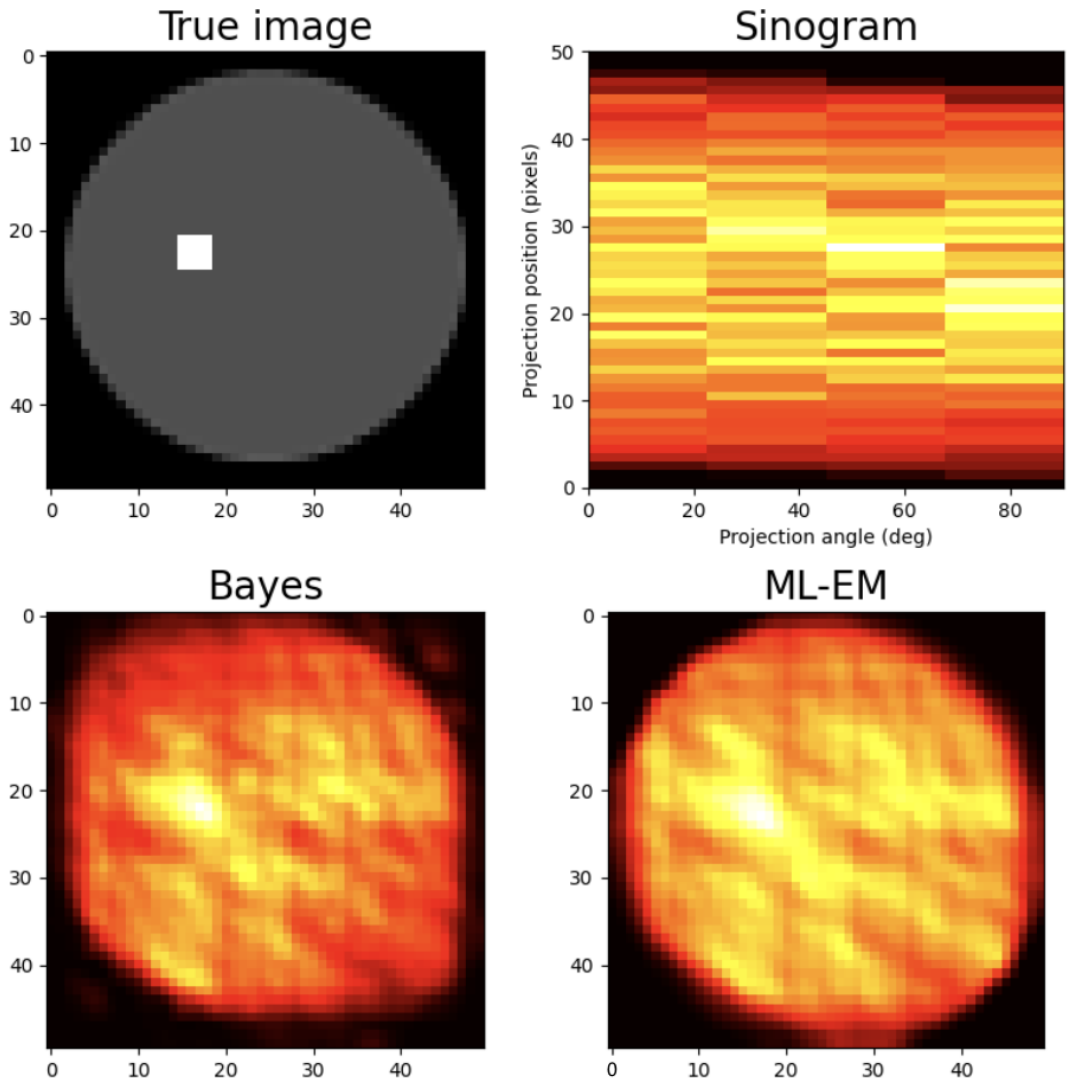

Figure 6.4 Simulation results ($\Delta\theta = 30°$):

Top left: True image (the black areas: regions outside the head, the grey areas: normal cells, the white areas: tumor cells.)

Top right: Sinogram created by projection

Bottom left: Image reconstructed using the Bayesian estimation method (iter =9, MAE =0.0560, SSIM =0.3560)

Bottom right: Image reconstructed using the ML-EM method (iter =3, MAE =0.1223, SSIM =0.3934).

Additionally, Figure 6.5 illustrates the absolute error distributions for each method, visualized as images, providing a clear depiction of the error patterns across the reconstructed images.

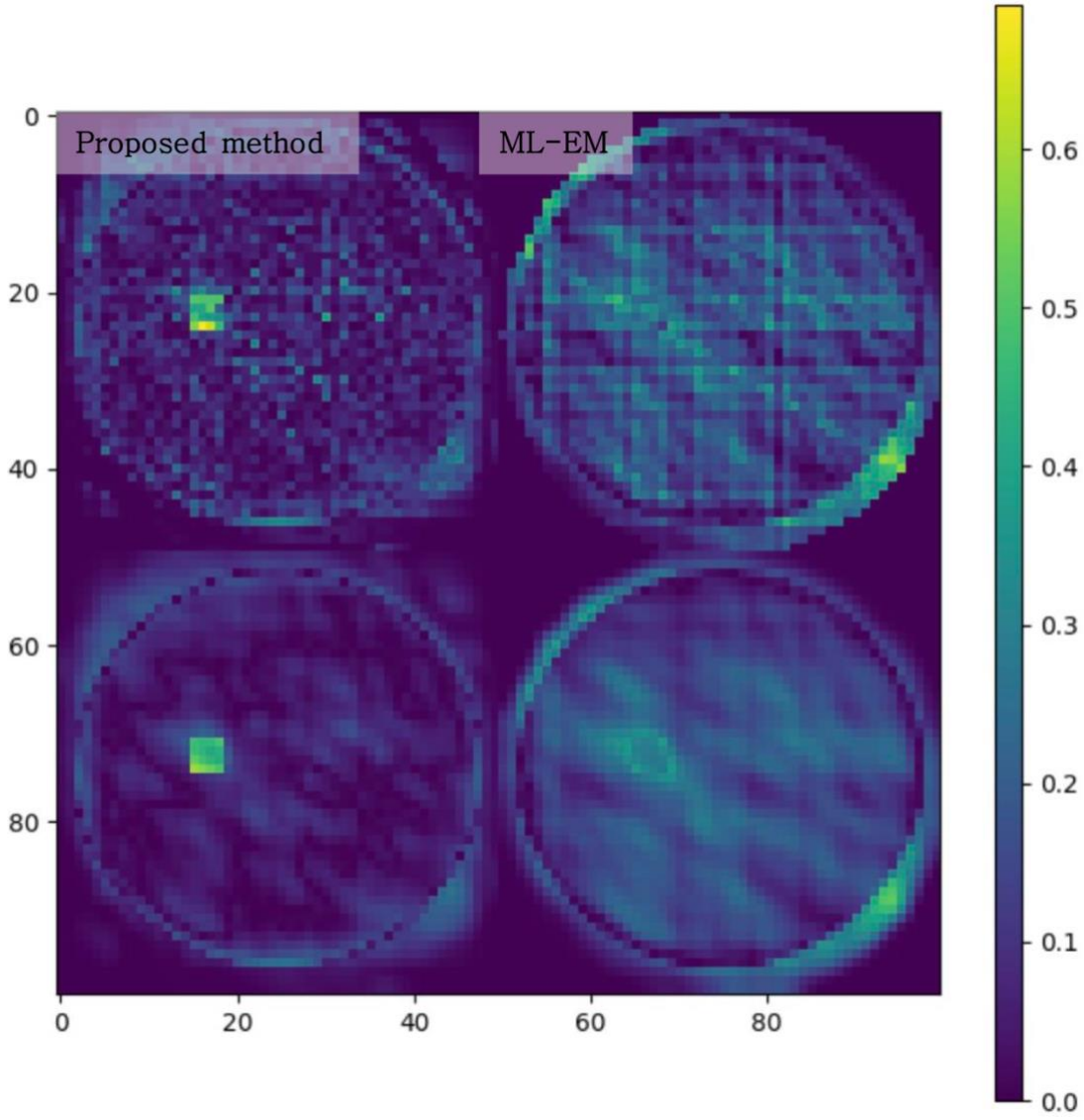

Figure 6.5 Absolute error distribution ($\Delta\theta = 30°$):

Top left: Proposed method, before smearing

Top right: ML-EM method, before smearing

Bottom left: Proposed method, after smearing

Bottom right: ML-EM method, after smearing.

Based on the results, for normal cells (1,408 pixels), the proposed method yielded an average estimated value of 0.3154±0.0005, compared to the true value of 0.31. The MAE for normal cells was calculated as 0.0481±0.0004.

For tumor cells (16 pixels), the proposed method produced an average estimated value of 0.5317±0.0051, whereas the true value was 1.00. Consequently, the Tumor-to-

Normal (T/N) ratio achieved by the proposed method was approximately 1.7, falling short of the expected ratio of 3.2 in this study.

In BNCT-SPECT, the accuracy of pixel values in normal cells is a critical factor for reliable treatment planning and assessment. To evaluate this, the relative error of the reconstructed image was defined as the ratio of the average pixel value of normal cells in the reconstructed image to the true pixel value of normal cells, considering only the normal cells. Using this metric, the relative error for the reconstructed image based on projection data obtained at a 30-degree projection angle was determined to be approximately 16% for the proposed method. A detailed summary of these results is presented in Table 1.

Table 1. Comparison of MAE, SSIM, and average pixel values for estimated images.

$\Delta\theta = 30$	**MAE (Entire image)**	**SSIM (Entire image)**	**Average value of tumor cells (=1.0)**	**MAE (tumor cells)**	**Average value of normal cells (=0.31)**	**MAE (normal cells)**
Proposed method	0.0568±0.0021	0.3624±0.0026	0.5317±0.0051	0.4683±0.0051	0.3154±0.0005	0.0481±0.0004

Considering the statistical errors inherent in BNCT-SPECT measurements, including constraints on projection angles and measurement times, projections performed with $\Delta\theta = 30°$ and image reconstruction using the proposed method yielded promising results. The MAE for the entire estimated image was 0.0568±0.0021, and for normal cells alone, it was 0.3154±0.0005, both demonstrating minimal error. These values were derived from the standard errors of data obtained through 50 numerical experiments, reinforcing the reliability of the findings.

Thus, it can be concluded that "under the conditions anticipated for BNCT-SPECT, performing a total of four projections with a projection angle of $\Delta\theta = 30°$ and using the proposed method for image reconstruction represents the optimal approach." However, when defining the relative error of the estimated image as the MAE of normal cells divided by the true pixel value of normal cells (=0.31), the relative error was approximately 16%, which is relatively high. Additionally, the T/N ratio remained around 1.7, significantly lower than the expected value of 3.2.

These findings indicate that while the proposed method shows promise, process improvements are required to address the high relative error and suboptimal T/N ratio to ensure practical and effective implementation of BNCT-SPECT in clinical settings.

6.2.2 Reconstruction at $\Delta\theta = 20°$ with six models

The reconstructed results presented in the previous section show there can be substantial improvement in our image reconstruction method. In this study, based on the principles of Bayesian estimation, we developed a Split-TV-EM approach.

The TV-EM （Total Variation Expectation Maximization） method is a technique that incorporates total variation (TV) norm regularization into the ML-EM (Maximum Likelihood Expectation Maximization) algorithm to achieve more accurate data reconstruction.

The ML-EM method is a widely used iterative algorithm for image reconstruction in emission tomography. It estimates the most likely distribution of the radioactive source by maximizing the likelihood function based on measured projection data. However, ML-EM often suffers from noise amplification, particularly in low-count regions, leading to degraded image quality.

To address this issue, the TV-EM method introduces TV norm regularization into the ML-EM framework. The TV norm helps suppress noise and preserve edge structures by minimizing excessive intensity variations in the reconstructed image. By incorporating this regularization term, TV-EM enhances image quality while maintaining spatial resolution, making it particularly suitable for limited-view-angle reconstruction scenarios.

To effectively reduce noise and enhance the clarity of tumor shape reproduction, this study develops the Split-TV-EM method based on the aforementioned approach. Figure 6.6 illustrates the workflow of the Split-TV-EM method. A distinctive feature of Split-TV-EM is its ability to utilize measured sinogram data obtained from FBPA-PET, which is conducted prior to BNCT treatment to predict therapeutic effects. This method separates the normal cell region and tumor cell region within the sinogram and performs image reconstruction for each region independently. By doing so, it aims to improve reconstruction accuracy and better preserve tumor morphology.

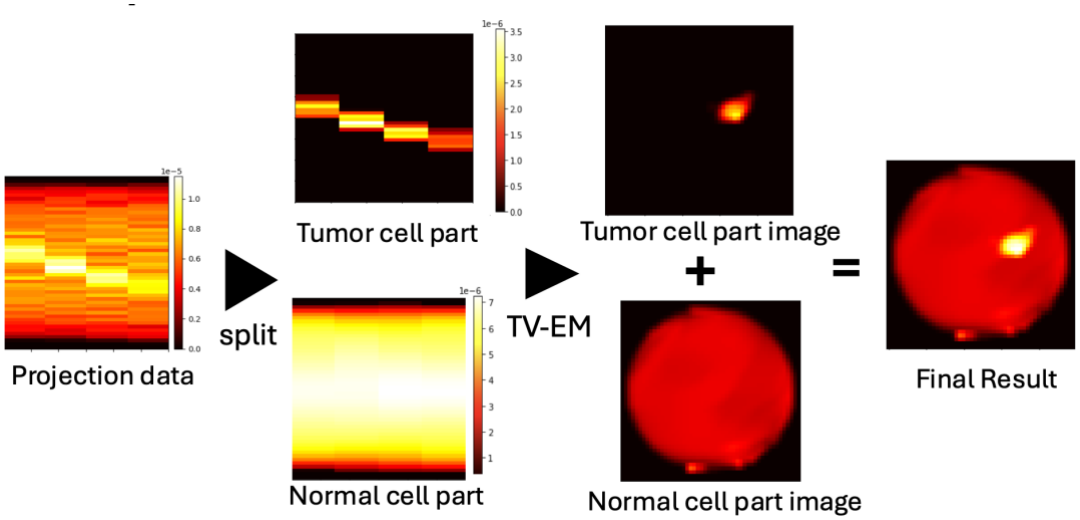

Figure 6.6 The workflow of the Split-TV-EM

Further research revealed that due to equipment design constraints in BNCT-SPECT, the projection moving angle θ must be less than 90°. When measuring gamma rays in BNCT-SPECT, the detector system rotates around the center of the head phantom, as shown in Figure 6.7. Since BNCT-SPECT requires measurements to be conducted during treatment, various treatment equipment, such as the patient bed and neutron source, restrict the rotation path of the detector. As a result, as illustrated in Figure 6.8, the projection angle is limited to less than 180 degrees, and the projection moving angle itself is further constrained to less than 90 degrees.

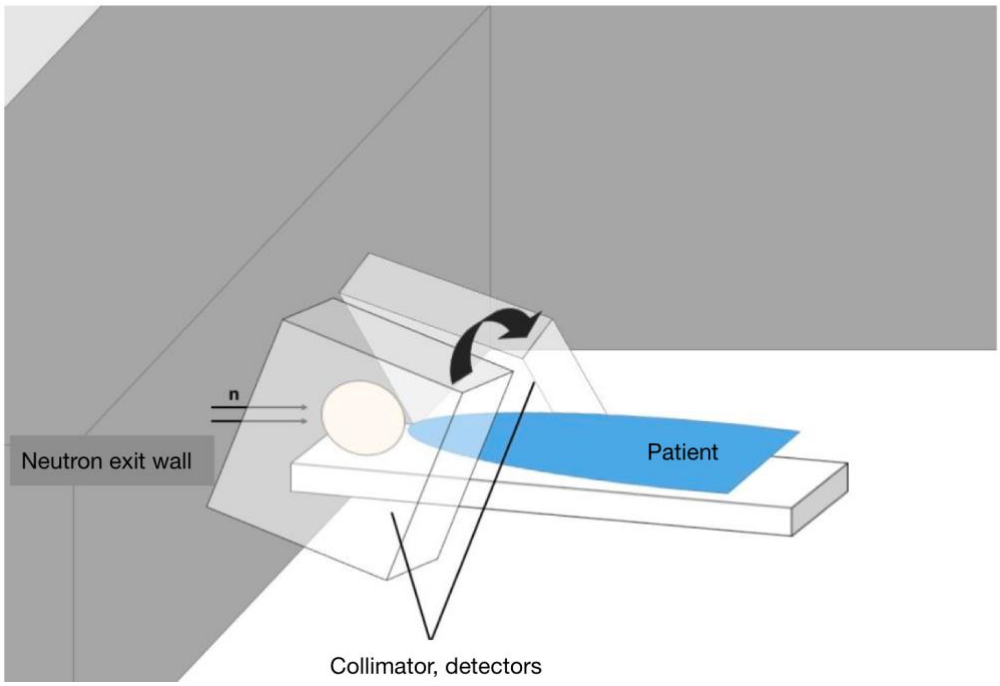

Figure 6.7 Overall diagram of the detection system

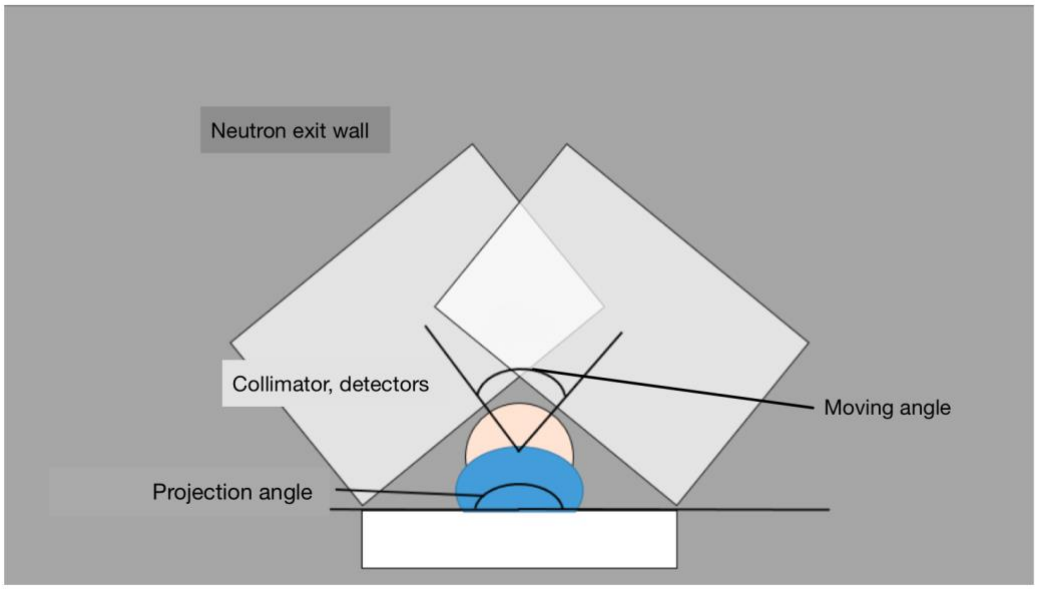

Figure 6.8 Illustration of projection angles and projection moving angle

Although larger projection angles generally improve reconstruction accuracy, smaller projection angles simplify the design and implementation of the system. Therefore, it is crucial to determine the minimum detection angle that can maintain reconstruction accuracy at a level sufficient for diagnostic purposes. Therefore, based on the

computational studies by our research group in 2024, the projection parameters were set to $\theta = 60°$ and $\Delta\theta = 20°$. [3]

In this numerical experiment, image reconstruction was performed using a total of six source models. These models are referred to as Models 1 to 6, and their details are described below. The projection directions are illustrated in Figure 6.9.

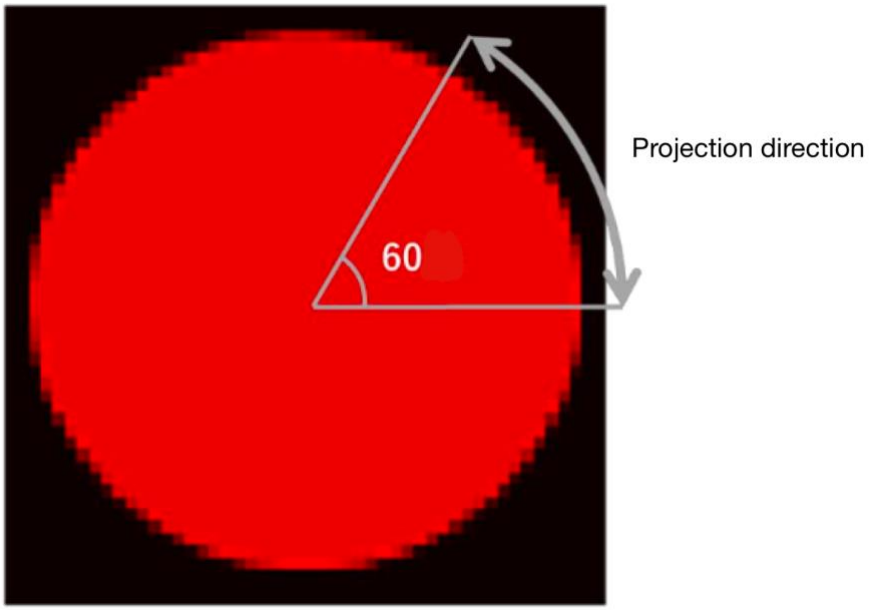

Figure 6.9 Projection direction

Model 1 represents a scenario where a single circular tumor exists within a uniform field of normal cells. This model was designed to evaluate whether the source concentration in both normal and tumor cells could be accurately reproduced when a small tumor is located in the deep brain. The tumor was positioned near the projection direction in the upper right region, with its minimum depth from the head surface set at 5.2 cm. The tumor's shape was modeled as a circle with a diameter of 4 pixels (=1.6 cm).

In the figure, the black areas indicate regions outside the head, the red areas represent normal cells, and the white areas represent tumor cells. If the brightness levels of the black and white areas are set to 0 and 1, respectively, the brightness level of the red areas is set to 0.31. This brightness difference corresponds to the T/N ratio, which

reflects the relative boron accumulation in tumor cells compared to normal cells. In this system, the T/N ratio is approximately 1/0.31≈3.23.

Model 2 replaces the circular tumor in Source Model 1 with an elliptical shape. This model was developed to evaluate whether the source concentration in normal and tumor cells can be accurately reproduced when a larger tumor exists in the deep brain. The elliptical tumor was positioned such that its center coincided with the center of the circular tumor in Source Model 1. In this configuration, the minimum depth from the head surface to the tumor is 4.5 cm. The ellipse representing the tumor has a major axis of 7 pixels (=2.4 cm) and a minor axis of 5 pixels (=1.6 cm).

Models 3 and 4 are variations of Models 1 and 2, respectively, with the tumor positions moved closer to the head surface. These models were designed to evaluate whether the source concentrations in normal and tumor cells can be accurately reproduced when smaller or larger tumors are located in more superficial regions of the brain.

For Model 3, the tumor shape is identical to that of Model 1, with a minimum depth of approximately 2.1 cm from the head surface. Similarly, for Model 4, the tumor retains the elliptical shape of Model 2, but its minimum depth is reduced to approximately 1.7 cm. These configurations enable the assessment of reconstruction accuracy for tumors located closer to the surface.

Models 5 and 6 are extensions of Models 1 and 2, respectively, with an additional elliptical region introduced to simulate the leakage of boron from the tumor into surrounding normal cells. This elliptical region has a brightness value of 0.5 and dimensions of 20 pixels for the major axis and 16 pixels for the minor axis.

The elliptical region is positioned slightly to the right within the circular area representing normal cells, at a minimum depth of 3.2 cm from the head surface. These models aim to evaluate the ability of the proposed method to reproduce distributions with smaller variations in normal cells compared to tumors. Additionally, they assess the impact of tumor shape on the reproducibility of these distributions. This configuration enables a deeper understanding of the method's performance under more complex conditions.

The six source models themselves are depicted in Figure 6.10.

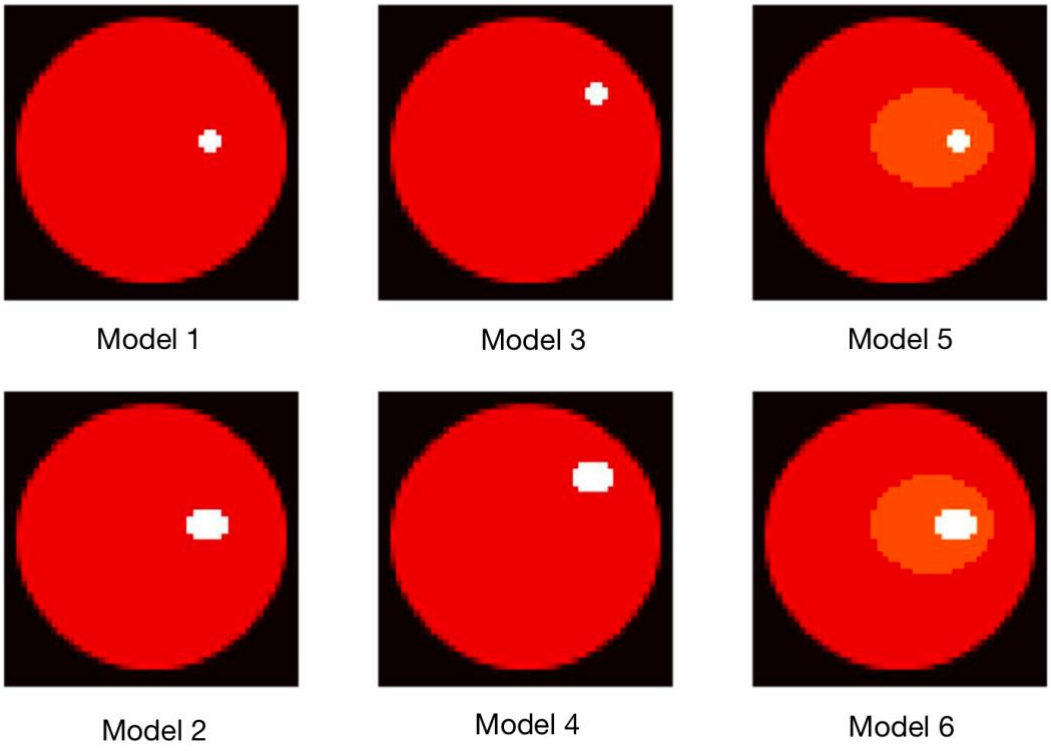

Figure 6.10 Model 1-6

The reconstruction results are shown in Figures 6.11 to 6.16.

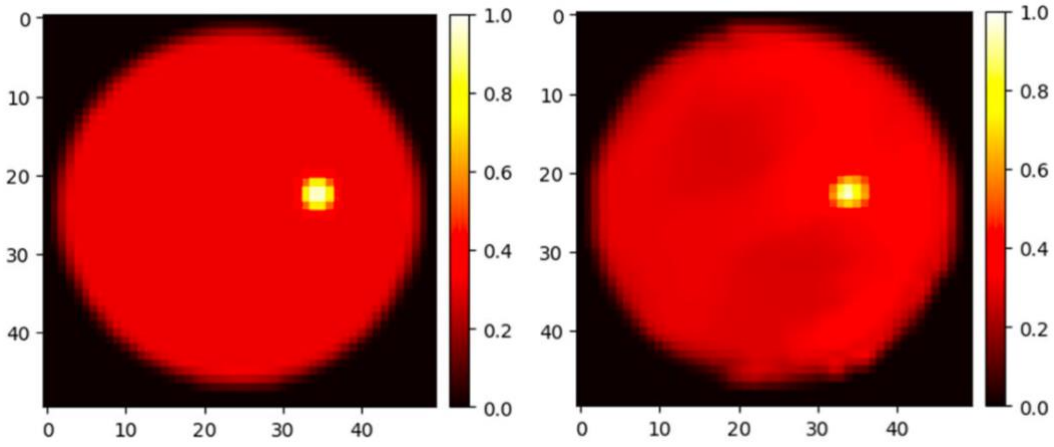

Figure 6.11 Model 1: true image and reconstructed image

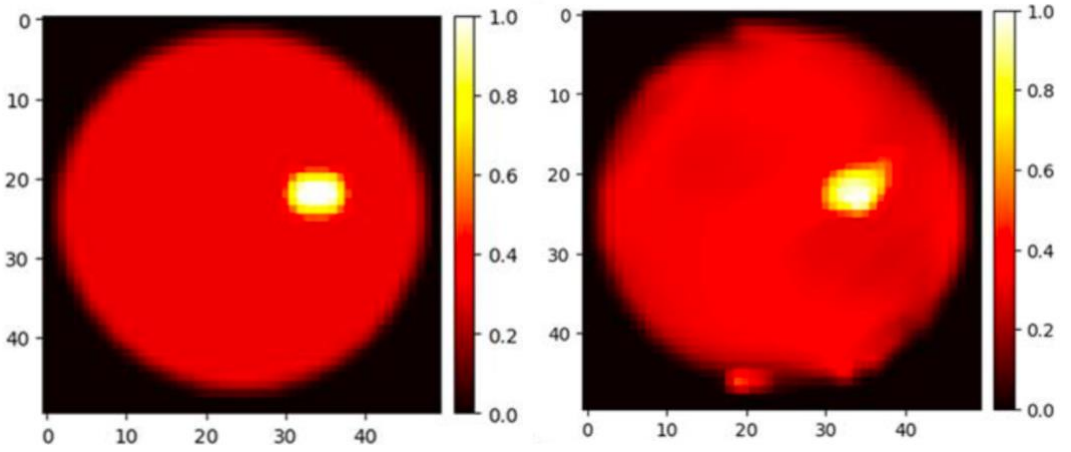

Figure 6.12 Model 2: true image and reconstructed image

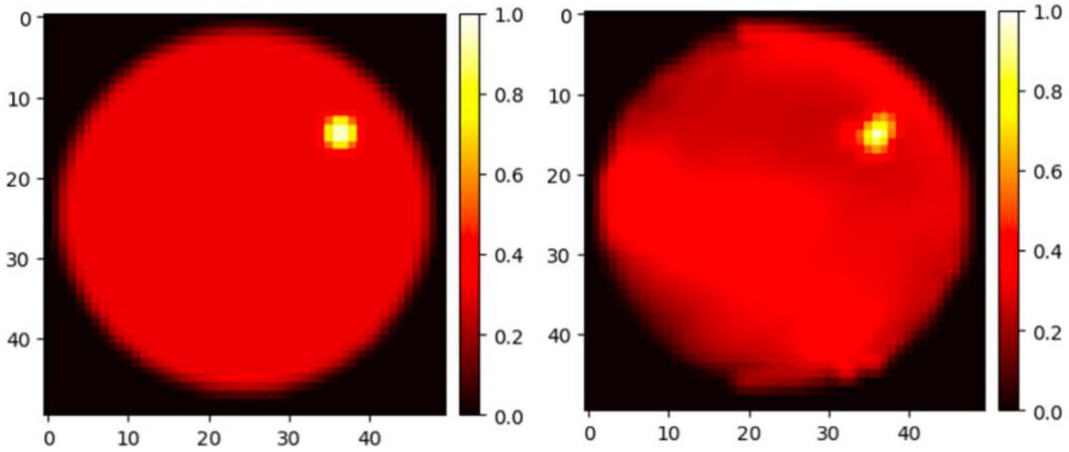

Figure 6.13 Model 3: true image and reconstructed image

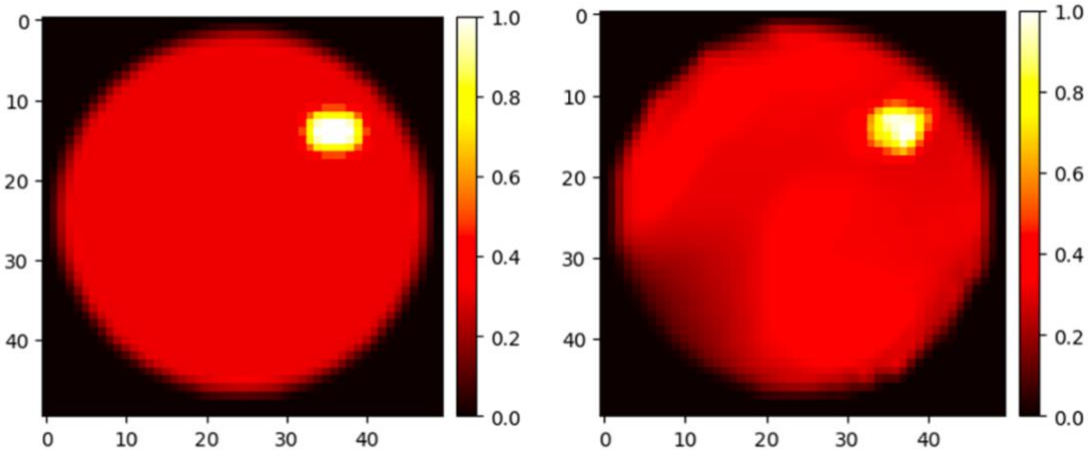

Figure 6.14 Model 4: true image and reconstructed image

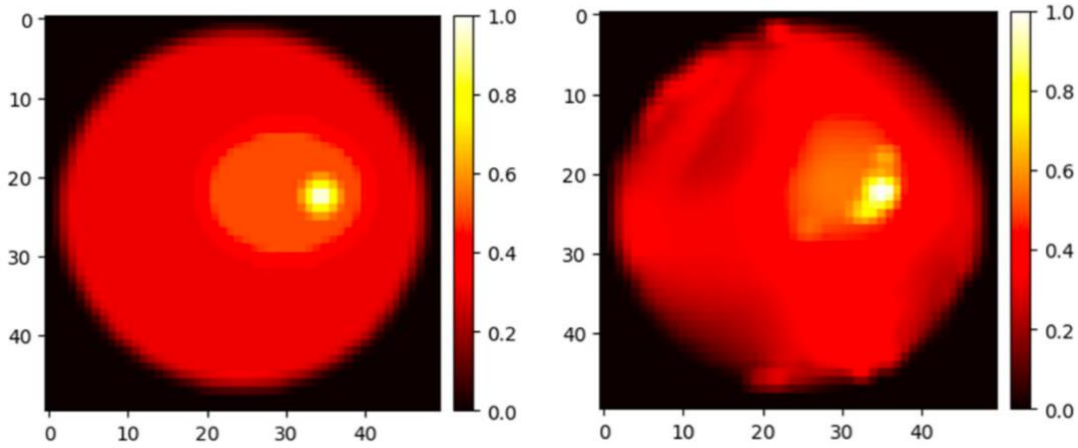

Figure 6.15 Model 5: true image and reconstructed image

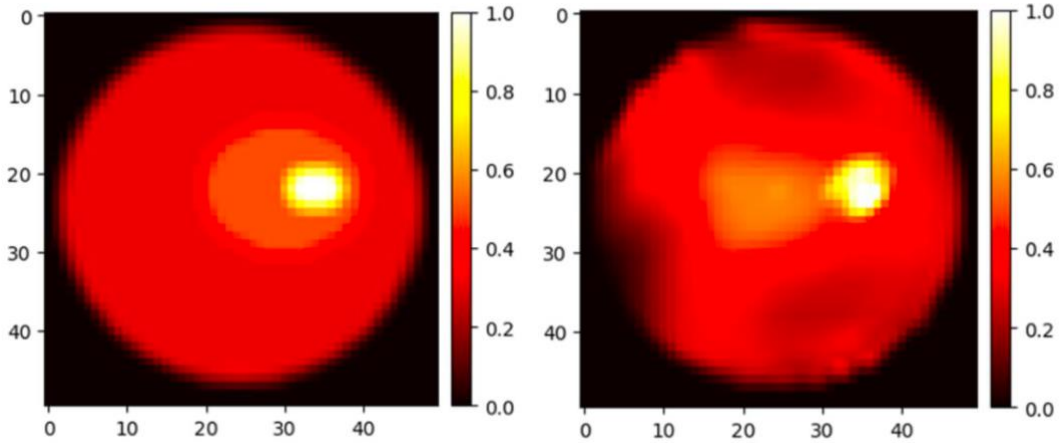

Figure 6.16 Model 6: true image and reconstructed image

Using the six models, image reconstruction was performed with the proposed Split-TV-EM method, and the results were compared to evaluate its performance. The evaluation revealed two significant strengths of the proposed method.

The first strength lies in its exceptional noise reduction capability in normal cells. This is primarily due to the creation of sinograms for normal cells through polynomial fitting, which not only interpolates the missing peaks in the sinogram of normal cells but also effectively eliminates noise.

The second strength addresses a common issue arising when the sampling density of the sinogram is low—namely, the distortion of tumor regions in the projection direction

and the associated underestimation of pixel values. By separating the tumor and normal cell regions within the sinogram, the proposed method reconstructs the tumor region without the influence of background signals from normal cells. As a result, pixel values originating from the tumor region are not dispersed into the normal cell area, allowing the pixel values to remain concentrated in the tumor region and preventing underestimation.

On the other hand, the proposed method has five challenges, albeit some of them are minor:

First, slightly Enlarged Tumor Shape: The reconstructed tumor shape may appear approximately one pixel larger in diameter than its actual size. However, since the total pixel value of the tumor region remains unchanged, this issue is not significant in BNCT-SPECT, where pixel values are more critical than precise shape accuracy.

Second, the formation of Artificial Peaks: A one-pixel-wide false peak may sometimes form at the outer edge of the tumor region. This peak becomes less noticeable when a Gaussian blur is applied, making it a minor concern.

Third, loss of Fine Features in Normal Cells: Fine details in the distribution of the normal cell region may be lost during reconstruction. However, in BNCT-SPECT, these fine details are not a priority, as the average pixel value representing the therapeutic effect is the primary focus. Hence, this issue is not a significant concern.

Fourth, distortion in Tumor Shape for Larger Tumors: When the tumor is larger, the peaks in the sinogram may split into multiple peaks, leading to distortions in the tumor shape in the reconstructed image. Although the distortion can often be mitigated by applying a Gaussian blur, the number of pixels occupied by the tumor generally does not change significantly. Consequently, the impact on the Tumor-to-Normal (T/N) ratio is minimal, making this issue less critical.

Fifth, sensitivity to Noise in Tumor Reconstruction: Tumor reconstruction is more susceptible to noise, especially for small and deep-seated tumors. This can result in frequent distortions in the tumor shape and increased variance in the tumor's average pixel value and the T/N ratio. This issue could be addressed by pre-estimating the number of pixels occupied by the tumor using auxiliary examinations such as FBPA-

PET. However, this approach would require additional prior information, which should be considered carefully.

By performing image reconstruction using the proposed method, it is possible to address the major challenges associated with image reconstruction in BNCT-SPECT. Therefore, the proposed method can be considered well-suited as a reconstruction algorithm specifically designed for BNCT-SPECT. However, the method still faces the issue of tumor shape distortion, which leads to increased variance in the Tumor-to-Normal (T/N) ratio. Hence, further improvements are necessary to resolve these challenges and enhance the method's performance.

6.3 Reconstruction with experimental data

In this section, we conduct experiments using the mock-up system established in Chapter 5. The experimental procedure follows the sequence described in the previous section.

A suitable volumetric gamma-ray source could not be prepared for this study; instead, a point source was utilized for the measurements. However, measuring a pulse height spectrum for a point source with collimators posed significant challenges due to the large variability in count numbers with slight positional changes. To address this, the measurements were conducted without collimators, and the results will be subsequently corrected through simulation to account for the absence of collimation.

In this setup, the ^{137}Cs gamma-ray source was positioned at the center of the head phantom, corresponding to the four central pixel locations. The head phantom was divided into sections, and for each position, measurements were conducted at four projection angles: 0, 20, 40, 60 degrees. An illustration of the projection angles is shown in Figure 6.17.

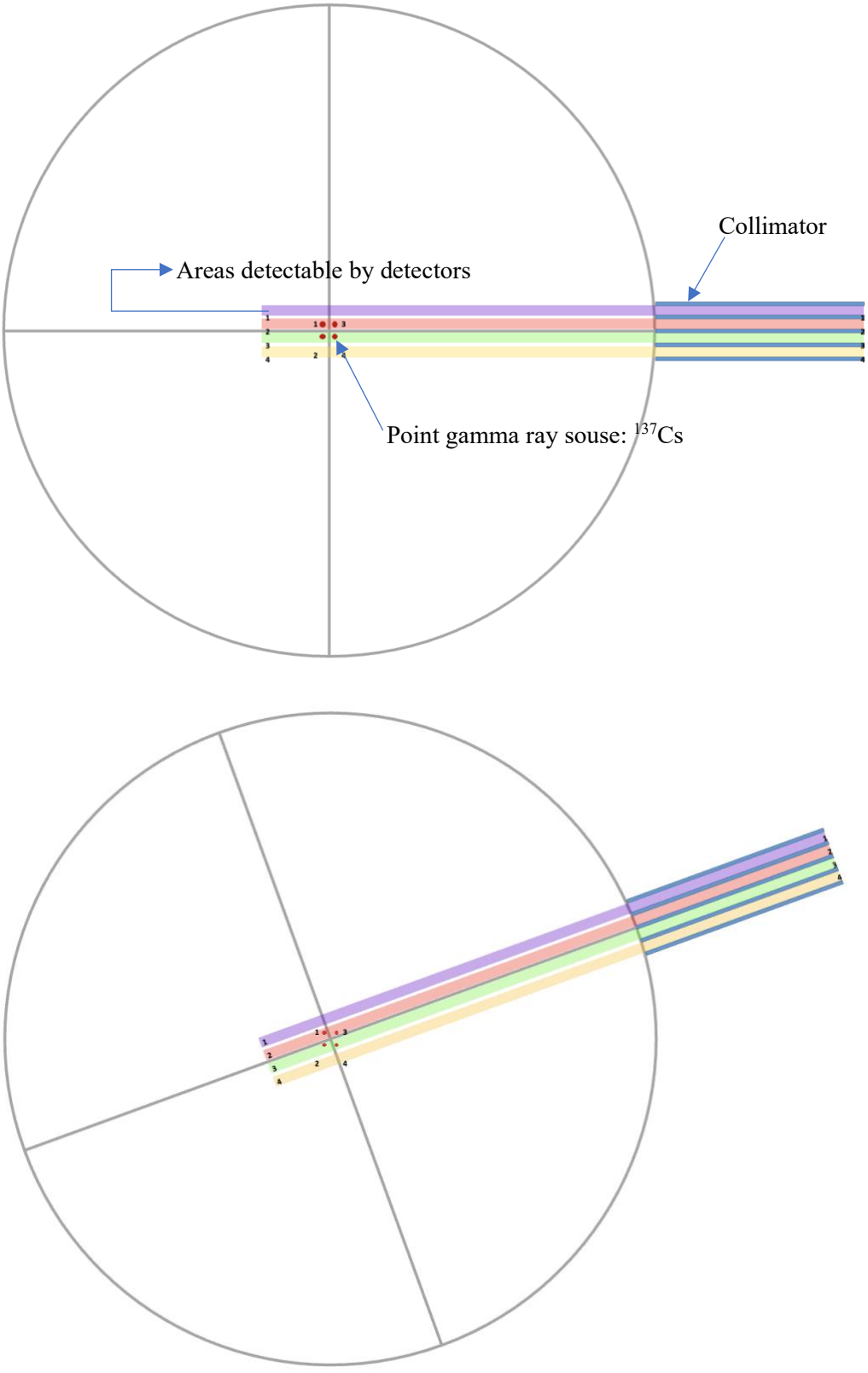
Collimator
Areas detectable by detectors
Point gamma ray souse: ^{137}Cs

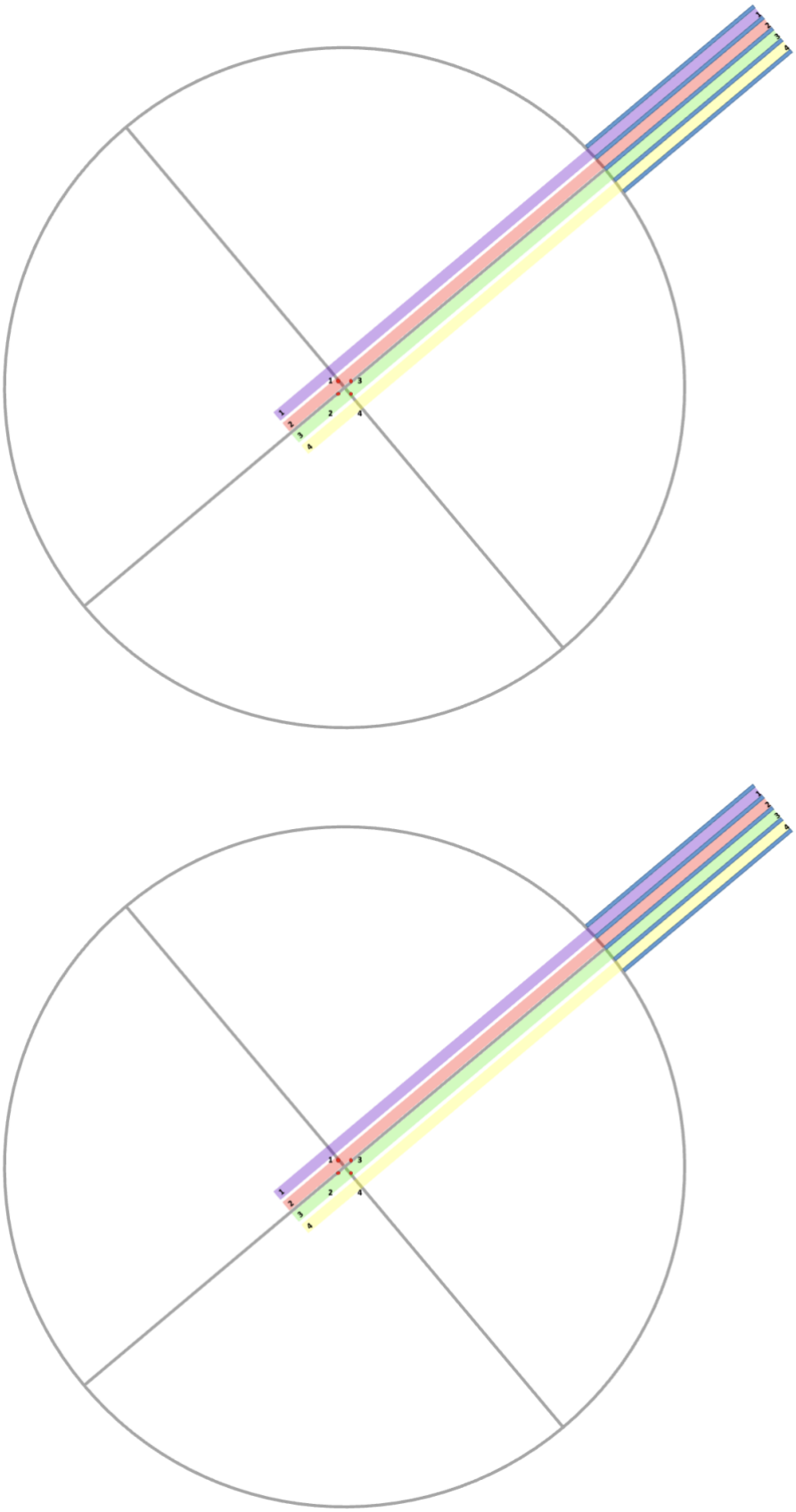

Figure 6.17 Projection angles: 0, 20, 40, 60 degrees

Simulation calculations were performed using MCNP5 to replicate the experimental setup accurately. The simulation was conducted twice under the same conditions: once with collimators and once without collimators. This process produced two distinct response functions. The corrected count, N_C , corresponding to a system with collimators, can be calculated using the following Equation (6.1):

$$N_C = N_{NC} \times \frac{R_C}{R_{NC}} \tag{6.1}$$

where N_{NC} is the number of counts measured in the experiment without collimators, R_C is the simulated response function with collimators, R_{NC} is the simulated response function without collimators.

This corrected count value serves as an effective proxy for the true system response and can be utilized for image reconstruction, ensuring that the results more accurately reflect the conditions of a system with collimators.

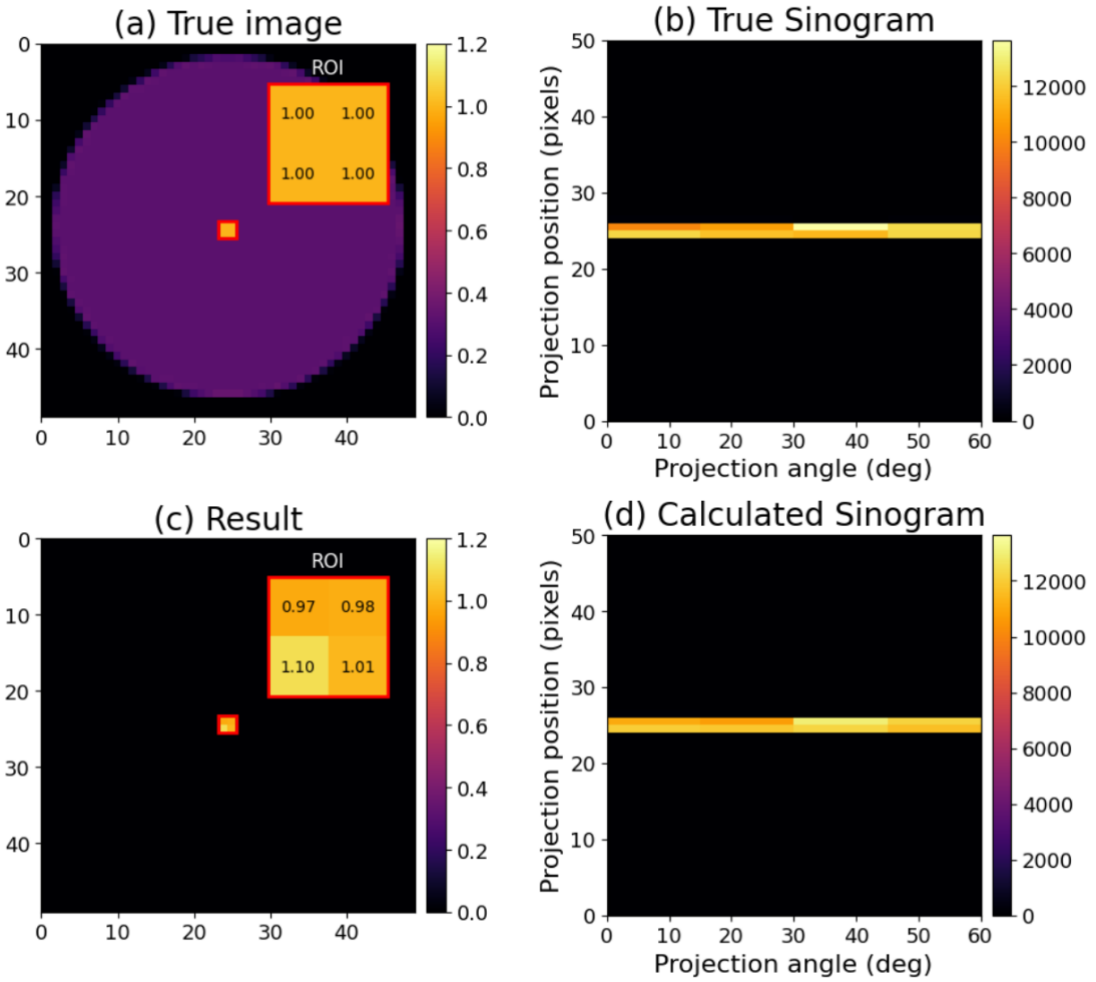

Figure 6.18 Results of image reconstruction

Figure 6.18 illustrates the initial image reconstruction results obtained using the new response function derived from prototype measurements.

- Panel (a): The true image represents the experimental setup, featuring four centrally located sources, each occupying a single pixel with an initial value of 1.0 (orange). The background pixels are assigned a value of 0.31 (purple), reflecting the relative contrast between the sources and the surrounding area.
- Panel (b): The sinogram, generated using the Radon Transform algorithm, simulates the data as it would be captured by the SPECT system during measurements.

- Panel (c): The reconstructed image is presented, derived from the sinogram data, showing meaningful information confined to the Region of Interest (ROI). This focus is a direct result of the tailored design of the response function.
- Panel (d): The calculated sinogram is produced by applying a second Radon Transform to the reconstructed image, providing a comparative analysis with the initial sinogram.

This approach highlights the accuracy and functionality of the new response function in reconstructing data within the ROI.

The measurements were performed exclusively for the four central pixels. As a result, the rest of the response function, even after applying the correction, contains zero values. Consequently, in this simulation, only signals originating from the centrally located pixels are detectable. This limitation confines the reconstructed image to represent only the central region, restricting the scope of the reconstructed data to the area covered by the measured response function.

This initial result confirms that our image reconstruction system can successfully reproduce the original image, even with limited-view angle projection data. The values of all four individual pixels deviate by approximately 10% from the actual γ-ray source intensity. Moving forward, the objective is to reduce these deviations to less than 5%.

Both individual pixel accuracy and ROI accuracy are critical for effective treatment monitoring in BNCT. Significant discrepancies or systematic errors in individual pixel values could result in misinterpretations of the boron distribution, potentially compromising treatment efficacy. To address this, future experiments should replicate this study for other pixel locations to assess the consistency of discrepancies between the true and reconstructed images and identify any potential systematic errors. Extending these evaluations to include tumors located in various positions within the phantom will aid in validating the image reconstruction method for the prototype, ensuring its reliability and accuracy in practical applications. Conducting experiments with tumors placed at different locations, rather than solely at the center of the phantom, is essential for a more comprehensive and meaningful evaluation of this image

reconstruction method in future studies.

6.4 Summary

In this chapter, we present the results of image reconstruction using both mathematically ideal response functions and experimental data derived from the mock-up system established in Chapter 5. The focus is on evaluating the effectiveness and accuracy of the proposed Bayesian estimation method under conditions relevant to BNCT-SPECT.

Section 6.1 introduces the chapter, explaining the two distinct reconstruction scenarios: using an ideal response function and employing experimental data. The aim is to compare the reconstruction quality across these methods and explore how well the experimental setup replicates the designed BNCT-SPECT system.

Section 6.2 explores the reconstruction process using a mathematically ideal response function. This section is further divided into two parts: Section 6.2.1 investigates reconstruction using a single model at a projection angle of $\Delta\theta=30°$. This configuration, based on previous studies, demonstrates promising results, achieving minimal MAE and a well-defined T/N ratio. Section 6.2.2 introduces the Split-TV-EM method, which is developed based on the Bayesian estimation principles discussed in Chapter 2. This section examines reconstruction using six different models at a projection angle of $\Delta\theta=20°$. By applying multiple models, this section evaluates the robustness of the reconstruction process and the impact of varying tumor shapes and locations on reconstruction quality.

Section 6.3 shifts focus on experimental data obtained through the mock-up system. Utilizing corrected response functions derived from MCNP simulations, this section validates the practicality of the proposed method under real experimental conditions. It highlights the challenges of limited-view angle projection data and discusses the system's performance in reconstructing images for central pixel locations.

The results in this chapter confirm the efficacy of the proposed Bayesian estimation method for BNCT-SPECT image reconstruction. While reconstruction accuracy is promising, particularly for central regions, challenges remain in achieving consistent

results for tumors positioned at various locations within the phantom and reducing systematic discrepancies. These findings emphasize the need for further experiments to validate the method across varying pixel locations and projection conditions, paving the way for improvements in clinical applications.

References

[1] Menéndez, P. R., Roth, B. M. C., Pereira, M. D., Casal, M. R., González, S. J., Feld, D. B.,Santa Cruz, G.A.,Kessler, J.,Longhino, J.,Blaumann, H.,et al. “BNCT for skin melanoma in extremities: updated Argentine clinical results. Applied Radiation and Isotopes”, 67(7-8),(2009): S50-S53.

[2] Lu, F.; Inamoto, H.; Takeishi, S.; Tamaki, S.; Kusaka, S.; Murata, I. Development of a New Image Reconstruction Method Using Bayesian Estimation with Limited View-Angle Projection Data for BNCT-SPECT. *Appl. Sci.* **2024**, *14*, 9411. https://doi.org/10.3390/app14209411

[3] 奥田　航生: BNCT-SPECT 用画像再構成アルゴリズムの開発,” 修士学位論文, 大阪大学大学院工学研究科 (2024).

Chapter 7 Conclusion

This study explores the image reconstruction technique for BNCT-SPECT systems, aiming to address critical challenges of reconstruction images from limited-view-angle projection data- a key constraint in real-time BNCT monitoring. The research systematically investigates the design, simulation, and experimental validation of a BNCT-SPECT prototype, focusing on achieving accurate image reconstruction under practical constraints. Below, the major contributions and findings of each chapter are summarized, culminating in key conclusions and future directions.

Chapter 1 introduces the fundamental principles of BNCT and SPECT, tracing their development and integration into BNCT-SPECT systems for real-time treatment monitoring. The unique challenges in BNCT, such as the need for high precision and overcoming constraints like limited projection angles, are highlighted. This chapter establishes the motivation for adopting a hybrid imaging system and outlines the structure of the paper.

Chapter 2 discusses the theoretical basis of Bayesian estimation, emphasizing its application in image reconstruction for BNCT-SPECT. The chapter compares Bayesian estimation with the widely-used ML-EM method, demonstrating the suitability of Bayesian estimation methods for limited-view-angle data. Performance evaluation metrics, such as Mean Absolute Error (MAE) and Structural Similarity Index (SSIM), are introduced to quantify image quality.

Chapter 3 details the experimental setup for the study, including the selection and evaluation of key components like the GAGG(Ce) scintillator, MPPC, and MCA. The design and construction of a head phantom with precise geometric and material properties are presented. Experimental procedures are outlined to validate the imaging system, with emphasis on achieving realistic experimental conditions to replicate BNCT-SPECT scenarios.

Chapter 4 introduces MCNP5 simulations to model the BNCT-SPECT system. The Monte Carlo method is employed to calculate response functions and simulate complex interactions between radiation and matter. Variance reduction techniques and tally tools

are utilized to optimize computational efficiency, and simulation results validate the feasibility of the proposed imaging system under controlled conditions.

Chapter 5 focuses on the design and construction of a mock-up system, integrating components such as collimators, ^{137}Cs, and ^{60}Co sources. Key design parameters, including spatial resolution and gamma-ray intensity, are meticulously optimized to ensure compatibility with BNCT-SPECT requirements. The chapter highlights the success of the mock-up system in replicating key experimental specifications.

Chapter 6 presents the results of image reconstruction using both mathematically ideal response functions and experimental data. Reconstructions were conducted under various projection angles ($\Delta\theta=30°$ and $\Delta\theta=20°$) using single and multiple source models. The results demonstrate the efficacy of Split-TV-EM method in achieving high reconstruction accuracy, with minimal MAE and acceptable SSIM values under constrained experimental conditions. Challenges related to tumor shape distortion and noise sensitivity are also discussed, paving the way for future improvements.

Key Findings and Contributions

1. Addressing Limited-view-angle projection angle: The study confirms the viability of Bayesian estimation for reconstructing images with high accuracy under limited projection angles. The method outperforms traditional approaches, particularly in noise reduction.
2. Development of Mock-Up System: The developed mock-up system successfully simulates BNCT-SPECT conditions, with results demonstrating its ability to reproduce key experimental parameters such as S/N ratio and statistical accuracy.
3. Integration of Simulation and Experimentation: MCNP5 simulations complement experimental measurements, enabling corrections for collimator effects and enhancing the reliability of the reconstructed images.

Challenges and Future Directions

While the study demonstrates significant advancements in BNCT-SPECT imaging, several challenges remain:

- Tumor Shape Distortion: Reconstruction inaccuracies in tumor shape,

particularly for smaller or deeper tumors, require further refinement of the response function.

- Noise Sensitivity: Improved noise reduction techniques are essential for enhancing the reliability of reconstructed images under realistic conditions.
- Tumor Position Diversification: Future studies should focus on reconstructing images for tumors located in various positions within the phantom to ensure consistent accuracy across all regions of interest.

In conclusion, this research tackles the critical problem of reconstructing images using limited-view-angle projection data in BNCT-SPECT systems, offering promising insights into real-time treatment monitoring. By integrating Bayesian estimation methods with experimental and simulation-based validations, the study establishes a robust foundation for real-time treatment efficacy monitoring during BNCT treatments. By developing and validating a BNCT-SPECT system capable of reconstructing images with high precision, this study provides a reliable image reconstruction technique. Addressing the identified challenges and refining the system further will strengthen its potential to reliably monitor and guide BNCT treatments, ultimately contributing to safer and more effective clinical applications.

Acknowledgement

Time passes in the blink of an eye, and my doctoral journey is now coming to an end. Throughout these years, I have grown both academically and personally, and I am deeply grateful for all the experiences, challenges, and support that have shaped me along the way.

First and foremost, I would like to express my sincere gratitude to my supervisor, Professor Isao Murata, whose unwavering guidance, patience, and encouragement have been invaluable to my research and personal growth. His profound insights and rigorous academic approach have not only helped me complete this dissertation but have also instilled in me the spirit of scientific inquiry and perseverance that will guide me in my future endeavors. I am also deeply appreciative of the members of my dissertation committee, Professor Sato and Associate Professor Akiyama, for their invaluable feedback and constructive suggestions, which have greatly enriched this work. Their expertise and insights have pushed me to refine my research and strive for higher academic standards.

My heartfelt thanks go to my colleagues and friends in the laboratory. Their companionship and intellectual discussions have made my research journey both stimulating and fulfilling. I am particularly grateful to Dr. Kusaka, Dr. Tamaki, and Mr. Izutani for their support, whether in research collaboration or school life. The time we spent working together, exchanging ideas, and overcoming challenges has been truly memorable. Furthermore, I would like to extend my gratitude to the fellowship-Quantum Leader Resources for providing the necessary support and resources that made this journey possible. The academic environment and facilities at University of Osaka have played a crucial role in enabling me to pursue my studies in a conducive and enriching setting.

Beyond academia, I owe my deepest appreciation to my family. Their unconditional love, encouragement, and sacrifices have been my greatest source of strength throughout this journey. Despite the physical distance, their support has always been with me, reminding me that I am never alone in my pursuit of knowledge. The end of

this doctoral journey marks not only the culmination of my research but also the beginning of a new chapter. I will carry forward the lessons I have learned, the friendships I have forged, and the invaluable experiences I have gained, as I step into the future with gratitude and determination.